INTERNATIONAL SCIENTIFIC JOURNAL

MATHEMATICAL MODELING

YEAR IY, ISSUE 1/2020
ISSN (PRINT) 2535-0986
ISSN (WEB) 2603-2929

Published by
SCIENTIFIC-TECHNICAL UNION of MECHANICAL ENGINEERING - INDUSTRY 4.0
Sofia, BULGARIA

INTERNATIONAL SCIENTIFIC JOURNAL

MATHEMATICAL MODELING

PUBLISHER:

SCIENTIFIC TECHNICAL UNION OF MECHANICAL ENGINEERING "INDUSTRY 4.0"

108, Rakovski Str., 1000 Sofia, Bulgaria
tel. (+359 2) 987 72 90,
tel./fax (+359 2) 986 22 40**,**
office@stumejournals.com
www.stumejournals.com

ISSN (PRINT) 2535-0986
ISSN (WEB) 2603-2929
YEAR IV, ISSUE 1 / 2020

EDITOR IN CHIEF:

Prof. D.Sc. ANDREY FIRSOV
Peter the Great St.Petersburg Polytechnic University, Russia

CONTENTS

THEORETICAL FOUNDATIONS AND SPECIFICITY OF MATHEMATICAL MODELLING

Neural network approaches for a facility location problem
Vladislav Haralampiev 3

Address sequence generator for memory BIST investigation
Mikalai Shauchenka 7

Nagata patch interpolation for finite volume mechanical contact simulations
Ivan Batistić, Željko Tuković, Philip Cardiff, Peter De Jaeger 9

MATHEMATICAL MODELLING OF TECHNOLOGICAL PROCESSES AND SYSTEMS

Modeling and simulation of forging processes
Bojan Mitev, Atanas Kochov 13

Buckling analysis of columns made of functionally graded materials via Rayleigh-Ritz method
Domagoj Lanc, Ivana Ivančić, Mihael Katalenić 18

Mechanical and hydraulical stability of the offshore composit structure
Klodian Gumeni, Jorgaq Kaçani, Klodian Dhoska 22

Optimization of pneumatic vane motor based on mathematical modeling and computer si-mulation
Spartak Poçari, Andonaq Londo 26

Study the work of specialized car service as queue theory
Grozev D., Milchev M., Georgiev I. 31

Determination of empirical coefficients of heat dissipation characteristics by optimization methods for a spark-ignited car engine
Pavel Bolotov, Lloyd Rexford Neuburg 35

MATHEMATICAL MODELLING OF SOCIO-ECONOMIC PROCESSES AND SYSTEMS

On the distribution of the incentive fund at the university
Irina Mamaeva 39

Neural network approaches for a facility location problem

Vladislav Haralampiev

Faculty of Mathematics and Informatics – Sofia University "St. Kliment Ohridski", Bulgaria

vladislav.haralampiev@gmail.com

Abstract: *This paper examines the possibility to use neural networks for approximately solving the MiniSum problem, a classic facility location problem. For this we first create a set of realistic MiniSum instances, based on the Bulgarian road network. Two standard neural network approaches – Hopfield networks and Boltzmann machines, are then applied to the instances. Since the quality of solutions is not satisfactory, the reasons for the poor performance are discussed. An improved neural network approach is then proposed. This approach has excellent performance on the MiniSum instances. It always finds solutions just several percent worse than the optimum, and is often able to find the exact optimum.*

Keywords: FACILITY LOCATION, NEURAL NETWORKS, COMBINATORIAL OPTIMIZATION

1. Introduction

Facility location problems are a large class of optimization problems, often occurring in practice. In this paper we are interested in the MiniSum problem, a classic facility location problem. MiniSum models the search for optimal placement of a set of warehouses with goal to minimize transportation costs. We give a formal definition of the problem in the next section.

The interest in using neural networks for approximately solving optimization problems started from the seminal paper of Hopfield and Tank [3]. They propose a certain type of network, which is able to find solutions to the Travelling salesman problem. This network can be generalized to many combinatorial optimization problems. It is also implementable in hardware and is naturally massively-parallel, which makes the whole approach interesting for solving large instances. Sadly, the Hopfield-Tank (HT) approach has problems. As noted in [8] and in many other places, the approach does not scale to large instances and the quality of the solutions it produces is bad. There were many efforts to improve the HT approach. One promising direction are Boltzmann machines (further denoted BM), which add randomness to the network operation.

Neural networks for combinatorial optimization may be interesting from theoretical perspective, but if such approaches produce low-quality solutions, they will have no practical value. We start by generating a set of realistic MiniSum instances, based on the Bulgarian road network. We then apply the HT approach and BM to the instances and confirm that the quality of the solutions they give is not satisfactory. After analyzing the reasons for the poor performance, we propose an improved approach, which has excellent performance on the MiniSum instances. On average it finds solutions just 0.3% worse than the optimum and in 88% of the cases it finds the exact optimum. This confirms that asynchronous massively-parallel systems of "neurons" can be used to produce high-quality solutions to combinatorial optimization problems. The reasons for the poor performance on HT and BM are in their specifics, not in the idea of using such systems of "neurons".

2. The MiniSum problem

Intuitively, we are given a directed, weighted graph. Nodes represent populated places and edges represent roads. We need to choose k nodes from the graph where to locate warehouses. The goal is to minimize the sum of distances from each populated place to the closest warehouse.

2.1 Formal definition

The k-MiniSum problem is defined over a directed, weighted and strongly connected graph $G(V, E)$ with vertex set V and edge set E. The shortest distance in G between two vertices U and W is denoted as $dist(U, W)$. Integer k is a parameter of the problem and is usually much less than the number of vertices.

Definition *(k-MiniSum problem)*

Find a list of k vertices $V_1, V_2, \ldots V_k$ from V which minimize $\sum_{U \in V} \min_{V_i \in V_1 \ldots V_k} dist(U, V_i)$

The k-MiniSum problem in general graphs is well-known to be NP-hard (by reduction, for example, from the Set cover problem [4]).

2.2 Test instances

The Bulgarian road network is used to generate realistic MiniSum instances. For each instance a rectangular area is selected. All populated places and roads in this area are extracted and used as underlying graph. We choose the areas so that there are between 20 and 90 populated places and set the number of facilities to a value between 2 and 6. The instances are small enough to be able to exactly compute the optimal solution in reasonable time. As source of geographic data OpenStreetMaps [6] is used (data is extracted using SPARQL queries). For computing the exact solution each instance is modelled as integer programming problem and solved using the Cbc mixed integer programming solver [1]. In total we have selected 50 different rectangular areas, which gives 250 MiniSum instances. The image below shows one of them.

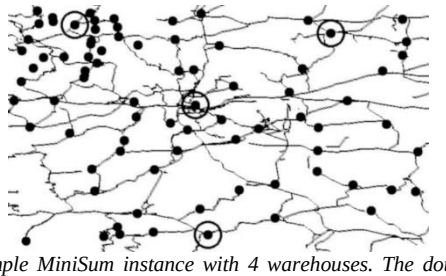

Fig. 1 *Example MiniSum instance with 4 warehouses. The dots represent populated placed and the 4 selected locations are marked with additional circular outline.*

3. Existing neural network approaches

Good description of combinatorial optimization using Hopfield networks can be found in [7], and using Boltzmann machines – in [5]. The two approaches have a lot in common. In fact, Boltzmann machines can be thought of as stochastic version of Hopfield networks. Both approaches assume a binary problem is given. There is a set of n binary variables $V_1, V_2 \ldots V_n$, an n x n weight matrix W and a weight vector D. The approaches find a local minimum of the function $\sum W_{ij} V_i V_j - \sum D_i V_i$ (called the energy function). To approximately solve a combinatorial optimization problem we need to choose a weight matrix and weight vector such that local minima of the energy function correspond to good solutions of the problem. We call this step encoding. It should be noted that there are requirements, which matrix W should meet (described in [7]). Usually, when encoding a problem, the requirements are naturally met.

Clearly, there are many ways to encode the MiniSum problem. Next, one possible way, inspired by the encoding of other problems in [7] and [8], is described. We believe that the encoding is reasonable, but there is a possibility for another encoding, giving better results, to exist.

Let n be the number of vertices in G and k be the number of warehouses we need to place. The neural network encoding has $2 \cdot n \cdot k$ binary variables. We call one group of $n \cdot k$ variables the client – facility variables and denote them as $CF[i,j]$. $CF[i,j]$ is 1 iff the client in vertex i is serviced by facility (warehouse) number j. Similarly, another group of $n \cdot k$ variables correspond to the facility – location relation. We denote them as $FL[j,s]$ and $FL[j,s]$ is 1 iff facility j is located in vertex s. The transportation cost can now be expressed as $\sum_{i,j,s} CF[i,j] \cdot FL[j,s] \cdot dist(V_i, V_s)$, which is in a form, compatible with the energy function notation. Fig. 2 illustrates the encoding.

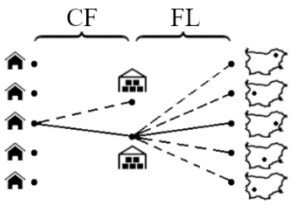

Fig. 2 *MiniSum encoding. Note that the binary variables correspond to edges (not all edges are shown). Dashed edges stand for variables with value 0, solid edges – with value 1. Solid edges connect a client with its facility and a facility with its location.*

For a solution to be valid, each client should be serviced by only one facility, and each facility should be located in only one vertex. The typical approach to achieve this 1–of–many constraint with neural networks is to add penalty terms to the energy function. Similarly to [7] and [8] we add to the energy function a group of penalty terms of the form $A \cdot \left(1 - \sum_j CF[i,j]\right)^2$ for each client i. When A is large enough, these terms force the network to choose exactly one facility for each client. We analogously add term of the form $B \cdot (1 - \sum_s FL[j,s])^2$ for each facility j to enforce the other 1–of–many constraint. Note that, when the brackets are open, the expressions are in a form, compatible with the notion of energy function. Choosing the values A and B is not straightforward and it affects the quality of the produced solution. The need to choose weights for the penalty terms is considered to be a major problem of the HT approach. Later in this section we will describe our approach for choosing the weights.

The problem encoding tells us how to construct, given a MiniSum instance, the set of binary variables, the weight matrix and weight vector. Variables are then mapped to simple computing units (neurons). Each unit corresponds to a variable. It has an output value equal to the value of the variable. The units are also connected to each other, matrix W gives the weights of the connections. Each unit has a procedure for updating its output, the procedure is different between HT and BM. The whole system of units starts from a random state (random output for each unit) and repeatedly chooses a unit and executes its update procedure. After enough time has passed, we read the output values of the neurons and this is the final solution. Again, the encoding tells us how to translate from the values of the binary variables V_i to the objects of the initial problem. In the case of the described encoding, the variables with value 1 tell which facility services each client and where each facility is located.

3.1 Hopfield network updates

Assume unit S wants to perform an update. It computes the value $inp[S] = \sum_j W[S,j] \cdot output[j]$. If $inp[S] < D[S]$ the unit sets its output to 1, otherwise it sets the output to 0. This computation is equivalent to checking the sign of the gradient of the energy function with respect to $output[S]$. The unit chooses the value of its output so that the energy function does not increase.

3.2 Boltzmann machine updates

In BM there is a notion of temperature. The temperature T controls the probability of accepting a change of the unit's output. Assume unit S wants to perform an update. It computes D, the difference in the energy function if we flip the output of S. If $D < 0$, S flips its output. Otherwise it flips its output with probability $\left(1 + e^{D/T}\right)^{-1}$.

It can be noticed that, when the temperature T is high, almost any change is accepted with high probability. When T is low, only changes which decrease the energy function are accepted. In this sense, when T is low, BM operates very similarly to a HT network. Temperature T gradually decreases with time. It starts from a value high enough to allow almost any change to be accepted (with high probability). Then every M steps it is multiplied by a constant a little less than 1 (where M is chosen to be proportional to the number of units).

3.3 Choosing penalty weights

Penalty terms were introduced to guarantee the validity of the solution. When their weight is too small, the system can arrive at a local minimum, in which a client is not connected to any facility, or no location is chosen for a facility. If the penalty weights are too high, they will dominate the energy function and will drive the system into a state representing a valid, but low-quality solution. Our approach to choosing the weights is to try to make them as small as possible. For this we first start from small values. We then repeatedly double the weights and run the network optimization procedure, until the network finds a valid solution. After this we repeatedly try to decrease the weights by a small fraction (10% or 5%) until the system still finds valid solutions. Actually, since in our encoding there are two separate weights (denoted A and B), we alternate between them in the decreasing steps.

3.4 Discussion on the performance

Here by performance we mean the quality of the solution. Since in both HT and BM there is some randomness, multiple runs were performed. More specifically, the described procedure for choosing penalty weights by itself performs multiple runs with different weights. Also, multiple runs were performed with the best weights found. In total this gives several hundred runs of the optimization procedure for each instance. The best solution found during the runs is selected.

The results of both HT and BM are very discouraging. While they are always able to find valid configurations, on average they find solutions more than two times more expensive than the optimum. The results of BM are slightly better than HT, but the runtime is significantly longer. Also, the cost of the found solutions just slightly decreases when increasing the number of facilities. And the quality of the solutions is not much better than a random solution. This points that both HT and BM put emphasis on finding valid solutions and almost do not optimize for solution quality.

It can be noticed that both HT and BM are variations of local search. They operate on a set of M binary variables and find local minimum in a solution space of size 2^M by starting from a random state and iteratively improving it. Local search is a well-researched area and is the base of many of the best-performing general approaches for (approximately) solving combinatorial optimization problems. Good overview of local search methods and their performance is [2]. We can borrow ideas from the analysis of local search methods to understand the problems with HT and BM, and improve their performance.

Neighbourhood

To choose the next state, local search performs small modifications of the current. The states, reachable from the current state in one modification step, are called its neighbours. The performance of local search highly depends on the neighbourhood definition, at least because local minimum is defined with respect to

a neighbourhood. For HT and BM the neighbourhood is formed by flipping one binary variable. This seems to be not flexible enough. Flipping one variable changes the validity of the current solution, which makes the penalty terms a major factor for deciding whether to accept a solution. Once a facility is connected to a location, for example, it becomes hard to change the location. The neighbourhood puts more emphasis on finding a valid solution than on finding a good solution. This may be a problem of our encoding of MiniSum. Yet, the mechanics of HT and BM seem to not be able to represent better neighbourhoods without excessive redundancy in the encoding.

Solution space

Since MiniSum is a hard problem, it is expected that the solution space is complex. But the penalty terms in the energy function create additional problems. It was already noted that choosing weights for the penalty terms is not straightforward. With respect to the solution space, the penalty terms create many (possibly poor) local minima from which it is hard to escape.

Randomization

Randomization often improves the quality of the solutions, found by local search. One common way to add randomization is to allow the search to occasionally accept modifications, which decrease the quality of the solution. This is done in an effort to escape from poor local minima. Since HT always decreases the value of the energy function, in this sense the method is completely deterministic. There is a historic explanation for this – Hopfield networks were developed as associative memory, not as machinery for optimization. Because of their determinism, we can expect HT to perform worse than stochastic local search.

BM allow transitions, increasing the value of the energy function. In this sense, they are better than HT. In fact, there is a theoretical result that, given enough time, BM will find the optimal solution (in probabilistic sense). But the time necessary for this is larger than the time for iterating through the whole solution space, so the result has little practical value.

Summary

As summary, the poor performance of HT and BM seems to follow from a combination of the penalty terms as mechanism for enforcing solution validity and the inflexible neighbourhood definition. For the HT approach there is the additional drawback of complete determinism (in the sense of the previous paragraph).

4. Proposed neural network approach

The proposed model uses the same binary variables CF and FL as in the already described MiniSum encoding. It minimizes the function $\sum_{i,j,s} CF[i,j] \cdot FL[j,s] \cdot dist(V_i, V_s)$. Note that there are no penalty terms in this function, another mechanism will be used to guarantee the validity of the solution. The binary variables are again mapped to units which have outputs, equal to the value of the corresponding variable. The whole system repeatedly updates the outputs of the units, same as the HT and BM approaches.

The units in the proposed approach have two more properties. Lets say that units X corresponds to the variable V_x. Then:

• $group[X]$ is a list of units which, intuitively, compete with X for activation. Eventually only one of the units in the group will have output equal to 1 (will be on). This is the mechanism for enforcing solution validity.

• $con[x]$ is a list of pairs of unit and weight (real number). This list represents the units to which X is connected (similarly to the W matrix in section 3).

The groups in the encoding naturally correspond to the 1-of-many constraints. Each client needs to be connected to exactly one facility, so for a $CF[i,j]$ (client - facility) unit its group is $\{CF[i,t] \mid t \in 1 \dots k\}$. Here k is the number of facilities. Similarly, for a $FL[j,s]$ (facility – location) unit its group is $\{FL[j,t] \mid V_t \in V\}$. This is because each facility needs to be located in exactly one vertex of the graph.

Connections in the encoding are only between $CF[i,j]$ and $FL[j,s]$ units. More specifically, $CF[i,j]$ is connected to $FL[j,s]$ with weight $dist(V_i, V_s)$. Similarly, $FL[j,s]$ is connected to $CF[i,j]$ with the same weight. Here i, j and s iterate through all valid values. This also has very natural interpretation – if client i is serviced by facility j ($CF[i,j]$) which is located in vertex s ($FL[j,s]$) then we pay $dist(V_i, V_s)$ for transportation.

As in Boltzmann machines, there is a notion of temperature T, which controls the probability of accepting transitions. This temperature decreases exponentially and can be either local for each unit, or global for the whole system.

If unit X wants to update its output, it first finds the set of units which have value 1 and are connected to X. Lets call this set ON. If ON is empty, X sets its output to 1. Otherwise, X computes $value[X] = (\sum_{e \in ON} weight[e]) / |ON|$. Here weight is the weight of the connection to the corresponding unit. X also computes $BEST = min\{value[s] \mid s \in group[X]\}$. The unit sets its output to 1 if $value[X] < BEST$, else it sets it to 0. After this X flips its output with probability $\left(1 + e^{\frac{|BEST - value[x]|}{T}}\right)^{-1}$

The operation of the system consists of a sequence of updates of unit outputs (starting form a random state). Assume there are M units in total. The sequence of updates is of size $5M^2$ and is separated into M groups. After each group the temperature T is multiplied by a constant C, which is chosen so that after the M groups T becomes 0.001 (the initial temperature is chosen as the maximum energy delta of a variable flip according to the initial random state). Each group of updates consists of $5M$ individual ones, in each of which we randomly choose a unit and update its output, as we already described.

Note that, when the temperature is low, the way we process groups guarantees the validity of the solution and the arrival at a local minimum of the energy function. Additionally, on higher temperatures there is a large probability to be in states, in which a facility is connected to multiple locations, or a client is connected to multiple facilities. Taking average in the value computation is done to increase exploration by allowing cheap "drifting" of the chosen location to neighbouring ones.

Since there is randomness in the system's operation, it makes sense to perform multiple runs. In our experiments we performed 4 independent runs for each instance and took the best solution found. Actually, most of the time one run was enough to find the optimal solution.

On the test MiniSum instances the described approach is able to find the exact optimal solution in 88% of the cases and achieves average error of 0.3%. By error we mean the difference (percentage) between the returned solution and the optimal solution. The maximum error on an instance is 8%, the next largest is 2%. We haven't tuned the parameters of the described model, so probably it is possible to achieve slightly better results. Also, it is worth nothing that, even on our small-sized MiniSum instances, the proposed approach is much faster than both the integer programming approach and BM.

5. Conclusion

We created a set of realistic MiniSum instances and proposed a general neural network approach for facility location, which has excellent performance on the instances. This shows that massively parallel systems of "neurons" can find good quality solutions to combinatorial optimization problems. Apart from being theoretically interesting, such systems allow for efficient distributed implementation. There are also developments in special hardware for neural networks, which can significantly decrease the time of

the computation. As future work it is left to analyze the convergence properties of the proposed approach and to evaluate it on other facility location problems and combinatorial optimization problems with 1-of-many constraints.

References

[1] "Cbc (Coin-or branch and cut) mixed integer linear programming solver", https://github.com/coin-or/Cbc

[2] Hoos H. H., Stützle T., "Stochastic Local Search: Foundations and Applications", The Morgan Kaufmann Series in Artificial Intelligence, 2005.

[3] Hopfield J. J., Tank D. W., "Neural Computation of Decisions in Optimization Problems", Biological Cybernetics, 52 (1985) 141-152.

[4] Karp R. M., "Reducibility among Combinatorial Problems", Complexity of Computer Computations. The IBM Research Symposia Series, Springer, Boston, 1972.

[5] Korst J.H.M., Aarts E.H.L., "Combinatorial optimization on a Boltzmann machine", J. of Parallel and Distributed Computing, Vol. 6, pp. 331–357, 1989.

[6] OpenStreetMap contributors (2015). Planet dump [Data file from 27/12/2019]. Retrieved from https://planet.openstreetmap.org.

[7] Rojas R., "Neural Networks – A Systematic Introduction", Springer-Verlag, 1996.

[8] Wilson G. V., Pawley G. S., "On the stability of the Travelling Salesman Problem algorithm of Hopfield and Tank", Biological Cybernetics, 58 (1988), 63-70.

Address sequence generator for memory BIST investigation

Mikalai Shauchenka
Lichtenbergschule Darmstadt
nik.sh.de@gmail.com

Abstract: *In this paper a method of construction of a generator for address sequences with given values of switching activity, based on the Idea of Antonov and Saleev and with use of Toeplitz and Hankel matrices, was proposed. The broad possibilities of this approach and the limitations associated with conflicting requirements for the values of the rows of the matrix and their linear independence are shown. Examples of the formation of standard address sequences used for self-testing of storage devices are described.*

Keywords*: ADDRESS SEQUENCES, MBIST, SWITCHING ACTIVITY, QUASI-RANDOM SEQUENCES*

1. Introduction

The memory devices of modern *System-on-a-Chip* take up the biggest portion of the area overhead occupied by modern systems [1, 2]. As a result, memory Built-In-Self-Tests (MBIST) have become a common practice in research and application [2, 3]. Modern *memory* BIST play a crucial role in providing embedded memory of high quality, regardless of the size and level of its architecture. Traditionally, a *memory* BIST based on march algorithms for testing consists of a number of march elements with a given memory cell address sequence [3, 4]. To achieve high fault coverage, a memory cell address generator types various sequences [5, 6], and can take between 26% and 33% of the whole MBIST [3].

In this paper an address sequence generator for the implementation of MBIST, based on an application of the Antonov and Saleev method [7, 8] is considered. As shown in [6], the occupied area overhead and performance are key properties of such a generator. To significantly reduce the area overhead that is required to store the generating matrix from m^2 binary memory cells down to $2m–1$ binary cells, the use of special forms of generating matrices like the *Toeplitz matrix* and *Hankel matrix* [6] is justified.

The most common property of an address sequence that is used to test memory devices is the switching activity [1, 2, 3, 4]. Based on the specific of the generating matrices the properties of the address sequences generated according to them are investigated

2. Mathematical model

Let`s consider the address sequence $A(n) = a_m(n)\ a_{m-1}(n)\ a_{m2}(n)\dots\ a_2(n)\ a_1(n)$, where $a_i(n), \in\{0, 1\}$; $i\in\{1, 2, \dots, m\}$ and $n\in\{0, 1, 2, \dots, 2^m - 1\}$ as a m-dimensional vector that consists from 2^m m-dimensional binary vectors in binary space. Now the problem of generating the necessary address sequence can be regarded as the generation of m-dimensional binary vectors $A(n)$ according to the procedure of generating elements of the binary space [6]. The foundation of the m-dimensional binary space is the set of linearly independent vectors $\{V_1, V_2, \dots, V_m\}$, $V_i = v_{i1}\ v_{i2}\dots\ v_{im}$, $v_{ij}\in\ \{0,1\}$ that allows to generate the whole binary vector space (all of the 2^m binary vectors) through their linear combinations:

$$A(n) = V_1 b_1(n) \oplus V_2 b_2(n) \oplus V_3 b_3(n) \oplus \dots \oplus V_m b_m(n). \quad (1)$$

The binary coefficients $B(n) = b_m(n)\ b_{m-1}(n)\ b_{m-2}(n)\ \dots\ b_2(n)\ b_1(n)$; $b_i(n)\in\{0, 1\}$, $I\in\{1, 2, \dots, m\}$ form (1) represent the whole set of 2^m binary vectors. Then the vector space $A(n)$ generated according to (1) is of dimension m and consists of 2^m vectors. So, the vectors $A(n)$ can be used as an address sequence [6]. An effective modification of the classic model (1) for the generation of address sequences was proposed by Antonov and Saleev in [7] and was applied in practice for the generation of address sequences [5, 6, 7]. The essence is the use of the Gray Code sequence to transform the classic relation (1) into a recursive relation with two operands. The main element of such an approach is the basis $\{V_1, V_2, \dots, V_m\}$ that is represented by a generating square matrix W of size $m\times m$. The matrix can have any entries. The only restricting factor is the linear independence of the set of vectors V_i [6]. To reduce the area overhead required for storing the matrix W and to assure their maximum rank, an original method for generating matrices of special types like the Hankel matrix and the Toeplitz matrix was proposed [6].

3. Switching activity

To judge the properties of the address sequences $A(n) = a_m\ a_{m-1}\ a_{m-2}\ \dots\ a_2\ a_1$, generated with Antonov´s and Saleev´s method, the new metric $F(a_j)$, $j\in\{0, 1, 2, \dots, m–1\}$ was introduced. It defines the number of switches (changes) of the j-th bit of a_j in such a sequence. The deciding factor for the judgement of the switching activity is the type of the generating matrix W, as shown in [5]. In the case of the Toeplitz matrix, the basis v_i of the matrix W is presented by a Set of linearly dependent binary vectors constructed from $2^m–1$ binary values $v_1, v_2, \dots v_{2m-1}$ (2).

$$W = \begin{vmatrix} v_m & \cdots & v_3 & v_2 & v_1 \\ v_{m+1} & \cdots & v_4 & v_3 & v_2 \\ v_{m+2} & \cdots & v_5 & v_4 & v_3 \rightleftarrows \\ \cdots & \cdots & \cdots & \cdots & \cdots \\ v_{2m-1} & \cdots & v_{m+2} & v_{m+1} & v_m \end{vmatrix}. \quad (2)$$

For a generating matrix W and an arbitrary value j the value of the metric will be calculated by the expression (3).

$$F(a_j) = \sum_{i=1}^{m} v_{i-1+j}\, 2^{m-i}. \quad (3)$$

The maximum value $maxF(a_j)$ and minimum value $minF(a_j)$ of this property, taking the values of $2^m–1$ and 1 respectively, are equal to the corresponding values for a generating matrix with linear independent vectors v_i [5]. However, in this case an even greater correlation between the switching activities of the digits of the address sequence can be observed. So, all the entries of the m-th column of the matrix W being equal to 1, namely $v_1 = v_2 = \dots = v_m = 1$, ensure the maximum switching activity of $2^m–1$ of the digit a_1 of the address sequence $A(n)$. Respectively, the switching activity of the m-th digit of an cannot be less than 2^{m-1}, since for the first column of the matrix $v_m = 1$ and the switching activity of the m−1-th bit is equal to $2^m–2$ ($v_{m+1}= 0$).

Based on the specific of the generating matrix W (2), namely the structure of its rows, the integral measure of the switching activity for the number sequence can be calculated by this expression:

$$F(A) = \sum_{i=1}^{m} 2^{m-i} \sum_{j=1}^{m} v_{j-1+i} \quad (4)$$

The second sum in relation (4) represents the number of ones in the *i*-th row of the matrix (2). For the general case considered in (5), the switching activity $F(A)$ (4) of the address sequence $A(n)$ takes the minimum value for the Gray Code sequence [6] that is determined by the matrix type (2). Then, for a matrix that consists out of m different rows, each containing one entry 1, we have $\min F(A) = 2^m - 1$ according to (4). The highest estimate of $F(A)$ is also uniquely defined by the type of the generating matrix [6] that in this case has only entries 1 in the first row and one zero in all the other rows. Then

$$max\ F\ (A) = 2^{m-1}m + \left(\sum_{i=2}^{m} 2^{m-i}\right)(m-1) = 2^{m-1}m + (2^{m-1} - 1)(m-1) = 2^m m - 2^{m-1} - m + 1 \quad (5)$$

The given estimates of the switching activity of $F(a_j)$ and $F(A)$ are fair for the Toeplitz matrix (2) as well as for the Hankel matrix. The range of possible values of the specified characteristics is defined by the maximum and the minimum values and shows the possibility of generating address sequences with given values for these characteristics.

4. Standard address sequences

The main generalized mathematical model (1) and it´s modifications considered in the previous sections is the generating matrix W on which the main properties of the address sequences and their subsets depend. For the implementation of a memory BIST the generator should generate at least a subset of these sequences, since their combinations have characteristic properties that are closely related to the possibility of memory fault discovery [1, 3, 4]. The considered method for generating address sequences allows to generate a huge number of address sequences, having an estimated maximum of 2^{2m}, out of which the standard sequences take up an important portion [3]. The set of of such sequences includes: linear sequences; Gray Code sequences; sequences of the Complement type; sequences of the Limited type; sequences with hamming distance equal to 1 for all pairs of addresses; and a number of other sequences.

Let`s consider the generation with the proposed method of the most important and widely used address sequences listed in [3] and shown in table 1 in the form of their generating matrix W.

Linear address sequences A(n), also called counting sequences, are the main sequences in the sequence family for memory BIST. An example of such a sequence is shown in table 1, for the case of m = 4, in form of a generating matrix W, that is a Hankel matrix. For minimal load during the test, sequences with minimum switching activity are used. Out of these sequences, the Gray Code sequences stand out.

In the general case, the generation of address sequences with minimum switching activity is performed with a matrix *W* with minimum amount of zero values. Both the Hankel matrix with a diagonal of ones or the Toeplitz matrix with the main diagonal consisting of ones (see table 2) can be used for this purpose. At the same time, the maximum load during testing requires the maximum switching activity of the address sequences. For this purpose, the *Complement* sequences and the *Limited* sequences often find use. As can be seen from table 1, the maximum value of the switching activity is achieved by the maximum number of nonzero values in the generating matrix *W*. Indeed, for sequences of the *Limited* type, the number of nonzero values in the matrix w reaches the maximum possible value for matrices of maximum rank of $m^2 - m + 1$. which provides the ultimate switching activity. For both cases the Toeplitz and the Hankel matrices can be used. Address sequences with a hamming distance of one for all pairs of addresses [3] can be only generated for the case of $i = m - 1$ with the Toeplitz matrix (see table 1 for an example where $m = 4$) and for $i = 0$ with the Hankel matrix. The proposed method allows to generate a large set of *quasi-random* sequences [8] with the use of different Toeplitz matrices. An example of such a matrix is shown in table 1. It should be noted that the maximum rank of the matrix *W* is a necessary condition for all of the reviewed cases

Table 1. Generating matrices for standard address sequences

Linear	*Gray Code*	*Complement*
$\begin{vmatrix} 0 & 0 & 0 & 1 \\ 0 & 0 & 1 & 1 \\ 0 & 1 & 1 & 1 \\ 1 & 1 & 1 & 1 \end{vmatrix}$	$\begin{vmatrix} 1 & 0 & 0 & 0 \\ 0 & 1 & 0 & 0 \\ 0 & 0 & 1 & 0 \\ 0 & 0 & 0 & 1 \end{vmatrix}$	$\begin{vmatrix} 1 & 1 & 1 & 1 \\ 0 & 1 & 1 & 1 \\ 0 & 0 & 1 & 1 \\ 0 & 0 & 0 & 1 \end{vmatrix}$
Limited	$2^i = 8$	*Random*
$\begin{vmatrix} 1 & 1 & 1 & 1 \\ 0 & 1 & 1 & 1 \\ 1 & 0 & 1 & 1 \\ 1 & 1 & 0 & 1 \end{vmatrix}$	$\begin{vmatrix} 1 & 0 & 0 & 0 \\ 1 & 1 & 0 & 0 \\ 1 & 1 & 1 & 0 \\ 1 & 1 & 1 & 1 \end{vmatrix}$	$\begin{vmatrix} 1 & 0 & 0 & 0 \\ 0 & 1 & 0 & 0 \\ 1 & 0 & 1 & 0 \\ 1 & 1 & 0 & 1 \end{vmatrix}$

5. Conclusion

In this paper a method of construction of a generator for address sequences with given values of switching activity, based on the Idea of Antonov and Saleev and with use of Toeplitz and Hankel matrices, was proposed. The broad possibilities of this approach and the limitations associated with conflicting requirements for the values of the rows of the matrix and their linear independence are shown. Examples of the formation of standard address sequences used for self-testing of storage devices are described.

References

1. Bushnell, M. L. Essentials of Electronic Testing for Digital, Memory & Mixed-Signal VLSI Circuits / M.L. Bushnell, V.D. Agrawal. – New York: Kluwer Academic Publishers, 2000. – 690 p.

2. Wang, L.-T. VLSI Test Principles and Architectures: Design for Testability / L.-T. Wang, [et al.]. – Elsevier, 2006. – 808 p.

3. Goor, A.J. Optimizing memory BIST Address Generator implementations / A.J. Goor, H. Kukner, S. Hamdioui // Proc. of 2011 6th International Conference on Design & Technology of Integrated Systems in Nanoscale Era (DTIS), Athens, Greece – 2011. P. 572–576.

4. Yarmolik, V.N. Transparent Testing of Digital Memories / V.N. Yarmolik, I.A. Murashko, A. Kummert, A.A. Ivaniuk. – Minsk, Bielarus: Bestprint, 2005. – 230 p.

5. Yarmolik, V.N. Generation of address sequences with a given switching activity / V.N. Yarmolik, N.A. Shevchenko // *Informatics*. – 2020. – № 1(17), – pp. 7 - 23. (In Russ.)

6. Shevchenko, N.A. Generation of address sequences with a given switching activity / SSRG – IJCSE – November 2019

. Antonov, I.A. An economic method of computing LPτ-sequences / I.A. Antonov, V.M. Saleev // *U.S.S.R. Comput. Math. Math. Phys*. – 1979. – Vol. 19, № 1. – C. 252–256.

8. Yarmolik, S.V. Quasi-random testing of computer systems / S.V. Yarmolik, V.N. Yarmolik // *Informatics*. – 2013. – № 3(39), – C. 65–81. (In Russ.)

Nagata patch interpolation for finite volume mechanical contact simulations

Ivan Batistić [1], Željko Tuković [1], Philip Cardiff [2], Peter De Jaeger [3]
Faculty of Mechanical Engineering and Naval Architecture, Zagreb, Croatia[1]
University College Dublin, School of Mechanical and Materials Engineering, Belfield, Ireland[2]
NV Bekaert SA, Belgium[3]
ivan.batistic@fsb.hr

Abstract: *This paper describes a finite volume contact algorithm with surface smoothing using the Nagata patch interpolation. Nagata interpolation is derived from existing discretisation, using the mesh points positions and their calculated normal vectors. The contact between a deformable and a rigid body is analysed, whereas the rigid body is described with Nagata patch interpolation. Such approach allows a more accurate evaluation of the resulting contact stresses and forces.*
Keywords*: MECHANICHAL CONTACT SIMULATION, SURFACE SMOOTHING METHOD, NAGATA PATCH INTERPOLATION, FINITE VOLUME METHOD, FOAM-EXTEND*

1. Introduction

As the finite element method is a common approach in the numerical stress analysis, it is also the most developed and advanced numerical method for calculating mechanical contact problems [1]. Recently, the finite volume method has established itself as a noteworthy alternative to the widely used finite element method in the simulation of stress analysis problems. Since the finite volume method proved to be capable of resolving strongly non-linear fluid flow problems, it is successfully applied to non-linear solid mechanics problems [2, 3].

Although the development and application of the finite volume method for stress analysis problems began more than two decades ago, the mechanical contact applications are still limited. The first finite volume mechanical contact calculation algorithm is proposed in [4] for linear elastic solids, where the contact constraint is enforced using the Dirichlet-Neumann partitioned procedure. The proposed Dirichlet-Neumann partitioned procedure was appropriate for two-dimensional cases, but it showed substantial limitations in three-dimensional applications, where it was difficult to prevent unphysical stresses at the edge of the contact surface. Because of the mentioned limitations, a contact algorithm based on the penalty method is developed in [5]. The proposed algorithm is based on the explicit update of contact force calculated at mesh points using penalty method. The calculated contact force is imposed on boundary via Neumman boundary condition. The algorithm was originally developed for three-dimensional frictionless problems. The extension on problems with friction and large elastoplastic deformation is done in [2]. The proposed contact calculation algorithm showed good stability and accuracy for complex contact problems. In order to better describe the friction in metal forming processes, the algorithm is extended to consider the lubrication in [6]. The lubrication is modelled by the Reynolds lubrication equations and solved numerically using the finite area method.

Algorithms for calculating contact problems with the finite element method cannot be directly applied to the finite volume method. In the finite element method, the weak form of the equation is solved. The contact effects are introduced via additional contact term in the energy functional. Furthermore, the solution is obtained by minimizing the modified energy functional [1] with methods well known in the optimization theory, where the constrained minimization problem is converted into an unconstrained saddle point problem. The most usable optimization methods in contact mechanics are the penalty method, the Lagrange multiplier method and the Augmented Lagrangian method [1]. In the finite volume method minimization of the energy is not carried out because a strong form of governing equations is discretized. Furthermore, the contact is treated like boundary conditions and the contact force is explicitly updated for each iteration of the segregated solver. It is important to notice that for both numerical methods, the algorithms for calculating contact problems are incremental and iterative since contact surfaces are unknown.

The purpose of this study is the development of the surface smoothing method for the finite volume contact algorithm. For the surface smoothing, Nagata patch interpolation is adopted to accurately describe contact surface. The main advantage of the chosen surface smoothing method is that it can be carried out efficiently and locally. The proposed procedure is implemented and tested in the foam-extend open source library.

2. Mathematical model

For each bodie in contact the conservation of linear momentum is considered:

$$\frac{\partial}{\partial t}\int_{\Omega}\rho\frac{\partial \boldsymbol{u}}{\partial t}\,\mathrm{d}\Omega = \oint_{\Gamma}\boldsymbol{n}\cdot\boldsymbol{\sigma}\,\mathrm{d}\Gamma + \int_{\Omega}\rho\boldsymbol{b}\,\mathrm{d}\Omega, \tag{1}$$

where ρ is the density, $\boldsymbol{u}$ is the displacement vector, $\boldsymbol{\sigma}$ is the Cauchy stress tensor, and $\boldsymbol{b}$ is a body force per mass unit. With appropriate constitutive equation for each bodie, the eq. (1) is reformulated into updated or total Lagrangian form. After the finite volume discretisation, a system of linear algebraic equations is obtained and solved in a segregated manner using iterative solvers. Contact is introduced via Neumann boundary condition, where the contact constraints are enforced using penalty method. More details about finite volume discretisation and solution procedure can be found in [2, 3].

2.1 Contact constraints

The mathematical background of the contact problem is defined by the contact constrains. The contact constraints can be divided into normal and tangential constraints. Accordingly, the normal contact constrains describe the normal component of the contact force, whereas the tangential constraints describe the tangential component of the contact force. The normal contact constraints are formulated using the Karush-Kuhn-Tucker conditions, being stated as:

$$g_n \geqslant 0, \quad p_n \leqslant 0, \quad p_n g_n = 0, \tag{2}$$

which must hold for all points on contact surface. The first term in the eq. (2) represents the geometric impenetrability condition. The second term allows only compressive contact pressure p_n, whereas the third term is the complementarity condition. Tangential contact constraints are described by a friction law. Most famous and simplest friction law is Coulomb law, which is described by the following three conditions:

$$\|\boldsymbol{t}_t\| - \mu|p_n| \leqslant 0, \;\; t_t + \mu|p_n|\frac{\dot{\boldsymbol{g}}_t}{\|\dot{\boldsymbol{g}}_t\|} = 0, \;\; \|\dot{\boldsymbol{g}}_t\|\left(\|\boldsymbol{t}_t\| - \mu|p_n|\right) = 0, \tag{3}$$

where μ is the constant friction coefficient, $\dot{\boldsymbol{g}}_t$ tangential relative sliding velocity and $\boldsymbol{t}_t$ the frictional force vector. The first term in eq. (3) limits the frictional contact force, the second term defines its direction, whereas the third term is the complementarity condition. To conclude, the contact conditions, i.e. components of contact force, are described by nonlinear functions. Hence, they are the main source of the nonlinearity of contact problems.

3. Surface smoothing method

From the numerical point of view, the finite volume analysis of contact problems can be divided into two categories. First, the general category represents contact between deformable discretized bodies whereas the second category is the simplification in which one bodie is rigid. For contact problems with large difference between stiffness of the contact bodies, the stiffer bodie can be represented as a rigid. Such approach leads to less computational effort and can be used in the simulations of complex engineering problems like: metal forming processes, rubber seals, tyre on road, indentation tests [7, 8, 9]. The representation of rigid body surface can be done using analytical surfaces, piecewise linear discretisation or with parametric patches obtained with surface smoothing. The analytical approach is limited on simpler geometry, whereas piecewise discretisation poses some drawbacks when point projection is calculated. Using surface smoothing methods, rigid contact surface is accurately and continuously described using higher order interpolations. Although, various surface smoothing methods have been developed in the finite element method, the recently applied Nagata patch interpolation can be easily generalized and efficiently applied on arbitrary piecewise linear finite volume mesh topology.

3.1 Nagata patch interpolation

The Nagata patch interpolation was originally proposed by Nagata [10]. The interpolation is based on a quadratic polynomial, requiring only position and normal vectors at the nodes of the surface mesh. The features of the proposed interpolation algorithm allows its efficient and robust application on arbitrary mesh topology. It is important to note that the proposed formulation can handle discontinuity of normals, sharp edges and singular points. In the presented study the interpolation method is used on smooth rigid surfaces, discretized with triangular facets.

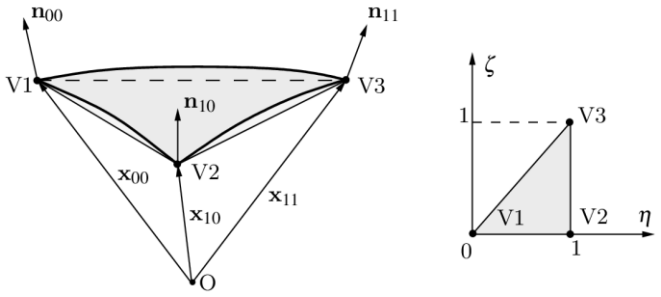

Fig. 1 *Nagata patch interpolation.*

For triangular Nagata patch (see Fig.1), the interpolated surface is given by the quadratic polynomial:

$$\boldsymbol{x}(\eta,\zeta)=\boldsymbol{c}_{00}+\boldsymbol{c}_{10}\eta+\boldsymbol{c}_{01}\zeta+\boldsymbol{c}_{11}\eta\zeta+\boldsymbol{c}_{20}\eta^2+\boldsymbol{c}_{02}\zeta^2, \tag{4}$$

where η and ζ are the local coordinates defined on the patch region, and satisfy the next condition:

$$0\leqslant\zeta\leqslant\eta\leqslant 1. \tag{5}$$

The coefficients in equation (4) are:

$$\begin{gathered}\boldsymbol{c}_{00}=\boldsymbol{x}_{00},\quad \boldsymbol{c}_{10}=\boldsymbol{x}_{10}-\boldsymbol{x}_{00}-\boldsymbol{c}_1,\quad \boldsymbol{c}_{01}=\boldsymbol{x}_{11}-\boldsymbol{x}_{10}+\boldsymbol{c}_1-\boldsymbol{c}_3\\ \boldsymbol{c}_{11}=\boldsymbol{c}_3-\boldsymbol{c}_1-\boldsymbol{c}_2,\quad \boldsymbol{c}_{20}=\boldsymbol{c}_1,\quad \boldsymbol{c}_{02}=\boldsymbol{c}_2,\end{gathered} \tag{6}$$

where $\boldsymbol{c}_1$, $\boldsymbol{c}_2$ and $\boldsymbol{c}_3$ are the vectors obtained with the edge interpolation. For each edge ($\boldsymbol{x}_{00}$, $\boldsymbol{x}_{10}$), ($\boldsymbol{x}_{10}$, $\boldsymbol{x}_{11}$) and ($\boldsymbol{x}_{00}$, $\boldsymbol{x}_{11}$), quadratic Nagata curve can be defined (see Fig. 2):

$$\boldsymbol{x}(\zeta)=\boldsymbol{x}_1+\left(\boldsymbol{x}_2-\boldsymbol{x}_1-\boldsymbol{c}\right)\zeta+\boldsymbol{c}\zeta^2 \quad \text{where} \quad 0\leqslant\zeta\leqslant 1. \tag{7}$$

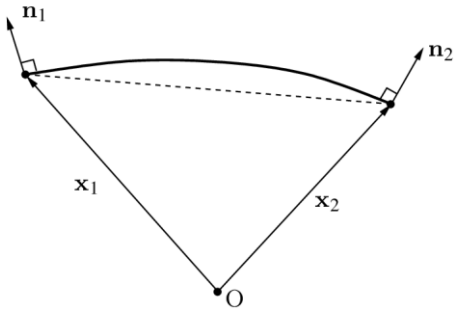

Fig. 2 *Nagata edge curve*

Vectors $\boldsymbol{x}_1$ and $\boldsymbol{x}_2$ are the position vectors of the edge end points, and $\boldsymbol{c}$ is the unknown coefficient vector. Coefficient vector c is calculated as:

$$\boldsymbol{c}=\begin{cases}\dfrac{[\boldsymbol{n}_1,\boldsymbol{n}_2]}{1-a^2}\begin{bmatrix}1 & -a\\ -a & 1\end{bmatrix}\begin{Bmatrix}\boldsymbol{n}_1\cdot(\boldsymbol{x}_2-\boldsymbol{x}_1)\\ -\boldsymbol{n}_2\cdot(\boldsymbol{x}_2-\boldsymbol{x}_1)\end{Bmatrix} & (a\neq\pm1)\\ 0 & (a=\pm1)\end{cases}, \tag{8}$$

where $a=\mathbf{n}_1\cdot\mathbf{n}_2$ and $[\cdot,\cdot]$ represent a matrix composed by two vectors. Equation (8) is derived from the assumption that the Nagata curve is orthogonal to the unit normal vectors $\boldsymbol{n}_1$ and $\boldsymbol{n}_2$ at points $\boldsymbol{x}_1$ and $\boldsymbol{x}_2$, respectively. For the parallel normal vectors ($a=\pm1$), the Nagata curve describes the linear segment, because of the zero coefficient vector $\boldsymbol{c}$. More details about the Nagata patch interpolation on triangular and quadrilateral patch can be found in the literature [11, 12].

3.2 Point normal calculation

In order to construct the Nagata patch, the calculation of normals at mesh vertices is conducted. The normal vectors at mesh points are estimated with normals from the point neighbouring faces. The calculation is done using the weighted average of the unit normal vectors of all neighbouring faces:

$$\boldsymbol{n}_{\mathrm{p}}=\frac{\sum_{i=1}^{n_f}\omega_i\boldsymbol{n}_{f,i}}{\left\|\sum_{i=1}^{n_f}\omega_i\boldsymbol{n}_{f,i}\right\|}. \tag{9}$$

In the presented study each neighbouring face contributes equally to the normal vector calculation (mean weighted equally). In the literature more advanced approach can be found, such as mean weighted by angle or mean weighted by areas of adjacent triangles [12].

4. Contact algorithm

The first part of the contact algorithm is the contact search. For each mesh point $\boldsymbol{P}$ of the deformable body potential Nagata contact candidates are identified. The potential contact candidates are calculated using the Axis Aligned Bounding Box quick rejection test. Such approach generates false candidates which are detected and eliminated using the Separation Axis Theorem algorithm. Using potential candidate list, for each contact point, the closest point projection is calculated for all candidates in order to find the minimal normal gap value. The relationship between the coordinates of contact point and closest point on Nagata patch is described with the following equation:

$$F^{\mathrm{proj}}(\eta,\zeta,g_n)=\boldsymbol{x}(\eta,\zeta)+g_n\boldsymbol{n}(\eta,\zeta)-\boldsymbol{P}=0, \tag{10}$$

where $\boldsymbol{P}$ denotes the contact point on the deformable contact surface, $\boldsymbol{x}$ closest point on the Nagata patch and $\boldsymbol{n}$ unit normal vector of the Nagata patch (see Fig 2). The patch normal vector is calculated as follows:

$$\boldsymbol{n}=\frac{\boldsymbol{t}_1\times\boldsymbol{t}_2}{\left\|\boldsymbol{t}_1\times\boldsymbol{t}_2\right\|}, \tag{11}$$

where $\boldsymbol{t}_1$ and $\boldsymbol{t}_2$ are surface tangents at point $\boldsymbol{x}(\eta, \zeta)$, defined as:

$$\begin{aligned}\boldsymbol{t}_1&=\frac{\partial \boldsymbol{x}}{\partial \eta}=\boldsymbol{x}_{10}-\boldsymbol{x}_{00}+\boldsymbol{c}_1\left(\left(\eta-\zeta\right)-\left(1-\eta\right)\right)+\left(\boldsymbol{c}_3-\boldsymbol{c}_2\right)\zeta,\\ \boldsymbol{t}_2&=\frac{\partial \boldsymbol{x}}{\partial \zeta}=\boldsymbol{x}_{11}-\boldsymbol{x}_{10}+\boldsymbol{c}_2\left(\zeta-\left(\eta-\zeta\right)\right)+\left(\boldsymbol{c}_1-\boldsymbol{c}_3\right)\left(1-\eta\right).\end{aligned} \tag{12}$$

The solution of $\boldsymbol{F}^{\text{proj}} = 0$ provides the local coordinate of the closest point $\bar{\boldsymbol{x}}$ on the Nagata patch. In order to solve the eq. (10) the Newton-Raphson method is used:

$$\boldsymbol{s}_{i+1}=\boldsymbol{s}_i-\left[\nabla \boldsymbol{F}^{\text{proj}}\left(\boldsymbol{s}_i\right)\right]\boldsymbol{F}^{\text{proj}}\left(\boldsymbol{s}_i\right), \tag{13}$$

where $\boldsymbol{s}_i=[\eta, \zeta, g_n]^T$ represents the solution vector at iteration i. The Jacobian matrix $\nabla \boldsymbol{F}^{\text{proj}}$ of the system of equations in the eq. (13) is defined as follows:

$$\nabla \boldsymbol{F}^{\text{proj}}\left(\eta,\zeta,g_n\right)=\left[\frac{\partial}{\partial \eta},\frac{\partial}{\partial \zeta},\frac{\partial}{\partial g_n}\right]\boldsymbol{F}^{\text{proj}}\left(\eta,\zeta,g_n\right). \tag{14}$$

In order to calculate the eq. (14) the gradient of the normal vector with respect to the local coordinates is evaluated using the Weingarten formula.

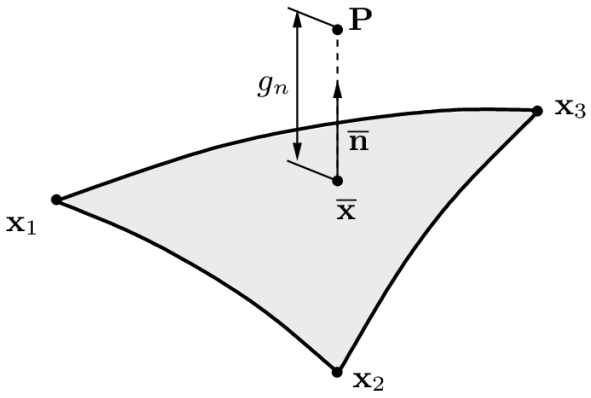

Fig. 3 *Closest point projection.*

For most cases solution of the eq. (13) is obtained with less than four iterations. With the obtained normal gap at mesh points, normal contact pressure is calculated using the penalty method, whereas the value at face center is obtained using the inverse distance interpolation.

2. Numerical examples

The proposed contact algorithm is implemented in the open-source foam-extend library as the extension to the work previously done by [2, 5]. The accuracy and efficiency of the proposed contact algorithm are tested via two numerical examples. The first example is a simple two-dimensional example of compressed cylinder tube with an exterior rigid tube. The second case is the finite element benchmark case initially proposed by Krstulović-Opara [13]. The examinated numerical examples comprise frictional and frictionless contact between rigid and deformable body, whereas the deformable body includes large deformation and large sliding. In both numerical examples, the Neo-Hookean material model is chosen for the deformable body. The results are compared with the current finite volume contact algorithm [2, 5], where the piecewise linear surface description is used.

5.1 Compressing cylindrical tube

Elastic cylindrical tube (Young's modulus E = 200 MPa, Poisson's ration υ = 0.3) with inner radius r_i =50 mm and thickness 15 mm, is initially overlapped δ= 1mm with exterior rigid cylindrical tube. Due to the symmetry of the problem, only 1/4 of the model is considered, which is discretized with 10 cells in radial and 40 cells in a circular direction. Rigid cylinder tube is discretised with two meshes (see Fig. 4), whereas mesh A consists of the same number of faces in the circular direction, resulting in accurate calculation of the normal gap at mesh points. At the contact interface, frictionless contact is assumed. From the Fig. 5 it can be seen that non-conformal discretisation on the contact interface produces stress oscillations, whereas application of surface smoothing produces results with a smooth distribution of radial stress.

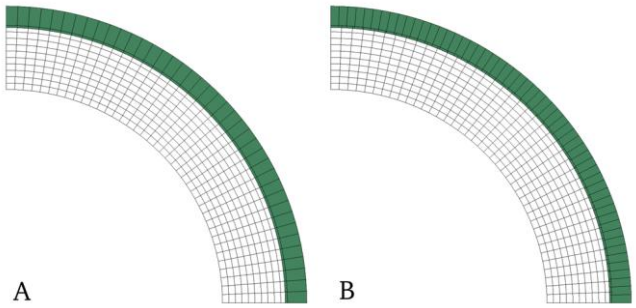

Fig. 4 *Cylindrical tube mesh: a) conformal, b) non-conformal discretisation at the contact interface.*

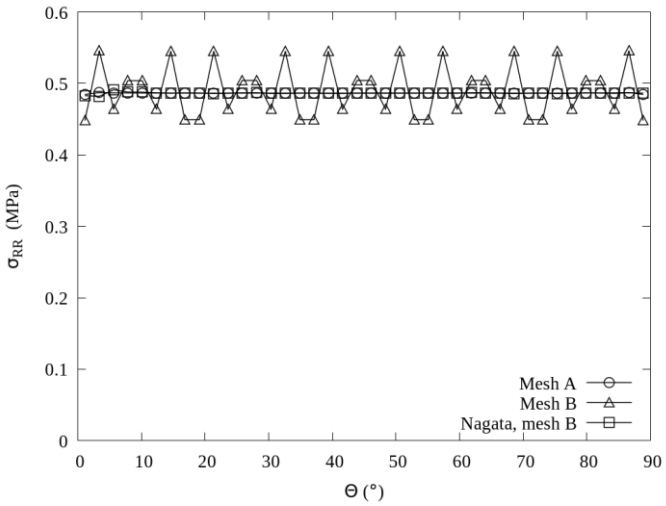

Fig. 5 *Radial stress distribution on the contact surface.*

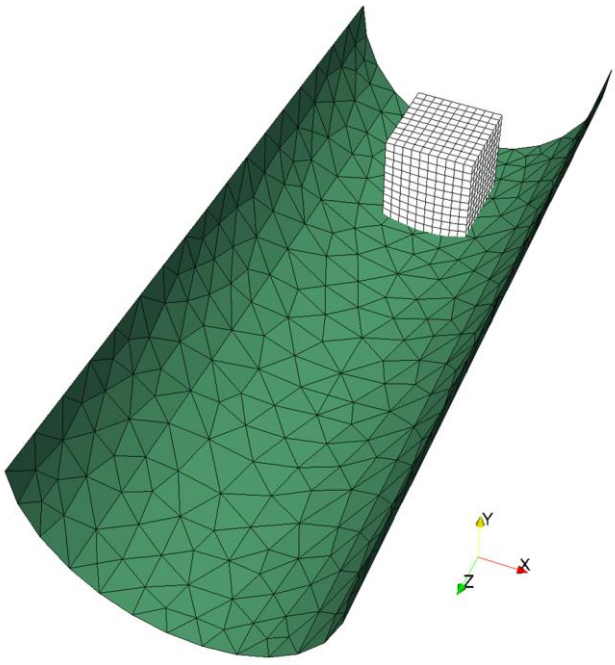

Fig. 6 *Unstructured mesh of a half-tube, 580 triangles (mesh A).*

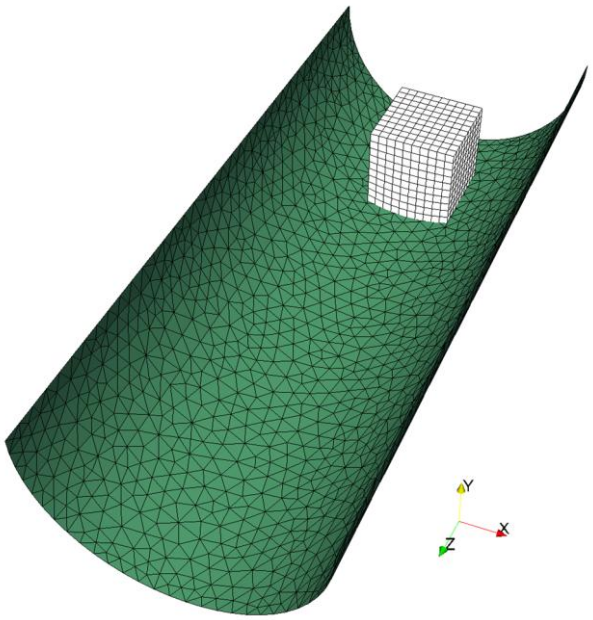

Fig. 7 *Unstructured mesh of a half-tube, 2442 triangles (mesh B).*

5.2 Cylindrical contactor sliding in a half-tube

This case represents the sliding of an elastic cylindrical contactor in a rigid tube. The cylindrical contractor dimensions are 2×2×2 with the curvature radius r=3 in the contact surface. The half-tube has a radius of r=3 and 15 units of length. The Young's modulus and the Poisson's ratio are defined as E=100 and υ=0.3, respectively. The friction is described with Coulomb friction law with coefficient of friction μ=0.1. The cylindrical contractor is uniformly discretized with 100 control volumes, whereas the rigid half-tube is discretized with unstructured mesh composed by 580 and 2442 triangles (see Fig. 6 and Fig. 7). At initial configuration the cylinder contactor overlaps rigid tube by δ=0.01 units. The axial displacement of 10 units in z direction is prescribed and solved via 100 equal increments. From Fig. 8 it is possible to conclude that coarse discretisation leads to bad force evolution because of the poor approximation of the cylinder surface geometry. Furthermore, finer discretisation produces results closer to ones obtained using surface smoothing. It is important to notice that the application of surface smoothing leads to approximately the same force evolution on both meshes studied. In this example, the average number of iterations per timestep is decreased for both meshes when mesh smoothing is used. Obtained results are in good agreement with [11] where the finite element method is used.

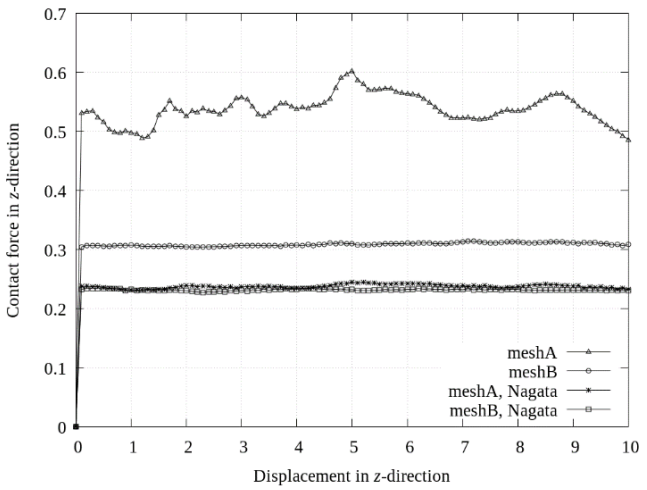

Fig. 8 *Comparison of the contact force as a function of displacement for piecewise linear and the smooth surface description of the half-tube.*

6. Conclusion

A patch smoothing procedure for the finite volume mechanical contact simulations is presented in this work. The implementation is done in the foam-extend framework, as the extension of the existing code developed for large deformation contact problems [2, 5]. The results are compared with the existing finite volume contact algorithm via two numerical examples. The results show that the Nagata patch interpolation allows more accurate evaluation of contact stresses. Furthermore, because of the continuous description of boundary, the force oscillations are reduced. For the future work, the efficiency and robustness of the current implementation will be tested and presented. Moreover, the implementation will be extended to handle the contact between deformable bodies.

7. Acknowledgements

Financial support via Ph.D. funding is gratefully acknowledged from NV Bekaert SA, Belgium.

8. References

1. P. Wriggers, Computational Contact Mechanics. Springer, **2**nd edition, (2006).
2. P. Cardiff, Ž. Tuković, P. DeJaeger, M. Clancy, A. Ivanković, A Lagrangian cell-centred finite volume method for metal forming simulation, International Journal for Numerical Methods in Engineering, **109(13)**, 1777-1803, (2017) .
3. Ž. Tuković, A. Karač, P. Cardiff, H. Jasak and A. Ivanković, OpenFOAM finite volume solver for fluid-solid interaction. Transactions of FAMENA, **42(3)**, pp.1-31, 2018.
4. H. Jasak, H. Weller, Finite Volume Methodology for Contact Problems of Linear Elastic Solids, Proceedings of 3rd International Conference of Croatian Society of Mechanics, Cavtat/Dubrovnik, 253-260, (2000).
5. P. Cardiff, A. Karač, A. Ivanković. Development of a finite volume contact solver based on the penalty method, Computational Materials Science, 283-284, (2012).
6. V. Škurić, P. De Jaeger and H. Jasak, Lubricated elastoplastic contact model for metal forming processes in OpenFOAM. Computers & Fluids, **172**, pp.226-240, (2018).
7. D. M. Neto, M. C. Oliveira, and L. F. Menezes, Surface smoothing procedures in computational contact mechanics, Archives of Computational Methods in Engineering **24.1,** 37-87, (2017).
8. M. Hachani and L. Fourment, 3D contact smoothing method based on Quasi-C1 interpolation, Trends in computational contact mechanics, **58**, 23-40, (2011).
9. T. Hama, T. Nagata, C. Teodosiu, A. Makinouchi and H. Takuda, Finite-element simulation of springback in sheet metal forming using local interpolation for tool surfaces. International Journal of Mechanical Sciences, **50(2)**, 175-192, (2008).
10. T. Nagata, Simple local interpolation of surfaces using normal vectors, Computer Aided Geometric Design, **22**, 327-347, (2005).
11. D. M. Neto, M. C. Oliveira, L. F. Menezes and J. L. Alves, Applying Nagata patches to smooth discretized surfaces used in 3D frictional contact problems, Computer Methods in Applied Mechanics and Engineering, **271**, 296-320, (2014).
12. D. M. Neto, M. C. Oliveira, L. F. Menezes and J. L. Alves, A contact smoothing method for arbitrary surface meshes using Nagata patches, Computer Methods in Applied Mechanics and Engineering **299,** 283-315, (2016).
13. L. Krstulović-Opara, P. Wriggers, and J. Korelc, AC 1-continuous formulation for 3D finite deformation frictional contact, Computational Mechanics, **29.1**, 27-42, (2002).

Modeling and simulation of forging processes

Bojan Mitev, Atanas Kochov
Faculty of Mechanical Engineering – Skopje, Rep. of North Macedonia
E-mail: bojanmitev77@gmail.com

***Abstract**: Forging is an experience-oriented technology. The physical phenomena that describe the forging operations are difficult to express with quantitative relationships. In order to avoid the trail-and-error method, we use numerical simulations for studying the forging process. With the help of these simulations, the engineers are able to uncover the potential defects which may happen during the forging process. Concurrent Engineering (CE) helps in making the forging process more effective. In the CE system, each modification of the product represents a taxonomical relationship between specifications, outputs, and the concept it represents. In the study, the forging process of a disc shaped part is analysed. Thanks to numerical simulations it is determined that the dimensions of the billet are larger than needed. This resulted in overfilling the flash of the tool, thus the simulation was unsuccessful. After correcting the dimensions of the billet, the simulation ran with no interruptions.*
***KEYWORDS**: FORGING PROCESSES, NUMERICAL SIMULATIONS, CONCURRENT ENGINEERING*

1. Introduction

In the forging process, initially a simple part – ingot is transformed into more complex part geometry, meanwhile, the tool forms the needed geometry and transfers pressure to the material which is deformed in the tool's interface. The forging processes usually produce little to none scrap and generate the final part geometry in a short amount of time, usually in one or a few strokes of a hammer or press. In addition, for a given weight, parts produced with forging show better mechanical and metallurgical properties than those produced by casting or machining. Forging is an experience-oriented technology. Throughout the years, a great deal of experience has been accumulated in this field, mainly through trial-and-error methods. Modern serial forging production is done with special forging tools. According to metal flow properties, closed-die forging can be done with or without flash; of the two, the latter is a more sophisticated method. Closed-die forging with hammers is done in a few strokes, whereas forging on a press is done in one slow stroke [1].

The physical phenomena that describe the forging operations are difficult to express with quantitative relationships. The material flow, friction between the tool and the material, the heat generation and transfer during the plastic flow, and the relationship between microstructure/properties and process conditions are difficult to predict and analyse. A forging system comprises all the input variables such as the billet (geometry and material), the tooling (geometry and material), the conditions at the tool/material interface, the mechanics of plastic deformation, the equipment used, the characteristics of the final product, and finally the plant environment where the process is being conducted. The key to a successful forging operation, to obtain the desired shape and properties, is the understanding and control of the metal flow [1].

2. Modeling and simulation of a forging tool

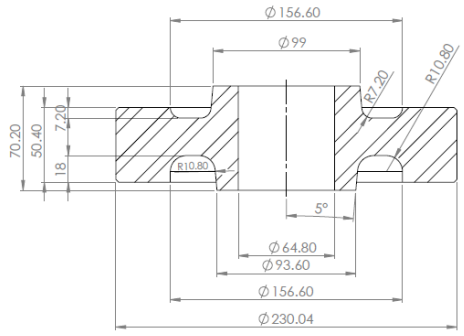

***Figure 1.** Final part drawing*

The forged part design is developed by using the part drawing and following the guidelines found in the EN DIN 10243-1 standard. This standard covers hot forgings made from carbon and alloy steels with a mass up to 250 kg.

2.1. Category of steel used

The type of steel used takes account of the fact that steels of high carbon and high alloy content are more difficult to deform and cause higher die wear than steels with lower carbon content and lower alloying elements. The category of steel used is determined as being one of the following:

- Group M1: Steel with carbon content not greater than 0.65% and total of specified alloying elements (Mn, Ni, Cr, Mo, V, W) not greater than 5% by mass;
- Group M2: Steel with carbon content above 0.65% or total specified alloying elements (as mentioned above) above 5% by mas;

To determine the category in which a steel belongs, the maximum permitted content of the elements in the steel specification will be used.

Table 1. Chemical composition

C	Si	Mn	Ni	V	Cr	Mo
0.42 - 0.50	max 0.37	0.5 – 0.8	1.3 – 1.8	0.10 – 0.18	0.3 - 0.6	0.2 - 0.3

The steel 45Х2МФА: ГОСТ 4543 has carbon mass fraction of up to 0.50% and a total mass fraction of its alloying elements of 4.18%. This places the steel in the group M1.

2.2. Shape complexity factor

The shape complexity factor takes account of the fact that in forging thin sections and branched components, as compared to components having simple compact shapes, larger dimensional variations occur which are attributable to different rates of shrinkage, higher shaping forces and higher rates of die wear. The shape complexity factor of a forging is the ratio of the mass of the forging to the mass of the enveloping shape necessary to accommodate the maximum dimensions of the forging.

$$S = \frac{m_{forging}}{m_{enveloping\ \ shape}} = \frac{\rho \cdot V_{forging}}{\rho \cdot V_{enveloping\ \ shape}},$$

where: S – complexity factor, $m_{forging}$ – mass of forged part, $m_{enveloping\ shape}$ – mass of enveloping shape, ρ – material density, V – volume.

The resulting shape complexity factor is determined as falling within one of the following categories:

- S4: up to and including 0.16;
- S3: above 0.16 up to and including 0.32;
- S2: above 0.32 up to and including 0.632;
- S1: above 0.63 up to and including 1;

$$V_{forging} = V_{part} \cdot K_P$$

$$m_{forging} = m_{part} \cdot K_P$$

where, K_p = 1.5 ÷ 1.8 – shape coefficient for round forged parts (gears, flanges, discs, etc.).

The parts mass and volume can be determined by using any CAD software while using the density of the material in question (Figure 2).

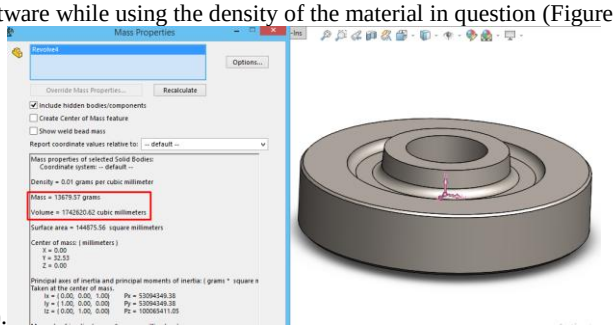

Figure 2. *Mass properties for the final part – SolidWorks*

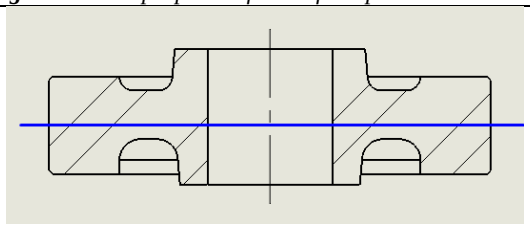

Figure 3. *Parting line*

$$V_{forging} = V_{part} \cdot K_P = 1742620.62 \cdot 1.5 = 2613930.93\ mm^3$$

$$m_{forging} = m_{part} \cdot K_P = 13679.57 \cdot 1.5 = 20519.355\ kg$$

The enveloping shape of a circular forging is the circumscribing cylinder the volume of which is calculated by increasing the maximal width and height of the final part by 5% to accommodate the increased size of the forging.

$$V_{enveloping\ \ shape} = \frac{(D_{max} \cdot 1{,}05)^2 \cdot \pi}{4} \cdot (H_{max} \cdot 1{,}05)$$

where, D_{max} [mm] – largest diameter; H_{max} [max] – largest part height.

$$V_{enveloping\ \ shape} = \frac{(230.04 \cdot 1{,}05)^2 \cdot \pi}{4} \cdot (70.2 \cdot 1{,}05) = 3375836.34\ mm^3$$

$$S = \frac{\rho \cdot V_{forging}}{\rho \cdot V_{enveloping\ \ shape}} = \frac{2613930.93}{3375836.34} = 0.7743$$

The complexity factor S = 0.7743 falls in the S1 category. It is important to emphasize that the initial complexity factor is an estimated value due to the estimation of the forgings and enveloping shapes mass. The estimated degree of complexity should be refined after calculating the exact envelopes and forging mass.

2.3. Parting line configuration

The part has a plain parting line configuration located at the half point of the thickness at the largest diameter (as shown in Figure 3).

2.4. Forging equipment selection

In order to begin the forging design, we must first select a forging machine by doing a control calculation to determine the plausibility of the technological process on the available equipment by estimating the needed machine force.

- For power-drop steam hammers:

$$G = 10(1 - 0{,}005D_{fmax})(1{,}1 + \frac{2}{D_{fmax}})^2(0{,}75 + 0{,}001{D_{fmax}}^2)D_{fmax} \cdot \sigma_m$$

- For mechanical presses:

$$F = 8(1 - 0{,}001D_{fmax})(1{,}1 + \frac{20}{D_{fmax}})^2 A \cdot \sigma_m$$

where, G [kg] – hammers falling mass; F [kg] – mechanical press force needed for forging circular forgings; $D_{fmax} = D_{max} \cdot 1{,}05$ – largest forging diameter; $\sigma_m \left[\frac{kg}{mm^2}\right]$ – material strength in the final forging stages; $A = \frac{{D_{fmax}}^2 \cdot \pi}{4}\ [mm^2]$ – projection of the forging in the horizontal plane.

The steel 45Х2МФА: ГОСТ 4543 can be classified in the second type according to table 2. From there we select the values for σ_m for the forging hammers and mechanical presses for the calculations.

Table 2. *Steel strength σ_m [kg/mm^2] in the final forging stages*

	Type of steel	Forging hammers	Mechanical presses	Horizontal forging machines
1.	Carbon steel with carbon content up to 0,25 %	5,5	6	7
2.	Carbon steel with carbon content above 0,25 %, or Alloyed steel with carbon content up to 0,25 % and alloying element content up to 5%	6	6,5	8
3.	Alloyed steel with carbon content above 0,25 % and alloying element content up to 5%	6,5	7	9
4.	Alloyed steel with alloying element content above 5%	7,5	8	10
5.	Alloy tool steel	9 - 10	10 - 12	12 - 14

$$G = 10(1 - 0{,}005D_{fmax})(1{,}1 + \frac{2}{D_{fmax}})^2(0{,}75 + 0{,}001{D_{fmax}}^2)D_{fmax} \cdot \sigma_m = 2.4\ t$$

$$F = 8(1 - 0{,}001D_{fmax})(1{,}1 + \frac{20}{D_{fmax}})^2 A \cdot \sigma_m = 13800\ t = 138\ MN$$

Since the estimated value for the needed force on the power-drop hammer is reasonable, it is selected as the forging machine used to manufacture the forging of the part. All the tolerances and machining allowances will be selected to suit the forging process on steam hammers.

2.5. Defining the forged part dimensions

All of the tolerances and machining allowances for the forged part were selected from the tables 1 to 6 from the standard DIN EN 10243-1. The standard identifies two grades of tolerances. Forging grade F with tolerances providing adequate standard of accuracy for the majority of applications and capable of being complied with by commonly used forging equipment and production methods. Forging grade E providing closer tolerances to assist in accommodating those instances in which the normal manufacturing standards are inadequate. The forging grades "E" and "F" were allocated to the measures, depending on the particular surface roughness and tolerances designated in the part drawing. The standard also identifies four major types of dimensions and several minor ones and classifies them in 4 groups.

All of the allocated allowances and tolerance grades for the inner and outer forging dimensions are given in table 4. Finally, the resultant dimensions are modified by a factor η that takes into

account the thermal expansion while heating. The outer dimensions are increased and the inner ones are decreased by a specific amount that corresponds to the forging temperature. This way we ger the correct hot forging part design with measurements ready for creating the die geometry. $\eta = 1{,}025$ – thermal expansion coefficient for steel alloys at forging temperatures of ~1200 °C.

2.6. Forging draft angles

Draft is an angle allowance added to surfaces parallel to the direction of die closure to facilitate release of the part form the die after forging. In general, draft allowances on inside surfaces are greater than those on outside surfaces, because of the tendency of the part to shrink onto projections in the die as cooling takes place [2]. For power drop steam hammers the chosen normative draft angles are as follows: $\alpha = 7°$ - external draft angle; $\alpha_1 = 10°$ - internal draft angle.

2.7. Forging fillet radii

All edges and corners in the part must have added fillets. These fillets are necessary to aid material flow and ensure good die filling. In addition, sharp corners in dies can lead to premature die failure due to fracture as a result of associated high stress concentrations. In general, larger radii are recommended for the more difficult-to-forge materials [2]. The outer radii are selected depending on the mass of the forging and the largest depth of the die impression that is calculated according to the position of the parting line; $R_{outer} = 2.5\ mm$.

The inner radii are calculated using this formula:

$$r_{inner} = (2{,}5 \div 3{,}5)R_{outer} + 0{,}5$$

$$r_{inner} = 3 \cdot 2.5 + 0.5 = 8\ mm$$

2.8. Defining the position, shape and dimensions of the barrier plates for all through holes in the forged part

In the forging process, holes are not punched through because this would make the ejection of the part more difficult. This way the dies are separated by a barrier plate in each hole. The thickness of the plate is calculated using the following equation:

$$s = 0{,}45\sqrt{d - 0{,}25h - 5} + 0{,}6\sqrt{h}$$

where, s [mm] – plate thickness, d [mm] – diameter of the hole at the topmost surface, h [mm] – distance from the plate midline to the topmost surface of the forging.

$$s = 0{,}45\sqrt{d - 0.25h - 5} + 0.6\sqrt{h} = 6.87 \rightarrow 7\ mm$$

The fillet radii for the plate also have to be calculated. Hence, we use the equation: $r_1 = r_{inner} + 0{,}1h + 2$, where, r_1 [mm] – fillet radii for the plate edges, r_{inner} [mm] – inner fillet radii for the forged part.

$$r_1 = r_{inner} + 0.1h + 2 = 14.37 \rightarrow 14\ mm$$

The type of plate depends on the size of the forging part, the diameter and the height of the hole. To determine the type, we need to check the following condition:

$$d - 1.25r_1 = 57.72 - 1.25 \cdot 14 = 39.75$$

The condition $d - 1{,}25r_1 > 26$ requires the use of a Type II plate with a shape shown in Figure 288, page 581, Obrada Metala Plasticnom Deformacijom, Binko Musafija.

$$d_1 = 0.12 \cdot s + 3 = 3.82 \rightarrow 4\ mm$$

$$S_{min} = 0.65 \cdot s = 4.4 \rightarrow 4\ mm$$

$$S_{max} = 1.35 \cdot s = 9.2 \rightarrow 8\ mm$$

where, d_1 [mm] – flat length of the plate, S_{min} [mm] – minimal plate thickness, S_{max} [mm] – maximal plate thickness.

2.9. Control check for the forging mass and the complexity factor S

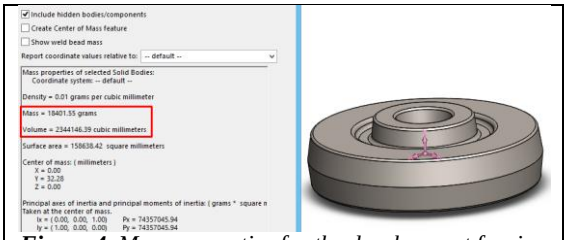

Figure 4. *Mass properties for the development forging part – SolidWorks*

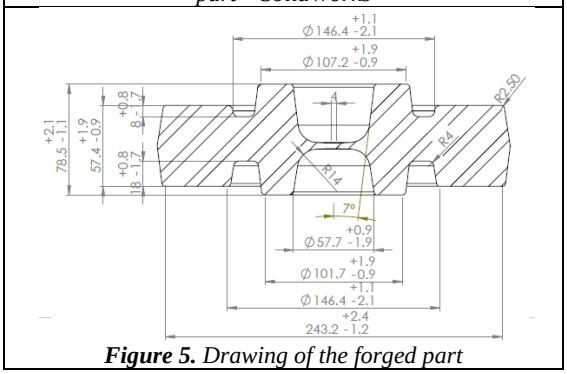

Figure 5. *Drawing of the forged part*

$$V_{enveloping\ \ shape} = \frac{D_{max}{}^2 \cdot \pi}{4} \cdot H_{max} = \frac{243.17^2 \cdot \pi}{4} \cdot 78.5 = 3644566.28\ mm^3$$

where, D_{max} [mm] – largest part diameter (with the added machining allowances), H_{max} [mm] largest part height (with the added machining allowances).

$$S = \frac{m_{forging}}{m_{enveloping\ \ shape}} = \frac{\rho \cdot V_{forging}}{\rho \cdot V_{enveloping\ \ shape}} = \frac{2344146.39}{3644566.28} = 0.64$$

The complexity factor S = 0.64 falls in the S1 category, same as the initially calculated value. Since the mass is within the previously selected range and the refined complexity factor matches the initial calculation, the added allowances are considered correct.

2.10. Determining the flash land geometry

The flash produced during closed-die forging is scrap material and may in many cases have a volume that is more than 50% of the final part volume. The amount of flash produced increases with the complexity of the part. However, the production of the flash is a necessary part of the process, and its control is essential to ensure good die filling [2]. The choice of the appropriate width and thickness of the flash land is an important part of the forging design. If the geometry is wrong, the dies may not fill completely or the forging loads may become excessive. In addition, the projected area of the flash in the flash land is usually included in the total projected area of the part for estimation of the forging loads required and therefore is a determining factor in equipment selection for processing. In order for vertical flow to occur in the die, the resistance to flow in the flash gap must be higher than that

required for vertical flow in the die. The material must not flow into the flash gap until the die cavity is completely filled. The resistance to flow in the flash gap depends upon the ratio of flash land width to flash land height. The flash land height can be calculated approximately using the following expression [3]: $c = 0{,}015\sqrt{A}$

where, c [mm] – flash land height, A [mm^2] – projected area of the forging (including allowances and draft).

$$c = 0{,}015\sqrt{46775.67} = 3.244\ mm$$

The flash land width is calculated with the help of a coefficient that takes into account the way the die is filled during the forging process: $K = 1{,}5 + 0{,}3\frac{H}{B_{avg}}$

where, K – coefficient that takes into account the way the die is filled, H [mm] – largest die depth, B_{avg} [mm] – average width of the die at the location of the flash land.

$$K = 1.5 + 0.3\frac{42.8}{237.24} = 1.55$$

According to the calculated values for the bridge height *c* and the coefficient *K* we choose the nearest standard flash land size. All relevant dimensions are given in table 3 below and figure 293, page 596 in Obrada Metala Plasticnom Deformacijom, Binko Musafija [4].

Table 3. Standard flash land and gutter dimensions

$c\ [mm]$	$c_1\ [mm]$	$R\ [mm]$	$b\ [mm]$	$b_1\ [mm]$	$A_f\ [mm^2]$	$R_1\ [mm]$	$R_2\ [mm]$
4	6	2	11	30	268	6	2

Finally, we need to determine the flash volume in order to be able to calculate the dimensions of the initial workpiece. The flash volume is calculated by the following expression: $V_f = \xi \cdot A_f \cdot P$, where, V_f [mm^3] – flash volume, ξ = 0.5 – coefficient of gutter fullness for axisymmetric forged parts, A_f [mm^2] – flash gap cross section area, $P = D_{max} \cdot \pi$ [mm] – perimeter of the forging in the parting plane (parting line length).

$$V_v = \xi \cdot A_f \cdot P = 0{,}5 \cdot 268 \cdot 237.24 \cdot \pi = 99821.1\ mm^3$$

2.11. Determining the initial workpiece dimensions

The volume of the workpiece is the sum of the forging and the flash volume, while taking into account the scale losses that occur during heat treatment processes. Oxide scales discolour the metal surface and hinder subsequent finishing operations and therefore need to be removed from the heated stock, either before or during forging operations.

$$V_{wp} = (V_{FP} + V_f)(1 + \Delta)$$

where, V_{wp} [mm^3] – workpiece volume, V_{FP} [mm^3] – forging volume, V_f [mm^3] – flash volume, Δ - scale loss.

Due to the fact that scale loss cannot be included in the simulation, for the purpose of this report, the scale loss coefficient is not taken into account (Δ = 0).

$$V_{wp} = (V_{FP} + V_f)(1 + \Delta) = 4252707.32 + 99821.1$$
$$= 4352528.42\ [mm^3]$$

Round parts are forged from cylindrical billets and before the dimensions are calculated we need to determine the relation between the height and the diameter of the workpiece.

$m = \frac{h_{wp}}{d_{wp}}$, where, $m = 1{,}5 \div 2{,}8 - {}^{h}/_{d}$ ratio, d_p [mm] – workpiece diameter, h_p [mm] – workpiece diameter.

This relation is in the range $m = 1{,}5 \div 2{,}8$. If m < 1.5 then the shearing of the billet to size is more difficult and is accompanied by the forming of big burr formations. For ratios of m > 2.8 there is a risk of buckling. The billet dimensions are determined by the volume and the ratio m. The estimated diameter is calculated as follows: $d_{wp} = 1.08\sqrt[3]{\frac{V_{wp}}{m}} = 154.04mm$

The standard dimensions for cylindrical billets are found in Kraut's Mechanical Engineering Handbook: $d_{wp} = 155\ mm$

The billets height is calculated using the expression:

$$h_p = \frac{V_{wp}}{A_{wp}} = \frac{4 \cdot V_{wp}}{\pi \cdot d_{wp}^{\ 2}} \approx \mathbf{145}\ mm$$

The billet for the part forging has the following dimensions:

$$\emptyset\ \mathbf{155} \times \mathbf{145}$$

2.12. Determining the die block dimensions

The dimensions selected for the die blocks depend on the depth of the cavity. The minimal thickness and height for each block (table 4) were selected according to the recommendations in Metal Forming Practise Processes, page 135, table 13.11 [3].

Table 4. Selected die block dimensions

	h [mm]	a [mm]	H [mm]
Upper block	43.76	56	200
Lower block	34.76	40	160

2.13. Production phases

1. Shearing the initial workpiece with a diameter of $\emptyset\mathbf{155}$ and height of $\mathbf{145\ mm}$.
2. Heating up the workpiece to the forging temperature of $\approx \mathbf{1100\ °C}$.
3. Upsetting the workpiece to a height of $\boldsymbol{h_1 = 83\ mm}$. The upsetting is carried out on a power-drop steam hammer (5t).
4. Finishing forging done on a power-drop steam hammer to the shape and dimensions given in Figure 5.
5. Flash removal using a trimming die and punching the barrier plate for the hole.

3. Simulation of the forging process

Computer Aided Engineering has many benefits when it comes to saving time and expenses, it gives certain important information about the forging process before the part is approved for production. Information as material flow, stress, deformation, temperature etc. are available to the user at any given moment after the simulation is done. This way potential defects as material overlapping, excess or lack of material etc. After all the calculations are finished, the 3D model and the 2D sketches in the CAD software, everything is set for the simulation to begin.

The numerical analysis for this study is simulated in two operations, upsetting and closed die forging with flash, as well as an additional operation for removing the flash and plate.

The first operation as said is upsetting. It is done with a 5t forging hammer. The initial part is heated to 1100 °C for the recrystallization process to occur. In this phase the initial height of

the part 145 mm is reduced to 83 mm. This allows the following operation to be completed with ease. The reducing of the height is completed with hammer blows. Figure 6. shows the maximum and minimum effective stress of the part in the first blow of the upsetting stage. The maximum stress is 170.83 MPa. Figure 7. shows the maximum and minimum effective stress of the part in the second blow of the upsetting stage. The maximum stress is 216.18 MPa.

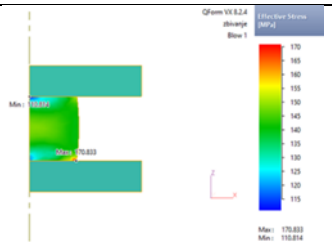

Figure 6. *Effective stress during the first blow*

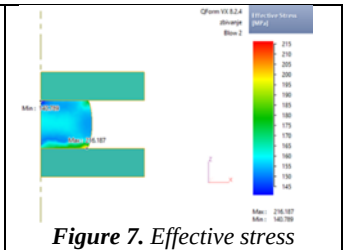

Figure 7. *Effective stress during the second blow*

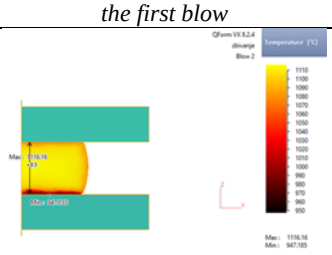

Figure 8. *Part temperature after the upsetting phase*

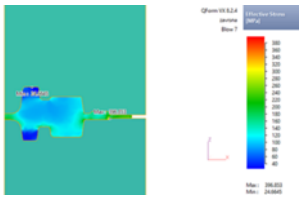

Figure 9. *Unsuccessful closed die forging simulation*

Figure 8. shows the temperature of the part after the upsetting. It is clear that the inside of the part will have its temperature (1116.16 °C) increased due to the deformations.

The second operation, closed die forging with flash, is completed with 5 hammer blows. The part is still heated, and graphite + water is used as a lubricant. In this operation the part gets its final geometry, and this is the phase where the most defects happen. During the simulation, there were a few unsuccessful attempts due to excess material, as it is shown is figure 9.

Figure 10, 11, 12 and 13 show the four needed blows for the operation. The figures show that the cavity fills in the first, second and third blow, and the fourth blow is for filling the flash.

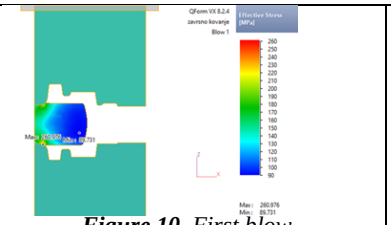

Figure 10. *First blow*

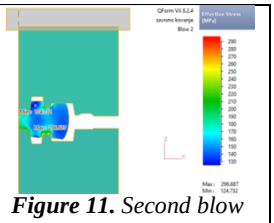

Figure 11. *Second blow*

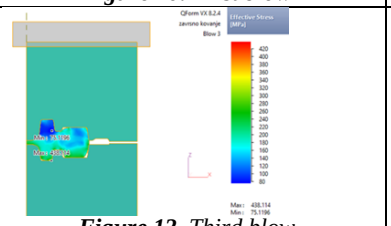

Figure 12. *Third blow*

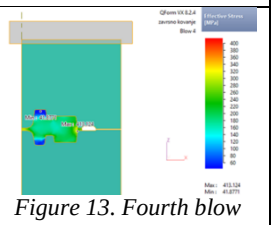

Figure 13. Fourth blow

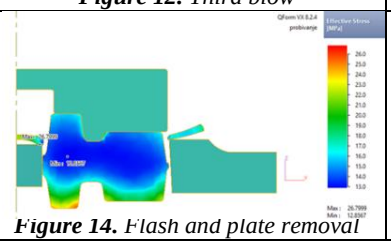

Figure 14. *Flash and plate removal*

The additional operation, removal of flash and plate, is completed on a mechanical press (6.3 MN). The goal of this operation is to remove the excess material which was necessary during the forging process. This operation is done with one blow, simultaneously removing the flash and plate (Figure 14).

4. Conclusion

Forging simulation offers significant advantages by providing detailed insight into the forging process before tool selection and process decisions are made on the shop floor [5]. Thanks to the numerical simulations, the initial error in the study is avoided, and the simulation was successful. Because of the complexity of metal flow, the friction between the tool and part, the temperature generation, CAE software is needed to analyse the initial idea of how the process should look like. In the process of making a product, it is very important in getting to know the characteristics of certain structures and their behaviour in exploitation.

5. References

1. T. Altan, G. Ngaile, G. Shen, *Cold and Hot Forging – Fundamentals and Applications* (2005)
2. G. Boothroyd, P. Dewhurst, W. A. Knight, *Product Design for Manufacture and Assembly* (2010)
3. H. Tschätsch, *Metal Forming Practice Processes* (2006)
4. B. Musafija, *Obrada Metala Plasticnom Deformacijom* (1979)
5. S. Khalilpourazary, T. Azdast, *Design and manufacturing of a straight bevel gear in hot precision forging process using finite volume method and CAD/CAE technology* (2011)

Buckling analysis of columns made of functionally graded materials via Rayleigh-Ritz method

Domagoj Lanc[1,*], Ivana Ivančić[2], Mihael Katalenić[2]
Faculty of Engineering, University of Rijeka, Croatia [1]
dlanc@riteh.hr

Abstract: *This paper presents the buckling analysis of functionally graded (FG) beams. To solve differential buckling equations of different FG sections the Rayleigh-Ritz method is used. The FG material is supposed to vary continuously over the beam depth according to power low. A set of analytical evaluation is run in order to calculate critical buckling loads in dependents of material power low index. The accuracy of method is confirmed comparing the results with the finite element ones.*
Keywords*: FUNCTIONALLY GRADED MATERIALS, RAYLEIGH-RITZ METHOD, BUCKLING, CRITICAL LOAD*

1. Introduction

This paper presents the flexural in plane buckling analysis of functionally graded (FG) beams using the Reyleig-Ritz method. A development of a new kinds of progressive composites such as functionally graded materials (FGM) in recent years is in a rapid increase. FGMs were first conceptualized at 1980s and after that have been very extensively studied by several researchers. Functionally graded materials are a type of composite materials that have a continuous material property change from one surface to another. Contrary to laminated composites, in such a way, the stress concentration is eliminated. FG material is usually made of a mixture of ceramics and metals. The ceramic can resist high temperature in thermal environments, whereas the metal can decrease the tensile stress occurring on the ceramic surface at the earlier state of cooling [1].

The beam structures are extensively used in engineering practice, both in stand-alone forms or as the stiffeners for plate-like or shell-like structures. Due to their slenderness, such structures are generally very susceptive to buckling.

Critical buckling load can be determinate solving the differential equilibrium equations using the approximate methods, based on the energy principal. The one of such methods is well known Rayleigh-Ritz method. The linearized stability analysis is performed in an eigenvalue manner and it attempts to determine the instability load in a direct manner without calculating the deformations. The lowest eigenvalue is recognized as a critical ones and the corresponding eigenvector corresponded to critical buckling mode. There are so many papers dealing with the buckling or vibration of FG beams, only some of that papers are cited here [2-5].

2. Rayleigh-Ritz method

The Rayleigh-Ritz method is based on existence of a relative minimum of the total potential energy at neutral equilibrium.

$$\delta\Pi = \delta(\mathsf{U} - \mathsf{V}) = 0 \tag{1}$$

where the U and V are potentials of internal and external forces.

For the case of in-plane flexural buckling of axially loaded simply supported beam, (see Fig. 1) the internal potential energy can be expressed as:

$$\mathsf{U} = \frac{1}{2}\int_0^l E I_x(z)\left(\frac{\mathrm{d}^2 v}{\mathrm{d}z^2}\right)^2 \mathrm{d}z \tag{2}$$

while the potential of external forces can be written as:

$$\mathsf{V} = -F_{cr} w_B = -\frac{F_{cr}}{2}\int_0^l \left(\frac{\mathrm{d}v}{\mathrm{d}z}\right)^2 \mathrm{d}z \tag{3}$$

The total potential is:

$$\Pi = \frac{1}{2}\int_0^l \left[E(z) I_x \left(\frac{\mathrm{d}^2 v}{\mathrm{d}z^2}\right)^2 - F_{cr}\left(\frac{\mathrm{d}v}{\mathrm{d}z}\right)^2 \right] \mathrm{d}z \tag{4}$$

According to Rayleigh-Ritz method, the beam deflection can be approximate as:

$$v_a(z) = \sum_i c_i \cdot \phi_i(z), \qquad i = 1,2,3,... \tag{5}$$

where the $\phi_i(z)$ are some known function satisfying the boundary condition while the c_i are unknown constants that should be determinate from condition defined by in equation 1.

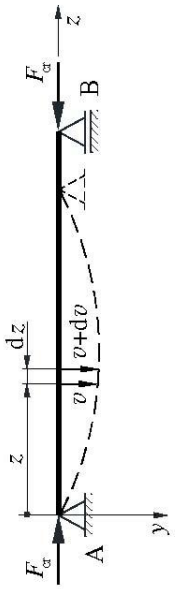

Fig. 1 *Buckling of axially loaded simply supported beam*

3. Functionally graded material

Supposing the functionally graded material, (see Fig. 2), the elasticity modulus is varied continuously through the beam height direction according to power-law distribution [6]:

$$E(y) = \left(E_{top} - E_{bot}\right)\cdot V_c + E_{bot} \tag{6}$$

where subscripts *top* and *bot* indicate the top and bottom surface components, and V_c represent the volume fraction of the ceramic phase, respectively.

The volume fraction can be calculated according to following formula:

$$V_c = \left(\frac{1}{2} + \frac{y}{h}\right)^p \tag{7}$$

where p is the power-law index.

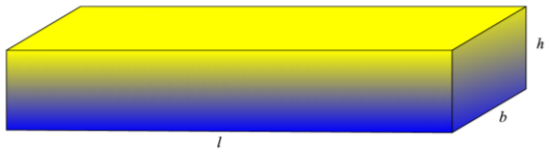

Fig. 2 *Material distribution over FG beam*

It should be noted that for zero value of power-law index, the FG material is the full ceramic, while as the power-law index increases, the FG material tends towards the full metal. An illustrative example of variation of E modulus in beam height direction for different values of power-law index p is shoved on Fig. 3.

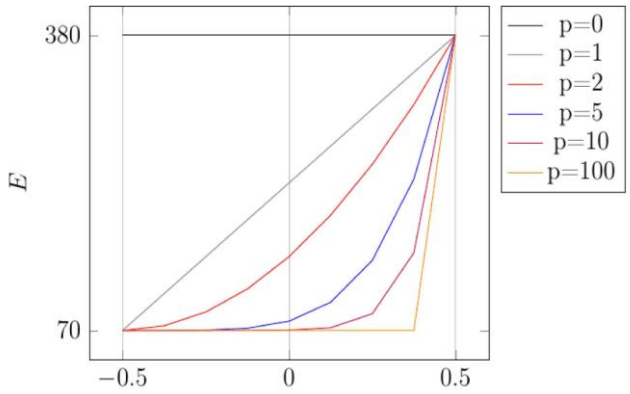

Fig. 3 *Variation of E-modulus over the beam height*

As it was described in the previous paragraph, the material parameters are not constant, so the flexural rigidity for the beam of constant weight can be calculated as:

$$EI_x = \int_{-h/2}^{h/2} b\left(\left(E_{top} - E_{bot}\right)\cdot\left(\frac{1}{2}+\frac{y}{h}\right)^p + E_{bot}\right)y^2\,dy \qquad (8)$$

3. Examples

As the first example, the axially loaded simply supported beam is considered. The beam length is l = 8 m while the cross section dimensions are $b = h$ = 0.1 m. FG material properties are assumed to be [7, 8]: Aluminum (Al: $E_m = E_{in}$ = 70 GPa, ν_m = 0.3) and Alumina (Al_2O_3: $E_c = E_{out}$ = 380 GPa, ν_c = 0.3).

The three parameter approximation is adopted, so selected $\phi_1(z)$ functions are:

$$\begin{aligned}\phi_1(z) &= \sin\left(\frac{\pi z}{l}\right);\\ \phi_2(z) &= \sin\left(\frac{3\pi z}{l}\right);\\ \phi_3(z) &= \sin\left(\frac{3\pi z}{l}\right)\end{aligned} \qquad (9)$$

The total potential according to equations (4) and (5) now can be expressed as:

$$\begin{aligned}\Pi = \frac{1}{2}\int_0^l\left[E(z)I_x\left(c_1\frac{d^2\phi_1}{dz^2}+c_2\frac{d^2\phi_1}{dz^2}+c_3\frac{d^2\phi_1}{dz^2}\right)^2\right]dz -\\ -\frac{1}{2}\int_0^l\left[-F_{cr}\left(c_1\frac{d\phi_1}{z}+c_2\frac{d\phi_1}{dz}+c_3\frac{d\phi_1}{dz}\right)^2\right]dz\end{aligned} \qquad (10)$$

where c_1, c_2, c_3 are unknown constant that follows from the non-triviality condition:

$$\frac{\partial\Pi}{\partial c_1}=0;\quad \frac{\partial\Pi}{\partial c_2}=0;\quad \frac{\partial\Pi}{\partial c_3}=0 \qquad (10)$$

or

$$\begin{aligned}\frac{\partial\Pi}{\partial c_1} = c_1\int_0^l E(z)I_x\left(\frac{d^2\phi_1}{dz^2}\right)^2 dz + c_2\int_0^l E(z)I_x\left(\frac{d^2\phi_1}{dz^2}\frac{d^2\phi_2}{dz^2}\right)dz +\\ +c_3\int_0^l E(z)I_x\left(\frac{d^2\phi_1}{dz^2}\frac{d^2\phi_3}{dz^2}\right)dz - F_{cr}c_1\int_0^l\left(\frac{d\phi_1}{z}\right)^2 dz -\\ -F_{cr}c_2\int_0^l\left(\frac{d\phi_1}{z}\frac{d\phi_2}{z}\right)dz - F_{cr}c_3\int_0^l\left(\frac{d\phi_1}{z}\frac{d\phi_3}{z}\right)dz\end{aligned} \qquad (11a)$$

$$\begin{aligned}\frac{\partial\Pi}{\partial c_2} = c_1\int_0^l E(z)I_x\left(\frac{d^2\phi_1}{dz^2}\frac{d^2\phi_2}{dz^2}\right)dz + c_2\int_0^l E(z)I_x\left(\frac{d^2\phi_2}{dz^2}\right)^2 dz +\\ +c_3\int_0^l E(z)I_x\left(\frac{d^2\phi_1}{dz^2}\frac{d^2\phi_3}{dz^2}\right)dz - F_{cr}c_1\int_0^l\left(\frac{d^2\phi_1}{dz^2}\frac{d^2\phi_2}{dz^2}\right)dz -\\ -F_{cr}c_2\int_0^l\left(\frac{d\phi_2}{z}\right)^2 dz - F_{cr}c_3\int_0^l\left(\frac{d\phi_1}{z}\frac{d\phi_3}{z}\right)dz\end{aligned} \qquad (11b)$$

$$\begin{aligned}\frac{\partial\Pi}{\partial c_1} = c_1\int_0^l E(z)I_x\left(\frac{d^2\phi_1}{dz^2}\frac{d^2\phi_3}{dz^2}\right)dz + c_2\int_0^l E(z)I_x\left(\frac{d^2\phi_2}{dz^2}\frac{d^2\phi_3}{dz^2}\right)dz +\\ +c_3\int_0^l E(z)I_x\left(\frac{d^2\phi_3}{dz^2}\right)^2 dz - F_{cr}c_1\int_0^l\left(\frac{d\phi_1}{z}\frac{d\phi_3}{z}\right)dz -\\ -F_{cr}c_2\int_0^l\left(\frac{d\phi_2}{z}\frac{d\phi_3}{z}\right)dz - F_{cr}c_3\int_0^l\left(\frac{d\phi_3}{z}\right)^2 dz\end{aligned} \qquad (11c)$$

It can be also written in a matrix form:

$$\left(\begin{bmatrix}A_{11} & A_{12} & A_{13}\\ A_{21} & A_{22} & A_{23}\\ A_{31} & A_{32} & A_{33}\end{bmatrix} - F_{cr}\begin{bmatrix}B_{11} & B_{12} & B_{13}\\ B_{21} & B_{22} & B_{23}\\ B_{31} & B_{32} & B_{33}\end{bmatrix}\right)\begin{Bmatrix}c_1\\ c_2\\ c_3\end{Bmatrix} = \begin{Bmatrix}0\\ 0\\ 0\end{Bmatrix} \qquad (12)$$

The coefficients in equation (12) are prescribed by the following integrals:

$$A_{11} = \int_0^l E(z)I_x\left(\frac{d^2\phi_1}{z^2}\right)^2 dz \qquad (13a)$$

$$A_{12} = A_{21} = \int_0^l E(z)I_x\left(\frac{d^2\phi_1}{z^2}\frac{d^2\phi_2}{z^2}\right)dz \qquad (13b)$$

$$A_{13} = A_{31} = \int_0^l E(z)I_x\left(\frac{d^2\phi_1}{z^2}\frac{d^2\phi_3}{z^2}\right)dz \qquad (13c)$$

$$A_{22} = \int_0^l E(z)I_x\left(\frac{d^2\phi_2}{z^2}\right)^2 dz \qquad (13d)$$

$$A_{23} = A_{32} = \int_0^l E(z)I_x\left(\frac{d^2\phi_2}{z^2}\frac{d^2\phi_3}{z^2}\right)dz \qquad (13e)$$

$$A_{33} = \int_0^l E(z)I_x\left(\frac{d^2\phi_3}{z^2}\right)^2 dz \qquad (13f)$$

$$B_{11} = \int_0^l\left(\frac{d\phi_1}{z}\right)^2 dz \qquad (13g)$$

$$B_{12} = B_{21} = \int_0^l\left(\frac{d\phi_1}{z}\frac{d\phi_2}{z}\right)dz \qquad (13h)$$

$$B_{13} = B_{31} = \int_0^l\left(\frac{d\phi_1}{z}\frac{d\phi_3}{z}\right)dz \qquad (13i)$$

$$B_{22} = \int_0^l\left(\frac{d\phi_2}{z}\right)^2 dz \qquad (13j)$$

$$B_{23} = B_{32} = \int_0^l\left(\frac{d\phi_2}{z}\frac{d\phi_3}{z}\right)dz \qquad (13k)$$

$$B_{33} = \int_0^l \left(\frac{d\phi_3}{z} \right)^2 \mathrm{d}z \tag{13l}$$

Solving for determinant of (12) follows the solutions for critical buckling load:

$$Det \begin{bmatrix} A_{11} - B_{11}F_{cr} & A_{12} - B_{12}F_{cr} & A_{13} - B_{13}F_{cr} \\ A_{21} - B_{12}F_{cr} & A_{22} - B_{22}F_{cr} & A_{23} - B_{23}F_{cr} \\ A_{31} - B_{31}F_{cr} & A_{32} - B_{32}F_{cr} & A_{33} - B_{33}F_{cr} \end{bmatrix} = 0 \tag{14}$$

The results for critical loadings that corresponds to different values of power-low index are given in the Table 1.

For results validation purposes, the closed form solution formula $F_{cr} = \pi^2 EI_x / l^2$, well known from the strength of materials gives the solutions for the pure metal $F_{\mathrm{cr,metal}}$ = 488339.8 N as well as for the pure ceramics $F_{\mathrm{cr,ceramic}}$ = 89957.3 N. This values well corresponds to the cases of power-law exponent values p = 0 and p = 1000.

Table 1: *Critical buckling loads versus power-law index for the case of simply supported beam*

p	F_{cr} [N]
0	488340
1	289149
2	222752
5	156354
10	126174
100	93902
200	91939
500	90753
1000	90355

In the second example, for the same beam geometry and material properties, different boundary conditions are considered. One side of the beam is simply supported while the other side is clamped (see Fig. 4.)

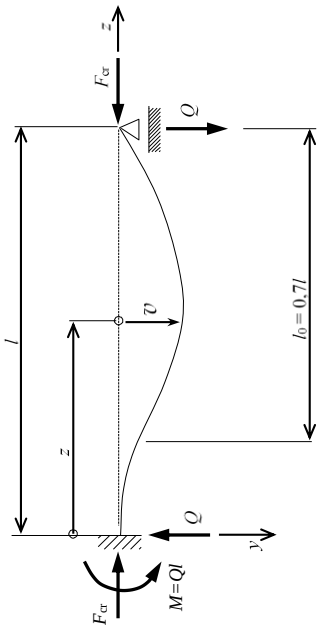

Fig. 4 *Buckling of axially loaded simply supported-clamped beam*

In this case the total potential is:

$$\Pi = \frac{1}{2} \int_0^l \left[E(z) I_x \left(\frac{\mathrm{d}^2 v}{\mathrm{d}z^2} \right)^2 - F_{\mathrm{cr}} \left(\frac{\mathrm{d}v}{\mathrm{d}z} \right)^2 - (Q(l-z))^2 \right] \mathrm{d}z \tag{15}$$

Using the five parameter polynomial approximation for deflection, as:

$$v_a(z) = c_1 \cdot \phi_1(z) + c_2 \cdot \phi_2(z) + c_3 \cdot \phi_3(z) + c_4 \cdot \phi_4(z) + c_5 \cdot \phi_5(z) \tag{16}$$

where the approximate functions are:

$$\begin{aligned} \phi_1(z) &= z^2(l-z); \\ \phi_2(z) &= z^3(l-z); \\ \phi_3(z) &= z^4(l-z); \\ \phi_4(z) &= z^4(l-z); \\ \phi_5(z) &= z^5(l-z) \end{aligned} \tag{17}$$

Again, the non-triviality condition should be satisfied in order to form buckling equation:

$$\frac{\partial \Pi}{\partial c_1} = 0; \quad \frac{\partial \Pi}{\partial c_2} = 0; \quad \frac{\partial \Pi}{\partial c_3} = 0; \quad \frac{\partial \Pi}{\partial c_4} = 0; \quad \frac{\partial \Pi}{\partial c_5} = 0 \tag{18}$$

where c_1, c_2, c_3, c_4, c_5 are unknown constants.

Following the same procedure as it was described in the previous section, the solutions for critical buckling load can be obtained. These solutions are presented in Table 2, for different values of power law exponent.

For comparison, critical buckling loads for pure materials evaluated via closed form solution formula $F_{cr} = \pi^2 EI_x / (0.7l)^2$ are: $F_{\mathrm{cr,metal}}$ = 183586.4 N and $F_{\mathrm{cr,ceramic}}$ = 996611.8 N. This values are comparable with the results for power-law exponent values p = 0 and p = 1000.

Table 2: *Critical buckling loads versus power-law index for the case of simply supported -clamped beam*

p	F_{cr} [N]
0	999031
1	591531
2	455698
5	319865
10	258122
100	192101
200	188086
500	185658
1000	184846

5. Conclusion

In this research, the analytical model for buckling analysis of functionally graded beams is applied. The model is developed on the basis of Rayleigh-Ritz method. This model is capable of predict accurately the critical buckling loading of axially loaded columns with different types of boundaries. The set of analytical evaluations is run in order to find the spectrum of results for different exponential material distribution. Results are presented with the respect to power law exponent values. The results are validated by comparison to closed form formula results for the cases of pure metal and pure ceramic cases. Very good correlation was observed. The proposed method is found to be appropriate and efficient in analysing buckling problem of functionally graded beams. The same method can also be successfully adapted to beam cross sections structured as sandwich with the pure metal or ceramic skins with the functionally graded core as well as to sandwiches with FG skins and pure metal or pure ceramic core.

6. Acknowledgement

The authors of this paper very gratefully acknowledge to financial support of Croatian Science Foundation under project number IP-2019-04-8615 as well as for financial support of University of Rijeka under projects: uniri-tehnic-18-139 and uniri-tehnic-18-107.

7. References

1. Vo TP, Thai HT, Nguyen TK, Inam F: Static and vibration analysis of functionally graded beams using refined shear deformation theory, Meccanica **49** (1), 155-168 (2014)
2. Vo T.P., Thai H.-T., Nguyen T.-K., Maheri A. and Lee J.: Finite element model for vibration and buckling of functionally graded sandwich beams based on a refined shear deformation theory, Engineering Structures, **64**, 12- 22, (2014)
3. Ziane N., Meftah S. A., Ruta G. and Tounsi A.: Thermal effects on the instabilities of porous FGM box beam, Engineering Structures, 134, 150-158 (2017)
4. Sina S.A., Navazi H.M. and Haddadpour H.: An analytical method for free vibration analysis of functionally graded beams, Materials & Design, **30**(3), 741- 747 (2009)
5. Nguyen T.-T., Kim N.-II. and Lee J.: Analysis of thin-walled open-section beams with functionally graded materials, Composite Structures, **138**, 75-83, (2016)
6. Reddy JN. *Mechanics of Laminated Composite Plates and Shells: Theory and Analysis* (CRC Press, Boca Raton, 2004)
7. Lanc, D; Turkalj, G; Brnić, J; Thuc P. Vo: Nonlinear buckling behaviours of thinwalled functionally graded open section beams, Composite structures, **152** (2016)
8. Lanc D., Vo T.P., Turkalj G. and Lee J.: Buckling analysis of thin-walled functionally graded sandwich box beams, Thin-Walled Structures, **86**, 148-156 (2015)

Mechanical and hydraulical stability of the offshore composit structure

Klodian Gumeni[1], Jorgaq Kaçani [2], Klodian Dhoska [3]
Polytecnich University of Tirana, Albania
Email: klodigumeni68@gmail.com

Abstract: *The aim of this research it was the installation of an intake sea water GRP (glass-reinforced plastic) structure in Vlore Bay. A detailed study about the extreme wave condition offshore was carried out by the SWAN (Simulating Waves Nearshore) model. Then the mechanical structure stability calculation was performed with AxisVM8, a finite element modeler & solver. Conservative hypothesis were taken, such as to use the max static pressure value as per energy balance calculation on the sea waves. The program Fluid Flow was used to model the pipe line end with pipe chimney connections. The scope of the calculation was primarily to balance fluid flows in each chimney in order to match the range of 0, 2 – 0, 25 m/s velocity at each chimney entrance.*
The result of the mechanical and hydraulically stability verification for the sea water intake structure take in consideration it was positive and this structure was installed successfully.
KEYWORDS*: COMPOSITE MATERIAL, SIGNIFICANT HEIGHT OF WAVE, WAVE ENERGY, VON MISE STRESS, STRESS INTENSIFICATION FACTOR.*

1. Introduction

In worldwide practice nowadays the use of offshore installations with GRP composite material is in a continuous development.
The main characteristics that the engineered solution was deemed to be inclusive, where:
From the construction point of view:

2. Easiness of construction
3. Easiness of installation
4. Easiness of handling
5. They are virtually non-corrosive to seawater
6. Relatively high solidity / specific weight ratio
7. Limited sensitivity to changing temperatures
8. Their production with relatively large diameters guarantees a low flow rate.

From engineering point of view:

1. Very shallow sea depth (around 2,5 m)
2. Turbulent area in case of windstorm (sea storm) with sea water waves breaking.
3. Possibility, during sea storm to suck-in sand.
4. Possibility, during sea storm to dry a part of the structure.

2. Prerequisites and means for solving the problem

2.1 Definition of wave parameters

2.1.1 Study of wave typology in Vlora bay

The aim of this study is:

1. Determination of the nature of waves in Vlora bay
2. Computer wave modeling resulting in wave distribution, given in a graph of Hs with respect to Tm and Tp for each sector, where:

- Hs- significant wave height
- Tm- wave period
- Tp- peak wave period

2.1.2 Nearshore wave modeling

Wave propagation from offshore and wave growth due to winds in Vlore Bay were modelled using the SWAN (Simulating Waves Nearshore) wave model to predict wave condition in this area [1]. From the study was found that under extreme wave conditions for all directions and for 1, 10 and 100 year return periods, the largest significant wave height is for the 100 year period equal to 4.2m. It should be noted that the water intake structure will receive waves from all directions, which will be considered in its design.
Figure 1, show the results of the SWAN model for a 100 year return period for offshore waves.

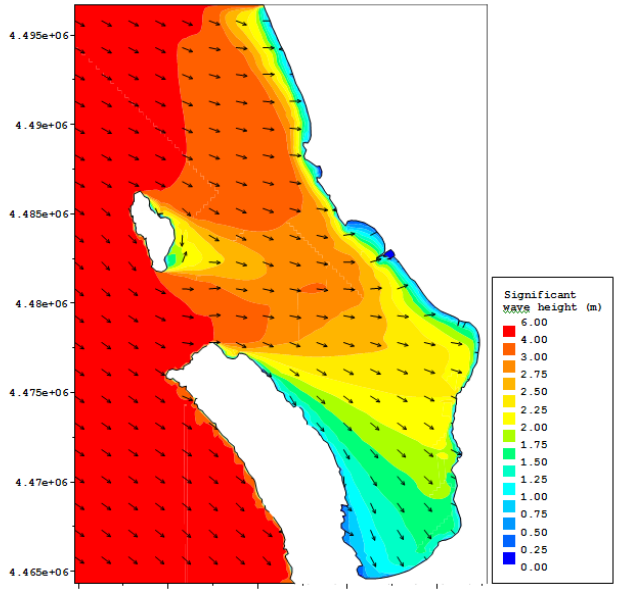

Figure 1. *SWAN model results for 100 year return period offshore wave.*

2.2 Prediction of extreme wave condition (Weibull).

There are several different methods of estimating extreme events from limited data. They are based upon the idea of fitting a standard probability distribution to the range of data which is available. The extreme wave heights are then obtained by substituting the corresponding extreme probability levels into the fitted equation [2].
Extreme value distribution:

$$P(H_s) = 1 - \exp\{-[\frac{H_s - a}{b}]^c\} \quad (1)$$

Where H_S is the significant wave height, P = probability less than H_S, and a, b, c are parameters to be found.

Weibull scales:

$$\log\{-\log[1 - P(H_s)]\} = c[\log(H_S - a) - logb] \quad (2)$$
$$y = \log\{-\log[1 - P(H_S)]\} \quad (3)$$
$$x = \log (Hs-a) \quad (4)$$

x and y are ploted on linear scales. Waves of a given return period (N years) are determined graphically from the appropriate probability. The expected highest individual wave (H_{max}) in a sequence is related to H_S by the approximate formula:

$$\frac{H_{max}}{H_S} = (\frac{1}{2} lnN)^{\frac{1}{2}} \quad (5)$$

Where N is the number of waves in the sequence.

2.3 The SWAN wave transformation model

SWAN is a computational spectral wave transformation model. It can be used to obtain realistic estimates of wave parameters in coastal areas, from given wind, seabed, and current conditions [3].

The SWAN models represents the waves in terms of the two dimensional wave action density spectrum N (σ, θ), even when the nonlinear phenomena dominate. The action density is equal to the energy density divided by the relative frequency:

$$N(\sigma, \theta) = \frac{E(\sigma,\theta)}{\sigma} \quad (6)$$

Where σ is the relative frequency and θ is the wave direction. In SWAN the two-dimensional wave action density spectrum may vary in time and space. Its evolution is described by the spectral action balance equation, which for Cartesian coordinates is:

$$\frac{\partial}{\partial t}N + \frac{\partial}{\partial x}C_x N + \frac{\partial}{\partial y}C_y N + \frac{\partial}{\partial \sigma}C_\sigma N + \frac{\partial}{\partial \theta}C_\theta N = \frac{S(\sigma,\theta)}{\sigma} \quad (7)$$

3. *Solution of the examined problem*

3.1 Design basis and basic assumptions

From the above study we found that the wave climate in Vlore Bay consist of those waves generated offshore that propagate through the west and north entrance to the bay and those generated locally within the bay by winds from the south. The largest wave of 4,5m occur from the direction sector 195 to 225°N. These waves have an associated mean wave period of 7 to 8 seconds. The 100 year return period of significant wave height is 3,5m.

The significant wave height is, by international definition, the average height – measured from wave top to bottom, of the highest 30% waves. This means that, according to probability scatter, the highest wave is normally 1,5 x significant wave. The energy of the wave, i.e the actual height when measured from average sea water level is 1,5/2 x significant wave height. For this reason we can assume by calculation that the effective highest wave, measured from the average sea water level is 2,62m (return period on 4 hours during the highest 100 year storm).

Actually, absolute wave height as indicated is that measured in the Vlore Bay when the effect of shallow sea depth is disregarded. When the sea depth is less than half of the wavelength, the wave starts to "feel" the effect of the sea bottom: its velocity decrease and finally the wave break, losing part of its energy [4]..

The energy of the wave is then lower that the correspondent maximum "static equivalent" height, according to Bernoulli equation (mass and energy conservation principle for fluids in motion). The pressure and the resultant force of the wave break than, associated to this wave height is that due to Stevino's approximation.

The value resulting from Bernoulli-Stevino, was used for mechanical design calculation purposes.

3.2 Geometry description of the structure

In order to limit the flow velocity to a value in the range of 0,2 – 0,25 m/s, seven GRF pipe "chimneys" diameter 1600 and 1800 mm (selected according to hydraulic calculation) shall be welded through lamination PN10 type on a 1800 mm diameter underground piping (the header). In order to limit weight and dimensions of the header two pieces (12m and 9m respectively) of 1800 mm ID pipe shall be connected through an 18000 mm metallic clamp. The connection of the existing pipe end, at 250 m from shoreline shall be executed via another metallic clamp.

The pipe shall be buried to -1,5 m from the sea bottom, while the pipe chimneys, 3 m long each, shall extend 1,5 m from the sea bottom, 1 m from average sea water level.

As per study carried out, it's clear that actual wave height around 250 m from shore line shall be in the range of 1 m or less. Once the pipe connections are verified according to mechanical stability the most problematic phenomenon to be take in consideration is that, on a shallow sea depth, the effect of turbulence of wave break may be a cause of sand entrance in the pipeline. Thus 1,5 m elevation from sea bottom line is deemed suitable, in the range of velocity selected, to limit the risk sand entrance in the pipeline during normal sea condition but may not be suitable in case of severe sea storm, thus causing the CCPP to stop its operation. Further action may be taken afterward to limit this phenomenon, with small modification to the present design.

3.3 Velocity and pressure drop calculation

The program Fluid Flow release 3 was used to model the pipe line end with pipe chimney connections. The scope of the calculation was primarily to balance fluid flows in each chimney in order to match the range of 0,2-0,25 m/s velocity at each chimney entrance, thus increasing the pressure drop where necessary, through pipe chimney orifice, that shall be performed on 1800 mm common header.

3.4 Process calculation results

In the figure 2 is given the simplified geometry of the structure.

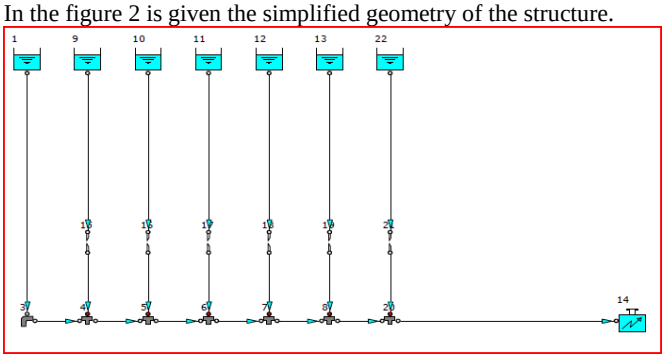

Figure 2. *The simplified geometry*

The data for the tables below are taken directly from the program.

Table 1. *Flow data in pipe stacks*

Unique name	Length (m)	ID (mm)	User number	Flow (m^3/h)	Pressure loss (Pa)	Velocity (m/s)
Pipe 4	3	1600	-14	1608	0,7	0,22
Pipe 7	3	1600	-13	1477	0,6	0,2
Pipe 6	3	1600	-10	1695	0,7	0,23
Pipe 5	3	1600	-8	1813	0,8	0,25
Pipe 3	3	1800	-5	1871	0,5	0,2
Pipe 2	3	1800	-4	1993	0,6	0,22
Pipe 1	3,1	1800	-3	1540	0,4	0,17

Table 2. *Flow data in orifice*

Unique name	Elevation (m)	Orifice size (mm)	User number	Flow (m^3/h)	Pressure loss (Pa)	Corner tap loss (Pa)
Pipe 2	3	1600	15	1993	6,4	0,22
Pipe 3	3	1200	16	1870	118,8	0,2
Pipe 4	3	950	17	1608	287,9	0,23
Pipe 5	3	900	18	1813	497,8	0,25
Pipe 6	3	800	19	1695	807,5	0,2
Pipe 7	3	700	21	1173	0,6	0,22

3.5 Mechanical stability calculation

Based upon input data as settled in 3.1, a computational finite element model was established both for 1600 mm and for 1800 mm pipe stack. Conservative hypothesis were taken, such as to use the max static pressure value as per energy balance calculation on the sea waves [5]. The pipe stack has been modeled as if rigidly connected to a fixed header (the underground pipe header) capable to withstand all transmitted forces. This approach is considered suitable for the purpose of mechanical verification, since

appropriate SIF shall be applied to allowable pipe stresses to take into account the "Tee" branch connection geometry, also based upon the fact that the mechanical characteristics of the pipe stack and pipe header are homogeneous.

Pipes material features

Elastic modulus in longitudinal direction: 22000 N/mm^2
Elastic modulus in transversal direction: 11000 N/mm^2
Thick of the pipe: 27 mm
Density: 1850 kg/m^3
Poisson coefficient: 0.2
Lowest allowable stress: 275 Kg/cm^2

3.5.1 Calculation

The analysis was performed with AxisVM8, a finite element modeler & solver. The action of these deformations can be relatively calculated taking account the contribution for lateral soil reaction (about 26 t/m^2) on the part of the underground pipe modelled with spring applied on shell surface. It is necessary to define the values of the maximum pressure, so that they are consistent with the intensity and wave level considered, therefore the scheme of calculation to be adopted is illustrate in the following. Considering a height wave of 2,62 m, the pressure applied to the part of pipe outside the ground (1,5 m) is:

$$\Delta P = \rho g \Delta H = 1000 \frac{kg}{m^3} * 9{,}81 \frac{m}{s^2} * 2{,}62m = 25702Pa = 25{,}7kPa \quad (8)$$

Once the maximum stresses according to Von Mises are calculated with AxisVM8, then the appropriate Stress Intensification Factor (SIF) according to ANSI is applied in order to compare actual stress to allowable stress. The actual SIF value was calculated modelling with CAESAR II – the piping modeler and stress analysis solver program – the geometry of the piping spool.

For both 1600 mm and 1800 mm branch connection, the calculated SIF is 2,3.

4. *Results and discussion*

4.1Vertical pipe φ1600 mm.

The figures below show the load case geometry and the relevant mesh definition:

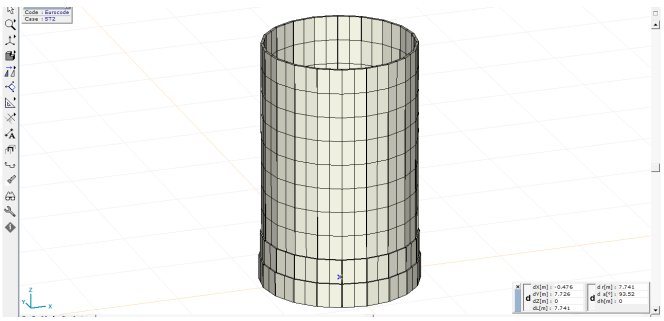

Figure 3. Vertical axial tube geometry

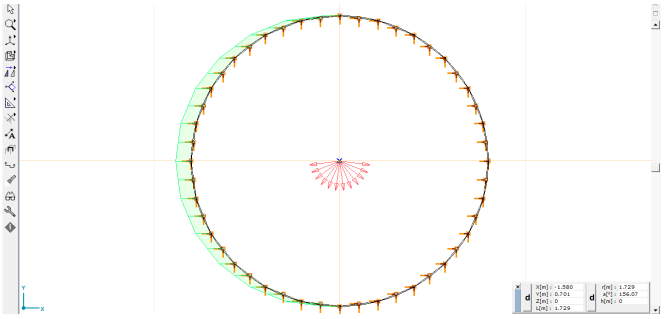

Figure 4. *Node definition and constrains*

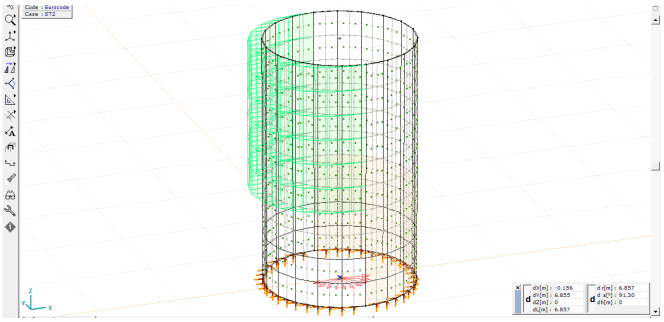

Figure 5. *Loads application on geometrical model*

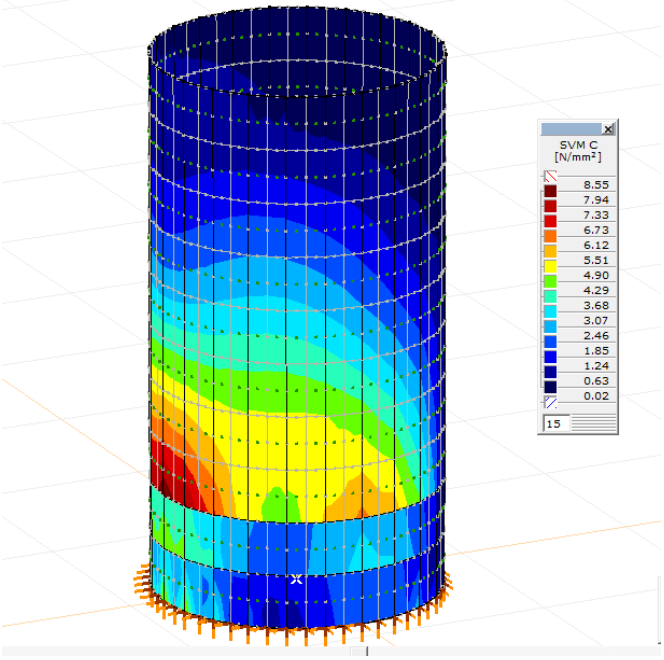

Figure 6. *Stress with Von Mises method*

Maximum stress according to Von Mises = 85,5 Kg/cm^2.
Maximum stress after SIF application = 85,5 x 2,3 = 196,7 Kg/cm^2
Allowable stress = 275 Kg/cm^2.
Safety margin 40 %.

4.2 Vertical pipe φ1800 mm.

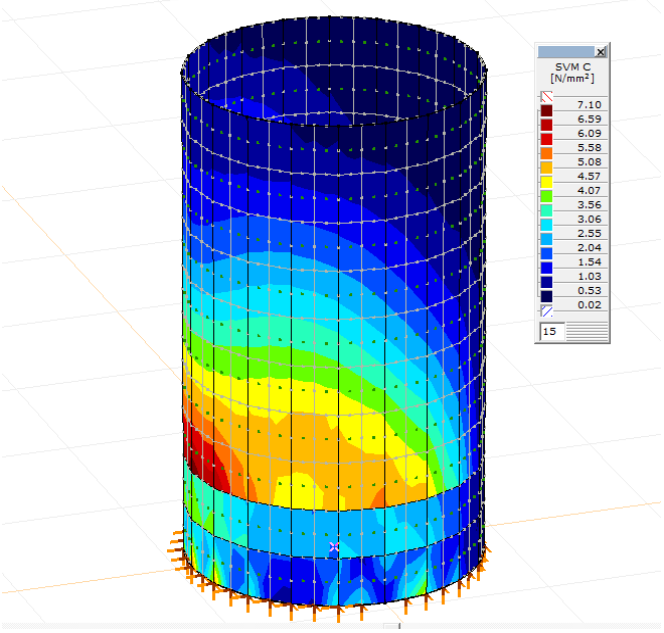

Figure 7. *Stress with Von Mises method*

Maximum stress according to Von Mises = 71 Kg/cm^2.
Maximum stress after SIF application = 71 x 2,3 = 163,3 Kg/cm^2
Allowable stress = 275 Kg/cm^2.
Safety margin 68 %.

5. Conclusion

The structure will be exposed to waves that are generated offshore that propagate through the entrance in the bay towards the site from west and north. The site will also be exposed to waves generated locally by winds from the south-east and south.

Mathematical modeling of the waves and their distribution spectra showed a satisfactory approximation of the real situation in the Vlora bay.

Hydraulic model of the structure, the flow balance having as the criterion that the suction velocity should be in accordance with the environmental directives, led to a clear concept of materialization of the structure with seven vertical tubes and a common horizontal collector.

Finite element modeling of the structure for calculating its mechanical stability, taking into account the action of the waves in the direction of the most significant height as well as the accurate calculation of their pressure from the energy balance, produced a highly reliable model for successfully assembling of the structure in an extremely complex environment of the sea.

6. References

[1] Booij N, Holthuijsen L.H, Ris R.C, The "SWAN" wave model for shallow water, Proc. 25th Int. Conf. Coastal Engineering, Orlando, 1996, pp.668-676.
[2] Collins J.I, Prediction of shallow water spectra, J.Geophys.Res, 77, No 15, 1972, pp.2693-2707.
[3] Eldeberky Y, Nonlinear transformation of wave spectra in the nearshore zone, Ph.D thesis, Delft University of Technology, Department of Civil Engineering, 1996.
[4] Madsen O.S, Poon Y.K and Graber H.C, Spectral wave attenuation by seabed friction, Theory, Proc 21th Int.Conf.Coastal Engineering,ASCE,1988, pp.492-504.
[5] Guo B, Song Sh, Chacko J and Ghalambor A, Offshore pipelines, 2005, pp.52-70.

Optimization of pneumatic vane motor based on mathematical modeling and computer simulation

Spartak Poçari[1], Andonaq Londo[2]
[1] Harry Fultz Institute in Tirana, [2] Mechanical Faculty at Polytechnic University of Tirana
spartakpocari@yahoo.it, alondo@fim.edu.al

Abstract: *Pneumatic vane motors are important actuators in industry, their optimization is difficult without e best mathematic model and computer simulation. In this article we presents a mathematical model for pneumatic vane type motors, construction of a simulation program associated with constructive engine parameters, experimental confirmation , and pneumatic motor performance optimization based on this model. The article begins with the description of the working principle of the vane type pneumatic motors, the geometric parameters that characterize it. The set of mathematical model equations consists in: the equations of geometry, the equation that describe the rotating moment, and equations expressing the mass flow into the motor. For the construction of the simulation program we have used the programming language of the G type LabView. Matching the results obtained from the simulation with the measured ones experimentally indicate that the built mathematical model is accurate and can be used to optimize pneumatic motors.*
KEYWORDS: *PNEUMATICS, PNEUMATIC VANE MOTOR, AUTOMATIZATION, FLUID-POWER, LABVIEW, COMPUTER SIMULATION.*

1. Introduction

The principle of the vane motor is that a rotor with a number of vanes is enclosed in a rotor cylinder. The motor is supplied with compressed air through one connection and air escapes from the other connection.

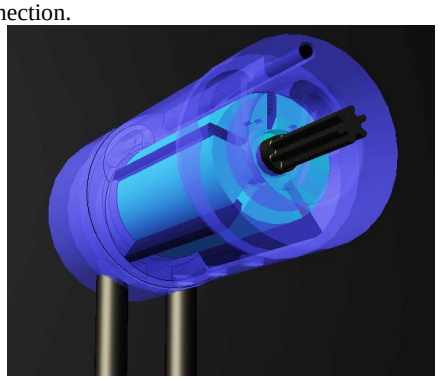

To give reliable starting, the air pressures press the vanes against the rotor cylinder. The air pressure always bears at right angles against a surface. This means that the torque of the motor is a result of the vane surfaces and the air pressure.
To study the performance of vane motor is difficult without e best mathematic model and computer simulation. In this article we presents a mathematical model for pneumatic vane type motors and the way to optimize them.

2. Preconditions

To build a mathematic model, assuming a polytrophic process and an ideal gas.

2.1 *Mathematic Model*

To construct the mathematical model of the pneumatic vane motor we will refer to the set of equations consisting of: equations describing geometry, equations expressing the rotational momentum of the rotor, and equations describing the mass flow of fluid passing through the motor.

Equations describing geometry

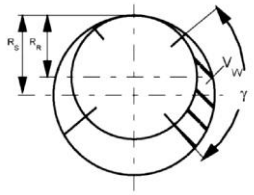

Fig.2.1.1. *Definition of vane angle (Υ)*

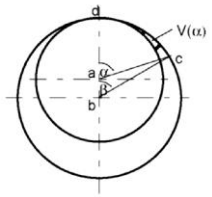

Fig.2.1.2. *Definition of rotor angle (α) and stator angle (β)*

$$\gamma = \frac{2\pi}{z} \qquad (2.1.1)$$

Where z is the number of vanes which is usually between 3 and 8.
The eccentricity ex is the difference between the inner radius of the cylinder and the radius of the rotor:

$$ex = R_S - R_R \qquad (2.1.2)$$

the rotor angle β is a function of the stator angle α.

$$\beta = \alpha - \arcsin\left(\frac{ex*\sin(\alpha)}{R_S}\right) \qquad (2.1.3)$$

Geometric volume of chambers between vanes from point d to point c. See fig.2.1.2 given by:

$$V_\alpha = \frac{L}{2}(R_s^2 \cdot \beta - R_r^2 \cdot \alpha - ex \cdot R_s \cdot \sin(\beta)) \qquad (2.1.1)$$

Geometric volume V_w of work chamber, volume between two vanes is given by:

$$V_w = \begin{cases} V_\alpha & for \;\; 0 < \alpha \leq \gamma \\ V_\alpha - V_{\alpha - i\gamma} & for \;\; i\gamma < \alpha \leq 2\pi \\ V_{2\pi} - V_{\alpha - \gamma} & for \;\; 2\pi < \alpha \leq 2\pi + \gamma \end{cases} \qquad (2.1.2)$$

The filling volume V_{fill} and the expanded volume V_{exp} if the geometric data is available, see Fig. 2.1.1. The ratio between the expanded and filling volume determines to what extent the internal energy of the air is used and is called the expansion ratio ε,

$$\varepsilon = \frac{V_{exp}}{V_{fill}} \qquad (2.1.3)$$

If a high expansion ratio is used, the engine power increases, but it may be that the air temperature in the supply equipment drops so much that it results in freezing of the water in the air by blocking the engine.
The nominal displacement volume is given by:

$$V_{disp,nom} = V_{fill} \cdot z \qquad (2.1.4)$$

Ideal engine torque

To construct the mathematical model of the rotational moment, we studied the thermodynamic processes. They include the equations for calculating the work, whose derivatives with

respect to time will give us the model of engine power and torque.

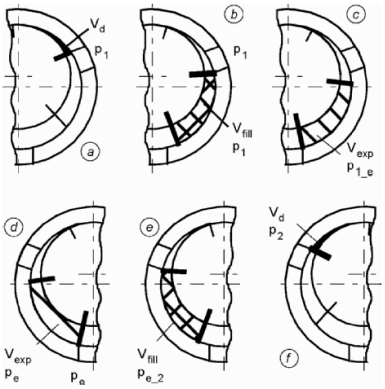

Fig.2.1.3. *Working volume between two shovels as a function of rotation angle*

Figure 2.1.1. shows the volume of one compartment as a function of the rotation angle, Fig. 2.1.4 the corresponding PV diagram (assuming clockwise rotation of the rotor). State *a* is the beginning of the rotation when the vane opens the compartment and air fills the dead volume. In state *b* the compartment is completely filled with air of pressure p1. While the rotor turns to *c*, the volume of the compartment increases. This process is assumed to be polytropic and the air pressure can be calculated by:

$$p_{1-e} = p_1 \left(\frac{V_{exp}}{V_{fill}}\right)^n = p_1 \varepsilon^n \qquad (2.1.5)$$

Where n polytropic index, $1 \leq n \leq \kappa$, $\kappa = 1.4$ for air.

Typically a value of n = 1.3 is used (Daser 1969; Sbahi 1992). When the vane opens, the air discharges and the pressure falls to the surrounding pressure p_e. This is the pressure at state *d* after the vane has closed the compartment and a reduction of the compartment volume begins. The air is compressed until at *e* the vane opens and releases most of the air to the second working port. Some air remains, state *f*. The compression from *d* to *e* is often neglected.

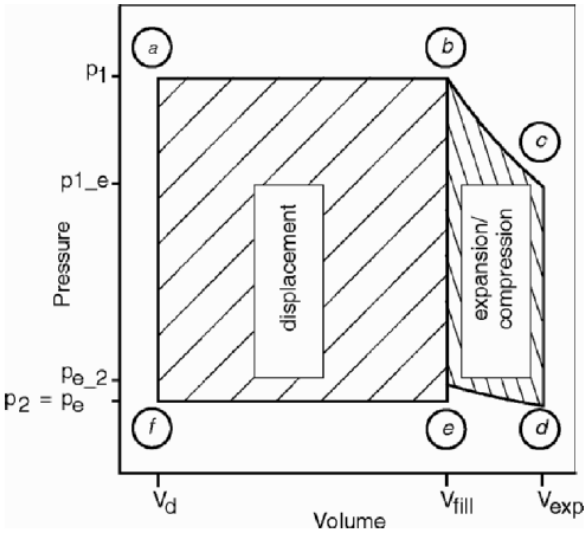

Fig.2.1.4. *PV diagram of the motor process in one compartment*

The work from the whole process is the sum of the expansion work, the displacement work and the compression work. Assuming a polytropic process and an ideal gas, the work is given by:

$$W = W_{exp} + W_{disp} + W_{compre} \qquad (2.1.6)$$

$$W_{exp} = -\int_c^b p dV = \frac{p_1 V_{fill}}{n-1}(\varepsilon^{1-n} - 1) \qquad (2.1.7)$$

$$W_{disp} = -\int p dV = (p_1 - p_2)(V_{fill} - V_d) \qquad (2.1.8)$$

$$W_{compre} = -\int_e^d p dV = \frac{p_2 V_{exp}}{n-1}(\varepsilon^{n-1} - 1) \qquad (2.1.9)$$

The power P of the motor can be calculated by differentiating the work W with respect to time. For the simulation model the torque T at the motor shaft is needed which is given by:

$$T = \frac{P}{\omega} = \frac{1}{\omega}\frac{dW}{dt} \qquad (2.1.10)$$

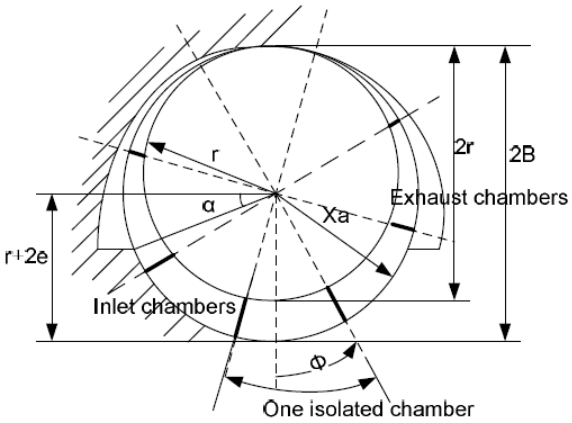

Fig.2.1.5. *Working radius of the vanes*

The working radius of the shovel referred to in figure 2.1.5 can be calculated from the relation:

$$X_a = ex \cdot cos\phi + \sqrt{B^2 - ex^2 \cdot sin^2\phi} \qquad (2.1.11)$$

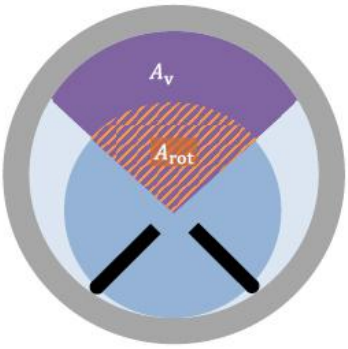

Fig.2.1.6. *The area between the two vanes*

The area A_v between the two shovels shown in light purple in Figure 2.1.6 is calculated by the following equation:

$$A_v = \frac{1}{2} \cdot \int_{\varphi_1}^{\varphi_2} X_a(\varphi) d\varphi \qquad (2.1.12)$$

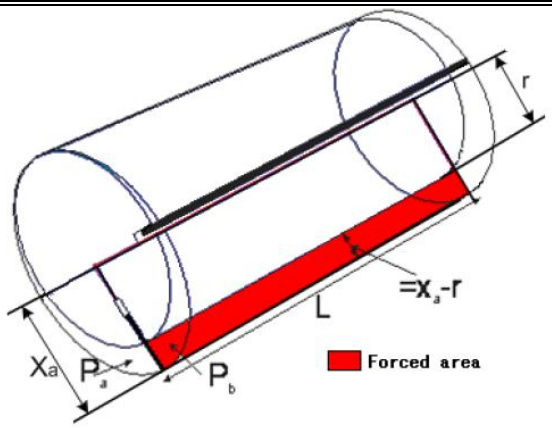

Fig.2.1.7. *Vane surface where rotational force is created*

Referring to figure 2.1.7, the rotational moment will be described by the relation:

$$M = (p_a - p_b) \cdot (X_a^2 - r^2) \frac{L}{2} \qquad (2.1.13)$$

Mass flow

Before the air can enter a compartment, it has to flow through long and narrow ducts whose resistance cannot easily be calculated analytically. There is also considerable leakage between the ports and through the bearing at the front side of the rotor.

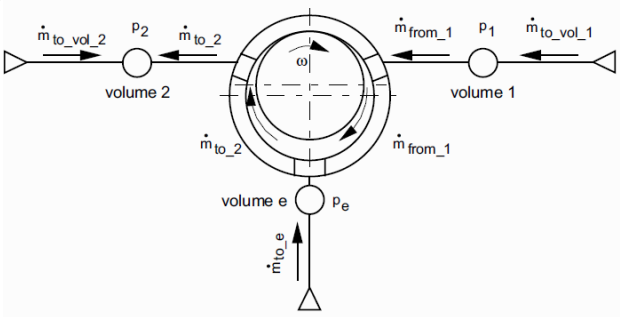

Fig.2.1.8. *Mass flow in the ideal motor*

Referring to Figure 2.1.8. we will express the mass flow through the equation:

$$\dot{m}_1 = -\dot{m}_{from_1} + \dot{m}_{to_vol_1} \qquad (2.1.14)$$

And through the equation of the ideal gas state:

$$p_1 = \frac{m_1 \cdot R \cdot T_0}{Vol_1} \qquad (2.1.15)$$

The mass flow rate $\dot{m}_{to_vol_1}$ depends on the pressure at port 1. The mass flow through the motor can be calculated from the compartment volume and the pressure p_1. Assuming clockwise rotation, $\omega > 0$, the mass flow rate from inlet 1 of the stator to inlet e, $\dot{m}_{from_1}$, is given by:

$$\dot{m}_{from_1} = \frac{p_1 \cdot \omega \cdot V_{disp,nom}}{2 \cdot \pi \cdot R \cdot T_0} \qquad (2.1.16)$$

For the mass flow rate $\dot{m}_{to_2}$, it follows accordingly:

$$\dot{m}_{to_2} = \frac{p_e \cdot \omega \cdot V_{disp,nom}}{2 \cdot \pi \cdot R \cdot T_0} \qquad (2.1.17)$$

The mass flow $\dot{m}_{to_e}$ can be calculated from the equation:

$$\dot{m}_{to_2} + \dot{m}_{to_e} = \dot{m}_{from_1} \qquad (2.1.18)$$

The mathematical model of the ideal engine does not take into account some important phenomena, such as the leakage flows between vaness and stator, system inertia and mechanical friction. Therefore, additional flow paths with nozzles, inertia and bearing friction have to be added to this ideal motor, see Fig. 2.1.9 for nozzles. To find parameter values for the nozzles and the friction model, a numerical estimation scheme can be used (Beater 2004).

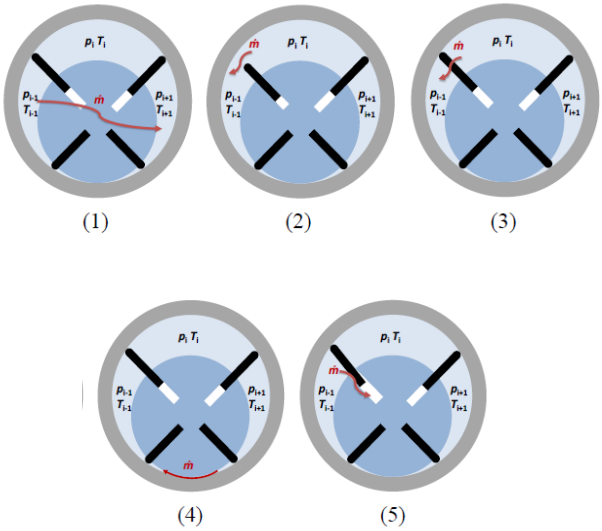

Fig.2.1.9. *Schematic of the main paths for leakage mass flow inside the vane motor*

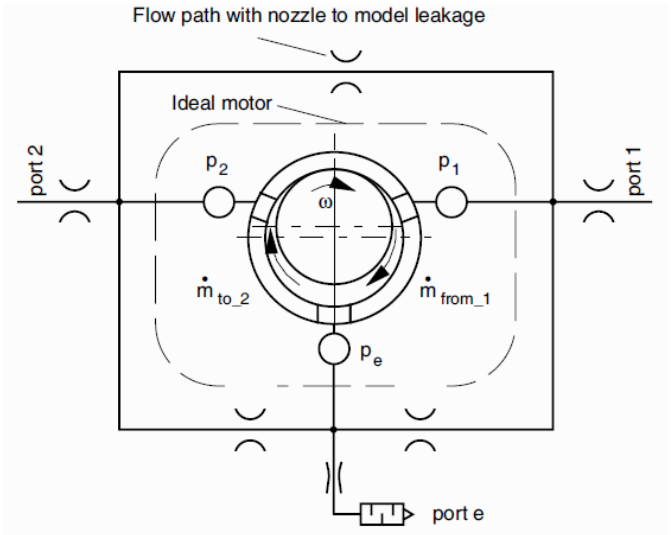

Fig.2.1.10. *Model that takes into account internal fluid leakage*

$$\dot{m}_{leakage} = 0.1mm \cdot L \cdot \sqrt{2 \cdot \frac{k}{k-1} \cdot p_1 \rho_1 \cdot \left(\left(\frac{p_2}{p_1} \right)^{\frac{2}{k}} - \left(\frac{p_2}{p_1} \right)^{\frac{k+1}{k}} \right)} \qquad (2.2.6)$$

2.2. Computer Simulation

Using the mathematical model described above and the LabVIEW G type programming language we have built simulation programs for the pneumatic vane motor.

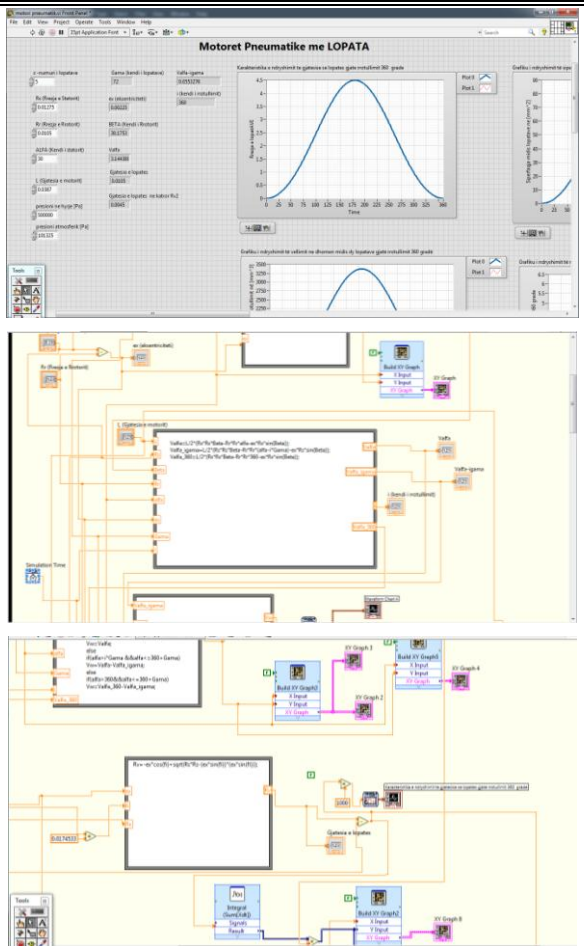

Fig.2.2.1. *Preview of the build program*

3. Optimisation

The performance characteristic of the motor is shown in curves as below fig.2, from which torque, power, and air consumption can be read off as a function of speed. Power
is zero when the motor is stationary and also when running at free speed (100%) with no load. Maximum power (100%) is normally developed when the motor is driving a load at approximately half the free speed (50%).

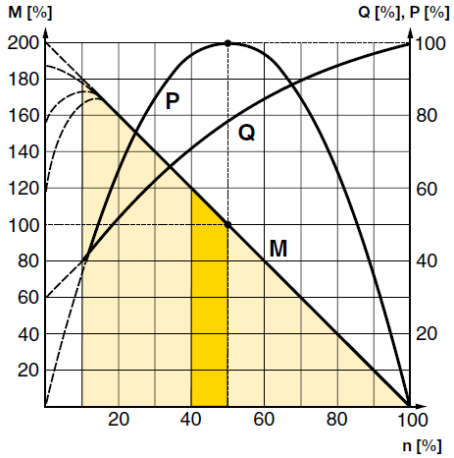

Fig. 3.1. *Vane motor characteristics*

Where:
P=Power
M=Torque
Q=Airconsumption
N=speed

Torque at free speed is zero, but increases as soon as a load is applied, rising linearly until the motor stalls. As the motor can then stop with the vanes in various positions, it is not possible to specify an exact torque. Air consumption is greatest at free speed, and decreases with decreasing speed, as shown in the above diagram.

The performance of an air motor is dependent on the inlet pressure. At a constant inlet pressure, air motors exhibit the characteristic linear output torque / speed relationship. However, by simply regulating the air supply, using the techniques of throttling or pressure regulation, the output of an air motor can easily be modified. The most economical operation of an air motor is reached by running close to nominal speed. By torque of M = 0, the maximum speed (idle speed) is reached. Shortly before standstill (n - 0), the air motor reaches its maximum torque (Mmax = 2 x M_o). At nominal speed (n_n), for example in
the middle of the speed range, air motor reaches its maximum power output (P_{max}).

Energy Efficiency

A pneumatic motor achieves its maximum power when it is operating as close as possible to its rated speed (50% of the rated idle speed). The energy balance is best in this area, because the compressed air is used efficiently.

Optimization of speed and torque

The speed and torque can also be regulated by installing a pressure regulator in the inlet pipe. This means that the motor is constantly supplied with air at lower pressure, which means that when the motor is braked, it develops a lower torque on the output shaft.

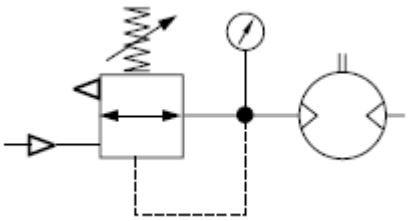

Fig.3.2. *Pressure regulation atmotor inlet.*

Speed regulation, air flow reduction

Every size reduction or restriction on the air line, whether of the supply hose itself or fittings, before the air motor affects the amount of the supplied air. By throttling you reduce the speed of the motor and simultaneously, the required torque. That means that you reduce the motor performance. The most common way to reduce the speed of a motor is to install a flow control valve in the air outlet, you can set the speed without loss of the torque. When the motor is used in applications where it must reverse and it is necessary to restrict the speed in both directions,
flow control valves with by-pass should be used in both directions. If the inlet air is restricted, the air supply is restricted and the free speed of the motor falls, but there is full pressure on the vanes at low speeds. This means that we get full torque from the motor at low speeds despite the low air flow. Since the torque curve becomes "steeper". this also means that we get a lower torque at any given speed than would be developed at full air flow. The benefit of throttling the inlet is that air consumption is

reduced, whereas throttling he exhaust air maintains a slightly higher starting torque.

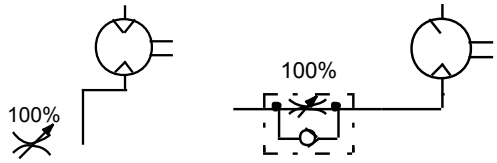

Fig.3.3. *Speed regulation, air flow reduction*

Reducing motor leakages and air consumtion

Inside the motor in the starting moment is the air pressure that push the vanes to the surface of the stator to create the necesary seal. So in the starting moment the leakages and air consumtion are to big vesus next moments, because the in the first moment distance betwin banes and stator is to big. If the vanes are adapted with spetial spring see the figure 3.4 below. The seal is in the necesary level at the starting moment.

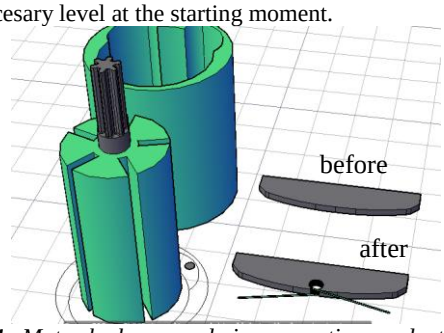

Fig.3.4. *Motor leakages and air consumtion racduction way*

Optimization of torque

Are to way to optimize the torque of the motor, increase the pressure, and increasing the radius of the stator and rotor. Using the program build in LabView we have do the simulation for stator diamter increased 10% , 20 % and 30 % .

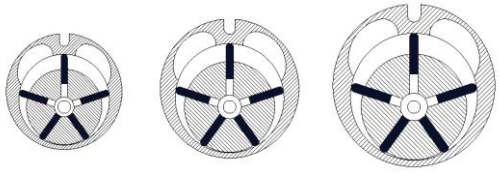

10% 20%, 30%

Fig.3.5.*Thre diameters of stator considered in simulation*

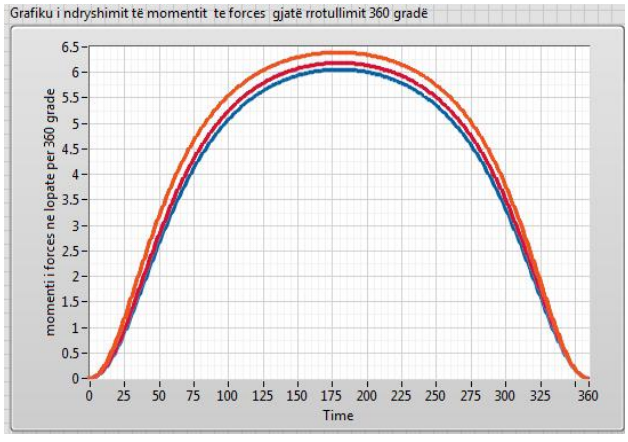

Fig.3.6. *The torque of the motor for 3 stator diameters*
Blue 10 %, red 20 % , orange 30 % more bigger

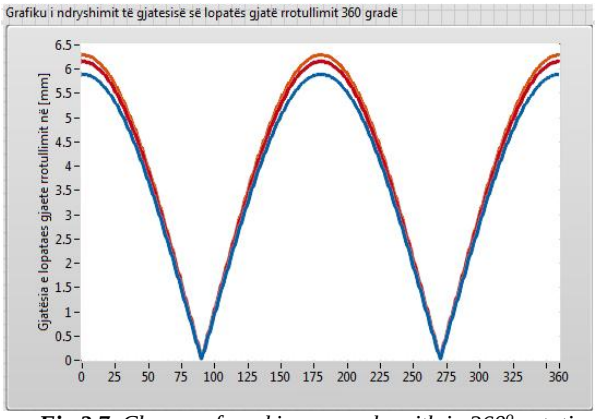

Fig.3.7. *Change of working vanes lengjth in 360° rotation Angle*

4. Conclusion

Using simulation software for the design and optimization of pneumatic actuators is the best and most economical way. Implementation of simulation programs requires a good and complete mathematical model as well as a programming language that can solve complex hydrostatic and mechanical equations in real time. The mathematical model presented above as well as the built-in simulation software can be used for optimization and precision (PID) command of the pneumatic vane motors.

5. References

[1] Londo. A "Transmisionet Hidropneumatike" 2008 Sh.B.L.U Tiranë 2008
[2] Zecchi. A "Controllo ed Elaborazione Numerica dei Segnali Con LabVIEW" Milano: Tecniche Nuove. 1999
[3] Andrew Parr "Hydraulics and Pneumatics" Third edition 2011
[4] S. Poçari, A. Londo. Mathematical Modelling and Computer simulation of pneumatic vane motor with LabView. *2nd International Conference "Engineering and Entrepreneurship" 10-11 October 2019*, Tirana, Albania.
[5] National Instruments. "Function and VI Reference Manual" January2016
[6] National Instruments. "User Manual". January 2016
[7] National Instruments. "Data Acquistion Basics Manual". January 2016
[8] Ninka. I "Metoda Numerike" Tiranë: 1983
[9] Hoxha. F "Analiza Numerike" Tiranë: Sh.B.U. 1997

Study the work of specialized car service as queue theory

Assist. Prof. Grozev D. PhD.[1], Assist. Prof. Milchev M. PhD.[1] M.Sc. Georgiev I. PhD.[2]
Faculty of Transport –University of Ruse "Angel Kanchev", Bulgaria [1] dgrozev@uni-ruse.bg
Faculty of Natural sciences and education –University of Ruse "Angel Kanchev", Bulgaria [2]

Abstract: *Study the refusal of requests received in a specialized automotive service workshop in the city of Rousse was investigated. The present work analyses the average monthly requests from customers of the workshop and the number of the actual repairs is determined. The work in the service have been seen as a mass service system with a non-stationary mid-month incoming stream with queries. Under non-stationary conditions, the basic values of the system parameters were calculated and Mat Lab application was created. The proposed approach can serve as a methodology for analysing and optimizing the activity of other universal automotive service.*

KEYWORDS: QUEUE THEORY, REFUSALS OF REQUESTS, MODELING, SPECIALIZED AUTOMOTIVE SERVICE, CORRECTION, OPERATING MODE, ORGANIZATION OF WORK

1. Introduction

Various studies have shown the importance of tires for driving a vehicle safely and economically [3]. This is especially important in bad weather conditions combined with wet and slippery roads. [5]. In the Republic of Bulgaria, such conditions occur mainly during the autumn-winter period of the year. To ensure road safety, the Bulgarian Road Traffic Act (Article 139, Paragraph 1, Item 4) states that during the period (November 15-March 1) motor vehicles, trailers and semi-trailers must are fitted with tires designed for winter conditions complying with the requirements of paragraph 4, or tires with a tread depth of at least 4 mm. [12]. From what has been said so far, there is no clear definition in the Bulgarian legislation of what kind of tires should be used during the winter months of the year. The decision on what kind of tires the vehicles will be equipped with is left to the fleet owners and managers. It is the responsibility of the same persons to decide when to change the tires. Therefore, in the tire repair shops can be expected a peak in the performed activities around the date of entry into force of Art. 139, para. 1, item 4 of the Road Traffic Act.

This report examines the specialized service of ARGO Ltd. in city of Rousse. The service was opened in 1997 as additional part of the company's business [13]. In the surveyed service, for a period of one year, more than 2000 cars enter the service and repair of the wheels, and more than 1100 are returned (about 52%) due to their inability to be serviced. The high percentage of returned cars raises the question of whether it is possible to reduce returned vehicles. Exploring this possibility is implemented as the work of the service is viewed as a system of mass service. The main activities carried out in this specialized service are: fixing flat tires, balancing of automobile wheels, replacement of worn tires with new or appropriate for the season.

2. Exposition

In order to describe the operation mode of the car service, considered as a mass service, it is necessary to know the characteristics of the incoming flow of cars considered as a stochastic process, the service intensity, the maximum length of the tail and the number of service units stochastic process, the service intensity, the maximum length of the tail and the number of service units.

For the inbound flow of freight we can make the following assumptions:

- ordinary flow - The probability of two or more cars occurring for an elementary time interval is infinitely small compared to the probability of occurrence of only one car. The normality feature means that the cars come as single, not in group of two, three and so on at the same time. [6,9,14,15];

- flow without consequences - the number of cars arriving in the system for time interval Δt does not depend on how many vehicles have already arrived, ie. does not depend on the history of the studied phenomenon (the flow without action afterwards (Poisson flow).

- stationarity/non-stationarity of the flow [8,11,14] - for sufficiently long periods of time - 1 month, 6 months, 1 year, etc. it is possible to assume the steady-state of the incoming stream, that is to say, with certain conventions. the probability of occurrence of a certain number of cars in a given, sufficiently long interval depends only on the length of that interval. Generally, in arbitrary periods, the λ stream is non-stationary λ = λ (t). This non-stationarity is clearly distinguishable over a period of one business year (about 300 working days).

Research service has three working places with six workers who work normal working hours.

An investigation of the flow of cars for the period from October 2018 to September 2019 (Table 1, Figure 1) was made. For the period under review, 2105 vehicles have passed. There are clearly two major peaks, in orders, in the months of October-November and April-May.

Table. 1 *Number of cars in service*

Month	Number of cars
October 2018	352
November 2018	361
December 2019	120
January 2019	86
February 2019	72
March 2019	61
April 2019	348
May 2019	353
June 2019	133
July 2019	87
August 2019	69
September 2019	63

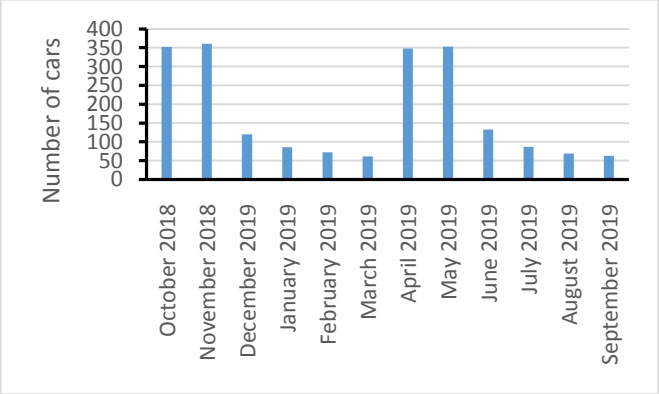

Fig. 1 *Number of cars in service*

The time of service in the study period was also investigated. The data are presented in Table 2 and FIG. 2.

For the period 10.2018 - 09.2019. data is available on the number of vehicles received. The intensity of service according to the data of the service manager is known to be partly constant. The average service time of

a car in the busiest months is about 40 minutes and in the nonbusiest months it is about 15-20 minutes. This is explained by the fact that with fewer clients, some of the installers who are not busy servicing the channel (the channel is free) help the busy channels.

Tab. 2 *Average time to service one car*

Month	Average time to service one car, [min]
October 2018	40
November 2018	40
December 2019	30
January 2019	25
February 2019	20
March 2019	15
April 2019	40
May 2019	40
June 2019	30
July 2019	25
August 2019	20
September 2019	15

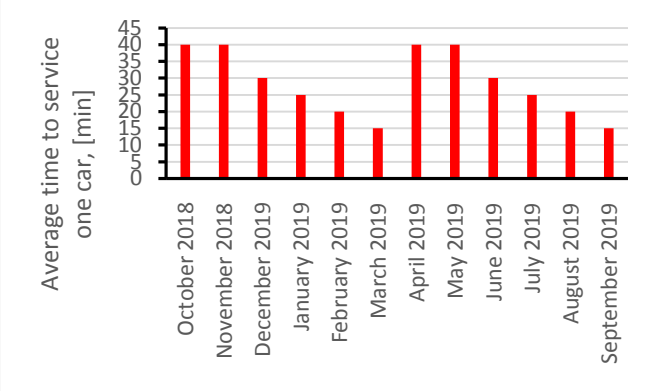

Fig. 2 *Average time to service one car*

The average service intensity μ per month is calculated as the number of vehicles that can be serviced by all channels for a given month. Regarding the number of service channels (servers) in the service, it is 3. Two workers are required to ensure continuous operation for 8 hours per channel. Again, according to the manager, given the nature of the service, with more than m = 1 waiting clients in the queue, in most cases the customer refuses to wait. To test the performance of the system, it is necessary to find the probability in the system that has the k number of vehicles at the moment t with n servers running, ie. [2,7].

$$P_k(t) = ?, k = \overline{0, n+m}, t \in [0, T], \quad (1)$$

where for one period T is taken one full working month. The beginning of the first working month (initial state) t = 0 coincides with the astronomical beginning of the year, the end of the last working month is t = 11, witch is the end of the astronomical year.

For a model such as queue model system (QMS), the following can be summarized as follows: a queuing flow of density λ (t) enters a queuing system with n serving channels. The query service time is a random variable with an exponential distribution and a parameter μ - in part constant. A car arriving at the moment when all channels are occupied, enters the waiting line and "patiently" waits to be serviced, unless there is more than m = 1 car in the service queue, ie. the system is with limited number of cars in the queue. The main indicator will be the intensity is returned requests, as well as during which time of the year these peaks are highest, as well as the average number of unprocessed requests in these peaks.

From what has been said up to now it can be said that the system is of type (M / M / s) in non-stationary mode. The following system of Kolmogorov (Erlang-Kolmogorov) differential equations is valid for describing a system of this type. [1,7,15]:

$$\frac{dp_0}{dt} = -\lambda P_0(t) + \mu P_1(t)$$

.....

$$\frac{dp_k(t)}{dt} = \lambda P_{k-1}(t) - (\lambda + k\mu) P_k(t) + \mu(k+1) P_{k+1}(t)$$

$$.....(0 \le k \le n-1)..... \quad (2)$$

$$\frac{dp_n(t)}{dt} = \lambda P_{n-1}(t) - (\lambda + n\mu) P_n(t) + n\mu P_{n+1}(t)$$

.....

$$\frac{dp_{n+s}(t)}{dt} = \lambda P_{n+s-1}(t) - (\lambda + n\mu) P_{n+s}(t) + n\mu P_{n+s+1}(t)$$

$$.....(0 \le s < m).....$$

$$\frac{dp_{n+m}(t)}{dt} = \lambda P_{n+m-1}(t) - n\mu P_{n+m}(t)$$

N denotes the number of channels and m is the maximum queue length when all servers are busy. In some cases (with endless waiting) the system of differential equations is open and for the numerical solution it is necessary to take the additional algebraic condition $\sum_{i=0}^{\infty} P_i(t) = 1$ for normality.

The input stream λ (t), in general, is different every day, and some seasonality is highlighted. The following table 1 provides statistics on requests received and service intensity by month for the period from 10.2018 to 09.2019. To model λ (t), it is appropriate to choose a relatively elementary function whitch have periodicity. This is appropriate given the seasonal variations. The least squares method (LSM) was used to approximate the averages values for the period 10.2018 -09.2019. The model should be as elementary as possible but reflect the most characteristic behavior of the real flow. The following trigonometric row, nonlinear to the coefficients sought, is selected as the model:

$$\lambda(t) = a_0 + a_1 \cos(wt) + b_1 \sin(wt) + a_2 \cos(2wt) + b_2 \sin(2wt). \quad (3)$$

Coefficients $a_0, a_1, b_1, a_2, b_2, w$ are calculated according to the LSM:

$$a_0 = 175.7846, a_1 = -122.5684, b_1 = -104.5706, a_2 = 39.6417, b_2 = 70.3940, w = 1.0508. \quad (4)$$

The coefficient of determination is R^2=0.9966 (statistically significant). The coefficients a_0, a_1, b_1, w, are also statistically significant.

Tab. 3 *Intensity of service in the surveyed service by months*

Months of the year	Service intensity for month μ (25 working days)
10.2018	300
11.2018	300
12.2018	400
01.2019	480
02.2019	600
03.2019	800
04.2019	300
05.2019	300
06.2019	400
07.2019	576
08.2019	132
09.2019	120

In the general case, at large maximum queue length, the system has a large dimension. The computational features related to system (2) after the eventual introduction of an algebraic equation are as follows:

- large dimension system (generally);

- the system is differential-algebraic;
- the system is of the "stiff system" type (rigid system of equations).

This can be summarized as: a system of rigid, differential-algebraic equations and in some cases of large dimension system. Special numerical methods have been developed to overcome these difficulties. A Matlab program for solving system (2) was made using the built-in ***"ode15s"*** solver implementing Gere's method. When entering λ (t), μ, n, m, the application returns a numerical solution to $P_k(t)$. The accuracy of the default for the solver is artificially increased by 10^{-6} up to 10^{-9} for an absolute mistake and by 10^{-3} up to 10^{-5} for relative error [4,10].

For the service intensity μ, it is also appropriate to select a periodic function. Considering the data in Table 1, a more complex trigonometric row is selected for the model relative to (3):

$$\mu(t) = a_0 + a_1\cos(wt) + b_1\sin(wt) + a_2\cos(2wt) + b_2\sin(2wt) + a_3\cos(3wt) + b_3\sin(3wt) \quad (5)$$

The reason for choosing model (5) is in the better approximation. The coefficients $a_0, a_1, b_1, a_2, b_2, w$ are calculated by LMS in equation (5) are:

$$a_0 = 390.6947, a_1 = 71.0263, b_1 = 159.3549, a_2 = 86.5555, b_2 = 100.3832, a_3 = -146.9048, b_3 = -16.4436, w = 0.5746 \quad (6)$$

Figure 3 shows the graph of λ (t) with coefficients calculated by the LMS.

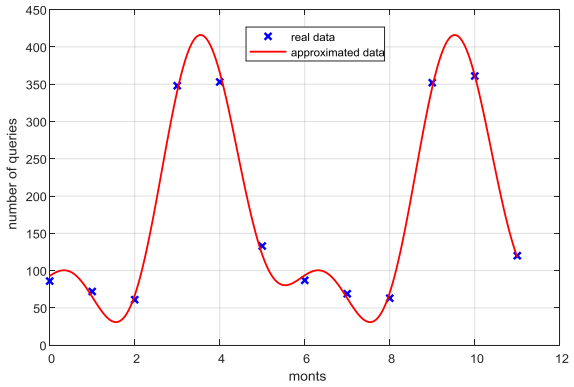

Fig. 3 *The function λ (t) with coefficients found according to the LSM*

The coefficient of determination is R^2=0.8963 (statistically significant).

Figure 4 shows the graph of μ (t) with coefficients calculated by the LSM.

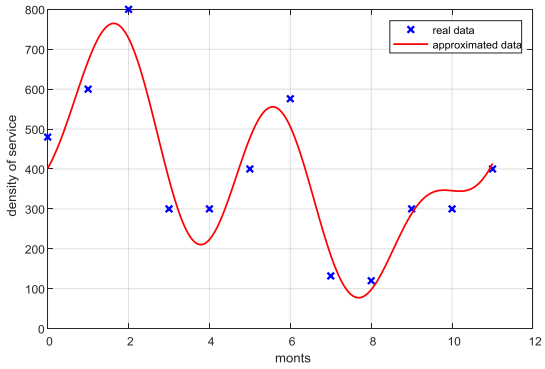

Fig.4 *The function μ (t) with coefficients found according to the LSM*

The initial state of the system Pk (t_0) is unknown. It is known that these types of processes are stable and after a long time enter into regular mode of operation. Therefore, an arbitrary initial state can be taken. The integration of the system needs to be done not for a single period of time, but for a sufficiently large number of periods. Thus the probability functions P_k (t) hey start to tend to their regular values. After several integrations with different end times, it is found that only after 5-6 periods the functions P_k (t) enter regular mode (for two adjacent periods, they remain the same). The accuracy is also increased here as the integration is done for 20 periods, with the difference between all P_k (t) in the last and the penultimate period being less than 10^{-8} for each t.

The following graphs show the results of the solution of system (2) at the following values:

- λ(t) calculated respectively by the coefficients of (4) and μ (t) by coefficients of (6),
- n = 3 (3 running servers),
- m = 1 (up to 1 place in the queue).

Figure 5 shows the probabilities of having exactly k∈ [0; 4] vehicles in the system. It is noteworthy that the most likely values for small or zero vehicles in worckshop are around the end of February, the beginning of March, and also in September.

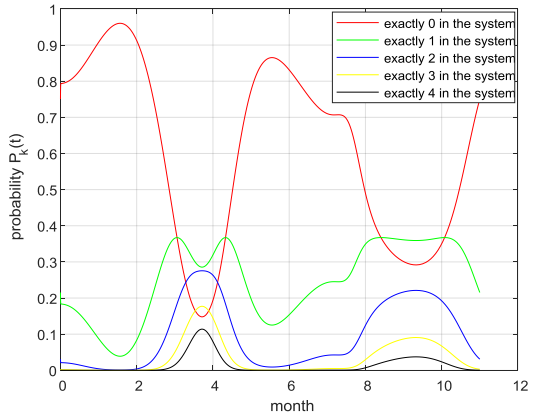

Fig. 5 *Graph of the probability of having exactly k∈ [0; 4] vehicles in the system*

It is also essential to know the density of rejected requests in Fig. 6. They are given with:

$$P_f(t) = \lambda(t)P_{n+m}(t) \quad (7)$$

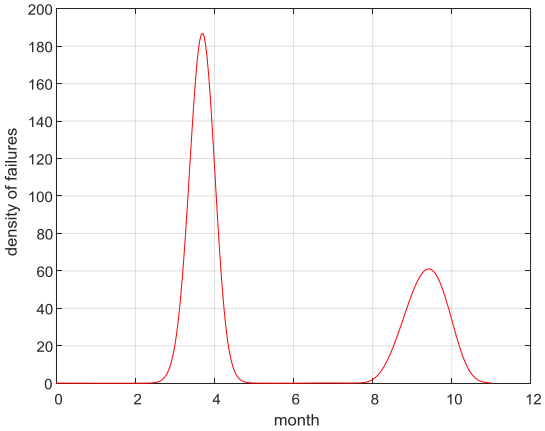

Fig. 6 *Graph of failure rejected requests density*

It is noteworthy that there are two large peaks of rejected requests density - one is the end of the aryl month, the beginning of May, the other is shortly after the beginning of October and November.

The volumes of retjected requests V_f calculated between arbitrary times t_1 and t_2 are given by:

$$V_f = \int_{t_1}^{t_2} \lambda(t)P_{n+m}(t)dt = \int_{t_1}^{t_2} P_f(t)dt \quad (8)$$

The average volume of rejected requests for the whole period is about 234,2671. The months of April, May, October and November are interesting, as the highest failure rates occur in them. The year is divided into three periods. The first period includes the months of April and May, the second - the months of October and November, and the third group includes all other months. After numerically solving the integral (8) for each group of months, the results are reported in Table 5.

Tab. 5 *Results of the calculations performed*

Months	Average number of fejects	% of all rejects
4,5	102.3368	43.6838
10,11	98.9257	42.2277
1,2,3,6,7,8,9,12	33.0046	14.0884

Table 5 shows that almost 87% of the returned requests are for a period of 4 months - from April, May, October and November.

3. Conclusion

The mode of operation of a specialized car service described is described as a queuing system. The characteristics of the incoming flow of vehicles, considered as stochastic process, the intensity of service, the maximum allowable length of the queue, and the number of service units are determined.

There is a two peak load of the service load in the incoming car flow with requests, which are in the months of October-November (713) and April-May (701). During these same months there is an increase in the service time of each request (about 40 min.). The model of the system describing the work in the specialized service is also defined, namely the system of Kolmogorov differential equations (Erlang-Kolmogorov).

After solving the system, the differential equations (2) are calculated the probabilities of the system to be in its many states. On the basis of these probabilities, key characteristics are calculated. One of them is the density of failures.

The flow of returned (unaccounted for) cars was established for the study period, which amounts to 234 units.

The discrepancy between the theoretical average number and the actual number of failures for the months of April, May, October and November diverges due to the accumulated errors in the approximation of the incoming flow λ and the speed of service μ, as well as factors not accounted for in the model used.

Different performance indicators can be calculated based on the model used to describe the work of the specialized service. Further exploration of a service center with that model can also provide a better option to handle the large number of returned (rejected) requests.

The study was supported by a contract of University of Ruse "Angel Kanchev", № BG05M2OP001-2.009-0011-C01, "Support for the development of human resources for research and innovation at the University of Ruse "Angel Kanchev". The project is funded with support from the Operational Program "Science and Education for Smart Growth 2014-2020" financed by the European Social Fund of the European Union.

References

1. A. Mitrofanova, Continuous times Markov chains. Poisson process. Birth and death process, (New York University, 2007)

2. H. Taha, Operations research, an introduction, New York (J. Wiley and Sons, 1993)

3. Kare Rumar, Ulf Berggrund, Per Jemberg, Uno Ytterbom, Driver Reaction to a Technical Safety Measure—Studded Tires, Human Factors: The Journal of the Human Factors and Ergonomics Society, Volume: 18 issue: 5, page(s): 443-454 Issue published: October 1, 1976

4. L. Shampine, M. Reichelt, The MATLAB ODE Suite, SIAM Journal on Scientific Computing, 18, 1-22 (1997)

5. Lena Larsson, Lennart Cider, Emil Pettersson, Co-optimizing multi vehicle combinations Fuel consumption & Traction in slippery conditions, Road-transport-technology Proceedings HVTT 14 (http://road-transport-technology.org/Proceedings/HVTT%2014/Larsson%20-%20Co-optimizing%20multi%20vehicle%20combinations%20fuel%20consumption%20%26%20traction%20in%20slippery%20conditions.pdf)

6. M. Zukerman, Introduction to queueing theory and stochastic teletraffic models, EE Department, City University of Hong Kong (2016)

7. N. Gautam, Analysis of queues: Methods and applications (CRC Press, 2012)

8. S. Ross, Introduction to probability models, (Elsevier, 2007)

9. J. Sztrik, Basic Queueing Theory, GlobeEdit, OmniScriptum GmbH, KG, Saarbrucken, Germany (2016)

10. V. Pavlov, I Georgiev, Optimization methods with MATLAB, (Avangard print, 2016)

11. Wallace R.B., D.N.Prabhakar Murthy, Case studies in reliability and maintenance, Wiley-interscience, 2003

12. ЗАКОН ЗА ДВИЖЕНИЕТО ПО ПЪТИЩАТА, в сила от 01.09.1999 г., Отразена деноминацията от 05.07.1999 г. (https://lex.bg/laws/ldoc/2134649345), (последно посетен 14.11.2019г.)

13. Представяне на фирма Арго ООД в бизнес каталог Авточастите БГ (http://avtochastite.bg/listing-%D0%B0%D1%80%D0%B3%D0%BE-%D0%BE%D0%BE%D0%B4-2023.html) (последно посетен 14.11.2019г.)

14. Р Митрев, Анализ и проектиране на системи за масово обслужване. Приложение в логистиката, строителството и подемно-транспортните системи, (Пропелер, София, 2017г.)

15. Т Саати , Элементы теории массового обслуживания и ее приложения (Книжный дом "Либроком", Москва, 2010)

Determination of empirical coefficients of heat dissipation characteristics by optimization methods for a spark-ignited car engine

Pavel Bolotov[1,*], Lloyd Rexford Neuburg[2]
MGTU N.E. Bauman, Moscow, Russia[1,2]
bolotovpo@student.bmstu.ru[1]
lloyd.neuburg@gmail.com[2]

Abstract: *For the development of new engines, as well as to obtain the correct results from mathematical modeling, numerical methods should be used, with the help of which verification of mathematical models takes place. This approach can significantly reduce the material and time costs at the development stage. The influence of the optimization method used in processing the experimental data of engine indexing to obtain semi-empirical coefficients of the form Wiebe is explored. A comparison is made of the rate of calculation of the coefficients of the Wiebe formula using brute force and gradient methods. In both methods, the integral using the modulus of the difference between squares of the experimental and calculated dependences is chosen as the target function. Analysis of the rate of calculation of the coefficients of the Wiebe formula showed the need to use the combined use of both methods: the global minimum of the objective function by the method of brute force with a large step and near the optimal point - the gradient method.*
Keywords*: PISTON ENGINE, HEAT DISSIPATION, INDICATOR DIAGRAM, OPTIMIZATION, OBJECTIVE FUNTION, BRUTE FORCE METHOD, GRADIENT DESCENT METHOD*

1. Formulation of the problem

When designing new engines, numerical methods are used, by which it is possible to significantly reduce the time and costs of developing new and improving existing piston engines [1]. Traditionally, the improvement of the engine is associated with the design and with the improvement of working processes. At present, special attention is paid to the improvement of the working process in the combustion chamber of a piston engine, since many toxic components are released into the environment with the exhaust gases [2,3,4]. Simulation of the combustion process in a piston engine is a difficult task, since it involves the calculation of a large number of physicochemical processes. In order to obtain a detailed account of all these processes, the use of computational fluid dynamic methods is required [5,6], which leads to the need to use large computational resources and long simulation times. In addition, at this stage of development of computer technology and calculation algorithms, this method does not allow for numerical optimization of a large number of parameters of the cylinder processes, especially for engines.

To calculate the cylinder processes in the early stages of design, semi-empirical formulas are needed, allowing for rapid optimization based on the laws of physics and chemistry. These models are successfully used in the study of the combustion process, but first they require verification, coupled with the processing of experimental data, and the refinement of a number of empirical coefficients of the mathematical model.

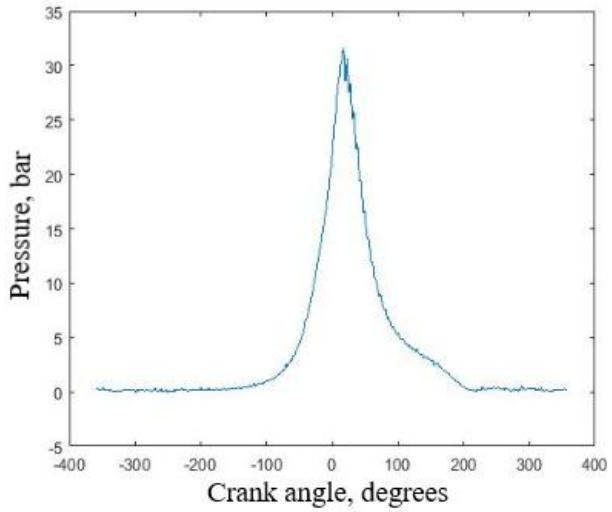

Fig. 1 *Example of an indicator diagram.*

Experimental data can be obtained by means of indicator diagrams, such as the one shown in Figure 1. Indicator diagrams measure the change in pressure in the cylinder over the course of a cycle. A pressure sensor is placed in a cylinder and measurements are taken at a set frequency. In addition, parameters such as atmospheric temperature and fuel consumption are measured, which are necessary for determining the heat release rate and total amount.

In this experiment, pressure readings were measured on a VAZ 2101 engine with an AVL pressure sensor GH12D at 20kHz, see Figure 2. By using a well-known engine with a large amount of supporting literature, it was possible to verify the legitimacy of the methodology used in this experiment. The empirical coefficients of heat dissipation characteristics obtained during the experiment could be compared to the results of previous studies, and if the results were sufficiently comparable, such methodology could then be implemented in the design of new engines or those which lacked a significant amount of research literature.



Fig. 2 *Pressure Sensor AVL GH12D*

Before the process of determining the empirical coefficients of heat dissipation could continue, a method for selecting the most appropriate indicator diagrams to analyze had to be developed. Pressure readings such as those shown in Figure 3 highlight the significant variability in cylinder pressure readings over the course of just a few cycles for a given engine mode.

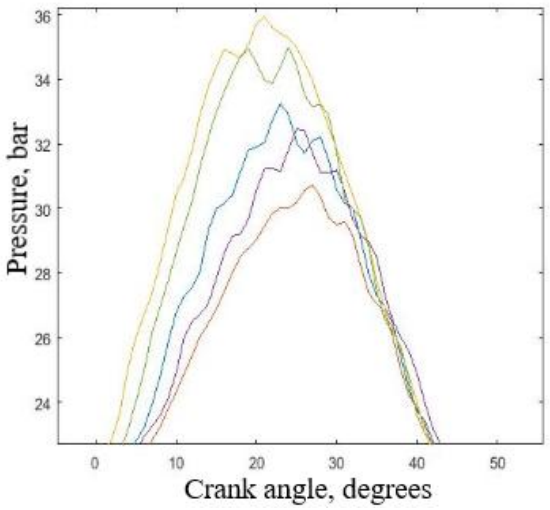

Fig. 3 *Enlarged image highlighting the difference in maximum pressure readings in the cylinder of a VAZ 2101, running at 2500rpm, 80% open throttle*

For this experiment, indicator diagrams taken from the same engine modes were compared with one another and an average pressure reading was determined. The measured cycle which was closest to this average was then chosen as the indicator diagram to be used to represent that specific mode. The average indicator diagram was determined two ways. First, it was decided to select the recording which was closest to the average indicator diagram, based on integrating the pressure readings over a set of crank angles from -100 to 100 degrees see Table 1. These specific values were chosen to ensure the intake and exhaust strokes were excluded from the combustion analysis. Next, the pressure readings were integrated at cylinder volumes which corresponded to the set of crank angles chosen in the first approach, which resulted in finding engine work output, see Table 2.

Based on the results, it was decided to select the most suitable indicator diagram based on integration of pressure over degrees, instead of pressure over volume, mainly due to the fact that this process is far simpler to integrate.

Table 1: *Minimum, Average and Maximum Pressure Readings integrated over degrees from indicator diagrams (2000rpm with 80% open throttle)*

RPM	Min Pressure (bar)	Avg Pressure (bar)	Max Pressure (bar)
2000	1739	2660	4470
2500	5266	5936	6387
3000	5907	6375	6881

Table 2: *Minimum, Average and Maximum Pressure Readings integrated over cylinder volume from indicator diagrams (2000rpm with 80% open throttle)*

RPM	Min Work (J)	Avg Work (J)	Max Work (J)
2000	87	130	219
2500	337	380	409
3000	362	390	422

Once all necessary measurements had been recorded and a method for choosing the correct indicator diagram had been determined, it was possible to continue with the task of refining the empirical coefficients for the combustion model.

Currently, combustion models can be divided into two large classes. The first class is combustion models, in which the kinetics of the process, the propagation of the flame front, etc. are calculated. The second model can be attributed to the calculation of heat generation or the rate of heat generation. With the help of such models the proportion of heat at a specified point in time can be calculated. These models allow for the calculation of the cylinder processes at high speed, but they require setting the "right" empirical coefficients to ensure the required calculations are accurate, while the models for calculating the heat release rate factor can be quite complex [7,8] and difficult when solving complex modern cylinder process optimization tasks [9,10].

There is a large number of semi-empirical dependencies for calculating the rate of heat release, but the formula of the Soviet scientist Wiebe has been most widely used [11,12,13]. In the derivation of this formula (1), the assumption of the chain mechanism of combustion of Semenov is used [11]. The formula for calculating heat dissipation is:

$$x = 1 - \exp[\, -6{,}908\, (\tau\, y/\, \tau z)^{(m+1)}\,], \quad (1)$$

where m is the rate of combustion; τ - the current time from the start of the combustion process, τ = 0 … τz; τz - the duration of the combustion process.

2. Object of study

In this work, an approximation of the experimental heat dissipation curve in various modes was performed by numerical methods for an automotive engine with spark ignition with a piston stroke of 66 mm and a cylinder diameter of 76 mm.

3. Mathematical Model

For the selection of parameters in the formula Wiebe, it is necessary to process the experimental data (indicator diagrams) and obtain the experimental heat release rate. To do this, we write the system of equations [14]:

$$dp/p + dV/V = dT/T, \quad (2)$$

$$dQ/dt = p \cdot dV/dt + m \cdot Cv \cdot dT/dt, \quad (3)$$

where p— pressure, Pa; V - volume, m3; T – temperature, K; R is the specific gas constant, m is the mass of the mixture, kg; Cv is the specific heat at constant volume, J/kg/K.

Solving the system of equations (2,3) we obtain the ordinary differential equation

$$dQ/dt = k/(k-1) \cdot p \cdot dV/dt + 1/(k-1) \cdot V \cdot dp/dt, \quad (4)$$

where k=Cp/Cv, for spark ignited gasoline engines, depending on the temperature, k = 1.280 ... 1.315 [15].

On the other hand, the derivative of heat supplied to the combustion chamber can be expressed as follows:

$$dQ/dt = dQw/dt + dQx/dt, \quad (5)$$

where Qw - the amount of heat absorbed from the combustion chamber into the wall, J; Qx - the amount of heat supplied during combustion, J.

Traditionally [11], at the end of the combustion, the amount of heat released as a result of chemical transformation from the fuel is calculated by the formula:

$$Qx = Hu \cdot qc, \quad (6)$$

where qc - cyclic fuel supply; Hu is the lowest calorific value of the fuel.

To simplify [14], one can make the following simplification:

$$dQw/dt = -\chi \cdot dQx/dt, \quad (7)$$

where χ is the fraction of heat corresponding to heat transfer to the wall of the combustion chamber, [14]. Then

$$dQ/dt = -\chi \cdot dQx/dt + dQx/dt, \quad (8)$$

or

$$dQ/dt = dQx/dt / (1-\chi). \quad (9)$$

Since the composition of the working fluid and its temperature change during the combustion process, the polytropic index also changes, see Table 3. In the mathematical model of this work, the dependence of the polytropic index k on temperature was used (the composition is taken into account implicitly at high temperatures):

Table 3: *Polytropic index for varying temperatures*

Temperature, K	200	700	1200	1700	2200	2700
k^a	1,315	1,310	1,305	1,300	1,290	1,280

Polytropic index

Taking heat exchange into account, we get the following formula:

$$dQx/dt = dX/dt \cdot qc \cdot Hu, \quad (10)$$

or

$$dX/dt = dQx/dt / (1-\chi) \cdot qc \cdot Hu, \quad (11)$$

To determine the duration of combustion and build the characteristics of heat generation by a numerical method, we replace the differentials (10,11) with finite differences, and instead of time, we will use the angle of rotation of the crankshaft, as shown in Figure 4b. Accepting these assumptions, we write the following equation

$$\Delta X/\Delta\varphi = [k/(k-1) \cdot p \cdot \Delta V/\Delta\varphi + 1/(k-1) \cdot V \cdot \Delta p]/\Delta\varphi, \quad (12)$$

where ΔP = Pi+1 – Pi; ΔV = Vi+1 – Vi; Δφ = φi+1 - φi; i - point number in the pressure array in the cylinder, as shown in Figure 4a.

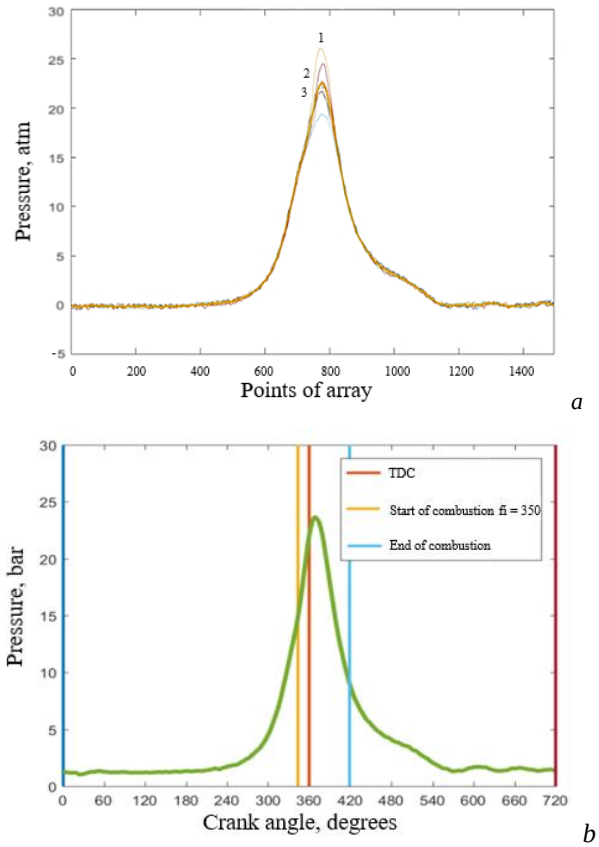

Fig. 4 *a - experimental indicator diagrams, 1,2,3 ... - number of cycles; b - averaged indicator diagram*

As the objective function, we take the sum of the modulus of the squares of the difference between the calculated curve and the experimental one. In this task, one should look for the minimum of the objective function:

$$f(a) \rightarrow \min, \quad (13)$$

where a = Σ[(ΔX / Δφ)i2 – (ΔXexp /Δφ)i2];

$$\Delta X/\Delta\varphi = C \cdot (mv+1)/\varphi z \cdot (\varphi/\varphi z)mv \exp[-C(\varphi/\varphi z)mv+1], \quad (14)$$

φz — burning time; mv —rate of fuel burned by the diffusion mechanism; C = log (1 – 0,999).

For a spark motor, the varying variable is the burn rate mv, which ranges from 0 to 7.

This task can be solved in two ways:

1) brute force method. To do this, we divide the range of varying variables with a constant step and calculate the value of the heat release rate using the Wiebe formula at every point. After that, we find a series of values of the objective function and determine the minimum among them. This method allows one to determine the global extremum, but requires a large amount of computation;

2) gradient method of multidimensional optimization (method of steepest descent). This is an iterative numerical method for solving optimization problems, which makes it possible to determine the extremum (minimum or maximum) of the objective function much faster than the brute force method. However, during the solution, the local minimum of the objective function is determined, which does not always coincide with the global extremum.

Comparison of two numerical methods for different engine operating modes is given in Table 4.

Table 4: *Results of the comparison of two numerical methods*

Crank shaft speed, min-1	**Brute Force**			**Gradient Descent Method**		
	mv	***min***	t_{calc}, c^b	***mv***	***min***	t_{calc}, c^b
2000	0.84	0.0017	14.3	0.816	0.0015	0.8
2500	0.67	0.0014	12.1	0.730	0.0013	0.9
3000	1.01	0.0021	10.0	0.978	0.0022	0.9

[a] t_{calc} –simulation time

From the data of Table 4 , the counting time using brute force is about 10 times lower than the counting rate using the gradient method. The use of the combined method: a full exhaustive method to determine the global extremum and the gradient method to refine the found solution, will reduce the computation time with a high accuracy of determining the empirical coefficients of the formula Wiebe

Figure 5 shows the processing result of the experiment and the calculation results by two methods using the example of a spark-ignited engine (at a crankshaft rotation speed of 2000 min-1).

The brute force method [16,17] allows the coefficients to be determined with sufficient accuracy, but its implementation requires a large amount of calculations, which leads to an increase in the simulation time. It follows that with an increase in the number of variables, the simulation time increases significantly.

The gradient descent method [18, 19, 20] makes it possible to find the minimum of the objective function in 10 ... 30 iterations, which leads to a reduction in the calculation time. However, the gradient descent method allows us to find the local minimum of the objective function, in contrast to the sequential search method.

As a result of the application of numerical methods, sets of coefficients (see Table 3) were obtained for the Wiebe formula for several modes that can be used for further calculations of the cylinder processes. Combining optimization methods makes it

possible to find the global minimum of the objective function using the brute-force method with a large step, and in the vicinity of this point, to use the gradient method.

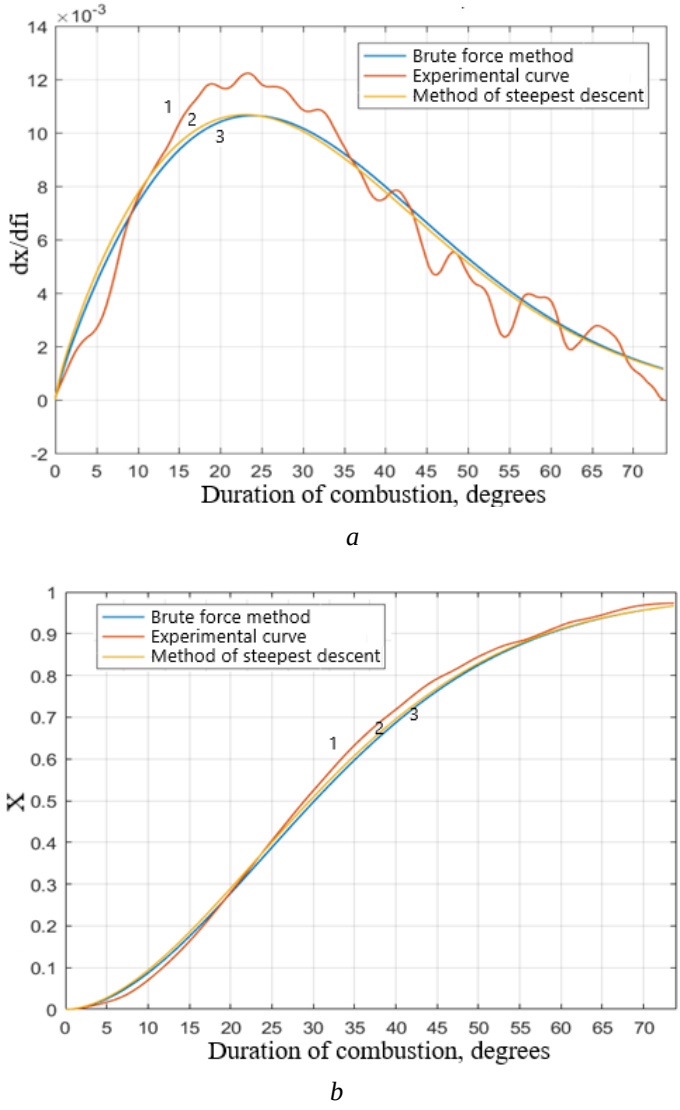

Fig. 5 *The dependence of the heat release rate (a) and heat release (b), obtained experimentally and by calculation, on the angle of rotation of the crankshaft (φ); 1 – experimental curve, 2 – brute force method, 3 – method of steepest descent*

4. Summary

1. Using two optimization methods, the mv coefficient for the semi-empirical heat release Wiebe formula is obtained, in several modes with partial engine load; the difference between the results obtained by different methods ranged from 4.6 to 8.2% - such a result can be considered satisfactory.

2. The application of each optimization method: brute force and gradient, has its own advantages and disadvantages. The combination of these methods can significantly increase the speed of calculations and the accuracy of determining the empirical coefficients of the b formula.

5. References

[1] Delprete, Cristiana, Fabio Pregno, and Carlo Rosso. "Internal combustion engine design: a practical computational methodology." SAE International Journal of Engines 2, no. 1 (2009): 263-270.

[2] Devaraj, A., I. Vinoth Kanna, K. Manikandan, and Jishuchandran. "Impact of Engine Emissions From HCCI Engine, An Overview." International Journal of Mechanical and Production Engineering Research and Development 7, no. 6 (2017): 501-506.

[3] Kim, Kibum, Hyungmin Kim, and Kihyung Lee. "Novel strategies and optimization techniques to reduce harmful diesel engine emissions." Environmental Engineering Science 29, no. 5 (2012): 335-342.

[4] Kihara, Nobutaka, Tokihiro Tsukamoto, Koichi Matsumoto, Kozo Ishida, Masao Kon, and Takao Murase. Real-time on-board measurement of mass emission of NOx, fuel consumption, road load, and engine output for diesel vehicles. No. 2000-01-1141. SAE Technical Paper, 2000.

[5] Weiser K., Ennemoser A. 3D-CFD Simulation of combustion and heat transfer in high-speed diesels. Valencia, Spain. THISEL Conference, 2002.

Weiser K., Ennemoser A. 3D-CFD Моделирование сгорания и теплообмена в быстроходном дизеле. Valencia, Spain. THISEL Conference, 2002.

[6] Laget, O., A. Kleemann, Stephane Jay, Benjamin Reveille, and S. Henriot. Gasoline engine development using CFD. No. 2005-01-3814. SAE Technical Paper, 2005.

[7] Kuleshov, A. S. Multi-zone DI diesel spray combustion model and its application for matching the injector design with piston bowl shape. No. 2007-01-1908. SAE Technical Paper, 2007.

[8] A.S. Kuleshov. Multi-Zone DI Diesel Spray Combustion Model for Thermodynamic Simulation of Engine with PCCI and High EGR Level, SAE Paper No 2009-01-1956, 2009.

[9] Malastowski N. S., Barchenko F. B., Grekhov L. V., Kuleshov A. S. Shaping of Injection Rate for Reducing Emission Level of High-Speed Engine. International Journal of Applied Engineering Research, 2016, vol. 11, Number 23 (2016), pp. 11189-11198.

[10] Malastovskij N. S., Barchenko F. B., Grehov L. V., Kuleshov A. S., Denisov A. A., Starkov E. E. Formation of requirements for the characteristics of the injection of a high-speed diesel in order to reduce toxicity. Engineering Journal: Science and Innovation, 2017, vol. 3. URL: http://dx.doi.o (date of the application 15 April 2017) DOI: rg/10.18698/2308-6033-2017-3-1594.

Маластовский Н. С., Барченко Ф. Б., Грехов Л. В., Кулешов А. С., Денисов А. А., Старков Е. Е. Формирование требований к характеристике впрыскивания высокооборотного дизеля в целях снижения токсичности. Инженерный журнал: наука и инновации, 2017, вып. 3. URL: http://dx.doi.o (дата обращения 15 апреля 2017) DOI: rg/10.18698/2308-6033-2017-3-1594.

[11] Kavtaradze R. Z. Theory of piston engines. Special chapters. Moscow, Bauman Press, 2008, 720p.

Кавтарадзе Р. З. Теория поршневых двигателей. Специальные главы. Москва, Изд-во МГТУ им. Н. Э. Баумана, 2008, 720с.

[12] Kuleshov A. S. Development of calculation methods and optimization of workflows of the internal combustion engine. Moscow, 2011, p18-26.

Кулешов А. С. Развитие методов расчета и оптимизация рабочих процессов ДВС. Москва, 2011, с18-26.

[13] Ghojel, J I. "Review of the Development and Applications of the Wiebe Function: A Tribute to the Contribution of Ivan Wiebe to Engine Research." *International Journal of Engine Research* 11, no. 4 (August 2010): 297–312. doi:10.1243/14680874JER06510.

[14] Heywood J. B., Internal combustion engine fundamentals. New York, 1988. p.930

[15] Ebrahimi R. Effect of specific heat ratio on heat release analysis in a spark ignition engine. Shahrekord Universiry, Iran, 2011.

[16] Akulich I. L. Mathematical programming in examples and problems. Moscow, 1986.

Акулич И. Л. Математическое программирование в примерах и задачах. Москва, 1986.

[17] Moore, A.W., Hill, D.J., and Johnson, M.P. An empirical investigation of brute force to choose features, smoothers and function approximators. In Hanson, S., Judd, S., and Petsche, T., editors, Computational Learning Theory and Natural Learning Systems, Volume 9. MIT Press, 1992.

[18] Gill F., Mjurrej U., Rajt M. Practical optimization. Moscow, 1985.

Гилл Ф., Мюррей У., Райт М. Практическая оптимизация. Москва, 1985.

[19] Korn G., Korn T. Math Handbook for Scientists and Engineers. Moscow, 1970.

Корн Г., Корн Т. Справочник по математике для научных работников и инженеров. Москва, 1970.

[20] Hasdorff, Lawrence. "Gradient optimization and nonlinear control." (1976).b

On the distribution of the incentive fund at the university

Irina Mamaeva [1]
Federal State Budgetary Educational Institution of Higher Education «Kostroma State Agricultural Academy»,
Karavaevo, Kostroma region, Russia[1]
Irina-Mamaeva@yandex.ru

The article highlights two approaches to solving the problem of the distribution of the incentive fund, one of which is based on the calculation of the cost of one point; the second one is based on elementary incentive payment in the system with weight indices. The latter approach makes it possible to single out a small number of clusters of successful personalities. Comparison of the considered approaches at the stage of their implementation allows us to draw the conclusion about the different aspirations of teachers in the performance assessment systems. A mathematical solution is proposed for the distribution of the incentive fund in the framework of the second approach. The proposed method allows dividing fund resources in an extremely short period of time.
***Keywords**: TASK OF THE DISTRIBUTION, INCENTIVE FUND, ACTIVITY, PERSONALITY, TEACHERS, CLUSTERS, METHOD OF CALCULATION, POINTS, WEIGHT.*

1. Introduction

Many higher education institutions develop strategic plans for their development. Obviously, the solution to this problem can only be complex. At the same time, one of the directions in the field of solutions is the determination of key indicators of teaching activities that affect the development of the university, and the further development of the corresponding incentive system [1].

At present, the question of improving the incentive system for university teachers remains relevant [2]. When developing any incentive system, researchers solve the problems of a quantitative method for evaluating activities and the distribution of the incentive fund between teachers.

We can find two approaches to the quantitative assessment of the activities of teachers. One approach uses rating points, the second – weights. There are different methodological grounds for the second approach (weight approach). However, often they lead to complicated decisions. It is relevant to search for such a solution to the problem of distribution of the incentive fund, which would be simple and create the conditions for the best teaching aspirations.

The article proposes a method for distributing an incentive fund among clusters of teachers. The method can be applied if the assessment system uses weighting factors and is based on the hierarchy method. In addition, the features of the point and weight approaches are discussed.

2. Preconditions and meals for resolving the problem

There are three main problems for incentive system developers:

1. What specific types of performance indicators need to be evaluated (taken into account) [3]?
2. How to get a quantitative equivalent of success (effectiveness) of the teacher [4]?
3. How to distribute the incentive fund for teachers?

The solution to the first and second problems is often executed jointly. Most of researchers use a point approach when the selected performance indicators of a teacher are characterized by rating points [5].

However, the point approach can operate with two types of rating [6]:

- a rating built with the use of a relative assessment of the performance of each teacher according to the natural indicators given in the various meters;

- a rating, built with the use of a single conditional-natural meter of the scope of works performed.

In the second case, the focus is on operating with coefficients when using a single meter of the scope of work performed. It can be attributed to the "weight approach" if “weighting factors” and the hierarchy method are used in its methodology.

That is, we will consider that the "weight approach" is a way of assigning quantitative estimates to the elements of the teacher 's activities, which uses weight coefficients and is based on the hierarchy method. There are various methodologies based on different foundations in determining the hierarchical set of indicators in the performance evaluation system.

The weight approach seems to us more justified for solving the problem of incentives, because the researchers found the demotivating nature of the point-rating system for assessing the activities (the first type of rating). Teachers aim to achieve a formal goal – getting points [7].

So, in the weight approach, the hierarchical system of indicators for assessing the effectiveness of university employees (types, elements of activity) is associated with weight coefficients [2]. To determine the values of weights, a comparative analysis can be used [8]. Weight coefficients can be part of a more complex system, such as a hierarchical system of criteria to measure and evaluate the effectiveness of quality assurance [9].

We can notice that the weight approach uses more flexible techniques to create a system for evaluating the performance of teachers.

Existing weight approaches differ methodologically; they can choose a different basis for establishing a hierarchy of performance indicators. More effective can be considered those that take into account the goals of the university and the personal orientation of the teacher. Less effective are those that set weights for previously financially stimulated privileges or positions.

In the approach with a rating of points after receiving a quantitative individual result for all teachers, the total of all points is calculated and, based on the size (amount) of the incentive fund, "the cost of one point" is calculated. Further, this should be multiplied by the individual points of the teacher.

In the weight approach, the same method of allocation of the incentive fund can be implemented, the difference can be manifested in the fact that weights can already be taken into account in calculations. Also, the weighted approach allows the use of other methods of distributing the incentive fund.

We propose a method of distributing the incentive fund, which is based on the distribution of personal results at several levels in the system of assessing the activities of the teachers.

It assigns incentive payments according to the level at which the teacher will be. This makes it possible on the one hand to lead teachers away from the pursuit of points, on the other hand to consider teachers at the same level as a community with equal opportunities in implementing educational or scientific projects. That is, the method allows you to distinguish clusters of teachers to solve different problems at the university.

The distribution of the incentive (premium) fund taking into account the selected levels can be realized by adjusting the methodology proposed by us earlier [10].

3. Results

A feature of the proposed method is associated with a mathematical solution to the problem of the distribution of the stimulating fund. The method takes into account:

- amount of money (size of the incentive fund);

- the distribution of the results of assessing the activities of teachers by levels (cluster distribution of teachers);

- coefficients that allow you to clarify the difference in payment between different levels of results (between different clusters).

The method of distribution of the incentive fund is implemented in five stages:

1. Initially, it is necessary to determine how many levels will be selected. There can be any number of levels. The choice of the number of levels can be done once - at the time the method is implemented. If necessary, you can return to the selection.

2. After forming an array of individual results of teachers' activities, it is advisable to normalize all results by the maximum value. This is necessary to avoid specific values, as they will be different in different systems. The result of this procedure should be a matrix with a list of teachers and their individual standardized results.

3. Next, it is necessary to calculate the "Width" of the range (D) taking into account the selected number of levels m, and, if necessary, the minimum (limiting) value of the individual normalized result ($R_{\min}$) can also be taken into account:

$$D = \frac{1{,}00 - R_{\min}}{m},$$

m is the number of levels.

4. Teachers are distributed by levels depending on the individual standardized result of the activities. The result of the procedure should be the number of teachers N_1, N_2, ..., N_m, the results of which fell into the corresponding ranges. Table 1 shows an example of the distribution of teachers by level at $R_{\min}=0$; m is 4; D=0,25.

Table 1: *The distribution of teachers by level.*

Level	Ranges	Number of teachers	Amount of one incentive payment
4	0,76-1,00	N_4	$k^3 \cdot S_e$
3	0,51-0,75	N_3	$k^2 \cdot S_e$
2	0,26-0,50	N_2	$k^1 \cdot S_e$
1	До 0,25	N_1	$k^0 \cdot S_e$

5. Finally, teachers are assigned payments from the incentive fund (see the last column of Table 1).

Let us explain the content of the last column of Table 1.

If SF is the amount of distributed incentive (premium) fund, it can be represented as the sum of the following type:

$$SF = N_1 \cdot S_e + N_2 \cdot k \cdot S_e + N_3 \cdot k^2 \cdot S_e + ... + N_m \cdot k^{m-1} \cdot S_e .$$

S_e is the elementary incentive payment, that is, the "elementary" part of the incentive payment that is taken as invariant;

N_1 is the number of teachers, whose results fell within the range of No. 1;

N_2 is the number of teachers, whose results fell within the range of No. 2, etc.

Separately, we will discuss the k coefficient. This is a coefficient that shows how many times the amount of incentive payment for teachers whose results hit different levels should differ. Its value and mathematical expression for it can be chosen by the developers of the incentive system themselves. We chose the power law for k, which reflects the difference in pay between teachers at different levels: at each next level the payment is k times more than at the previous level. Obviously, the coefficient k must be greater than one. It can be chosen the same, but it may be different for different levels or you can choose a different law for it.

The previous equation can be rewritten as:

$$SF = \sum_i^m (N_i \cdot k^{i-1} \cdot S_e) .$$

The elementary incentive payment is:

$$S_e = \frac{SF}{\sum_i^m (N_i \cdot k^{i-1})} .$$

And the amount of the incentive part of the payment (S_i) for one teacher at different levels is:

$$S_i = k^{i-1} \cdot S_e$$

Table 1 shows its mathematical expression for four levels, taking into account that $i = 1, 2, 3, 4$.

4. Discussion

Comparison of the considered approaches at the stage of their implementation allows us to draw the conclusion about the different aspirations of teachers in the performance assessment systems. Table 2 shows the comparative characteristics of the point and weight rating approaches and their differences.

Table 2: *Comparison of the point rating and weight approaches.*

Specifications	Point approach	Weight approach
Significator	rating points	weight coefficients
The way of distributing the incentive fund	one, there is no choice of the way	the possibility to choose the way
Single financial indicator	point cost	elementary incentive payment *
Possibility of automation	yes	yes
Personal orientations of the teacher	«pursuit of points»	seeking to get into another cluster *

* *when using the proposed method of distribution of the incentive fund.*

The proposed method of distribution of the stimulating fund can be applied both when considering general individual performance results, and when considering results for individual types of teacher activity (scientific, educational, etc.).

Calculations are easily automated in this method. After the number of teachers at different levels is determined, automation allows you to distribute the fund in a very short period of time.

5. Conclusions

The weight approach to the formation of the teacher performance assessment system is more flexible, it is able to reflect the significance of certain types and elements of activity, and therefore it is more promising from the point of view of managing teachers to achieve the goals of the University.

We can assume that the "weight approach" is a way of assigning quantitative assessments to the elements of the teacher's activity, which uses weighting factors and is based on the hierarchy method.

When implementing the weight approach, there is an opportunity to use the proposed method of distribution of the incentive fund. This method takes into account the size (amount) of the incentive fund, the number of teachers whose results have fallen at different levels, and the rule for determining the coefficient reflecting the difference in the incentive part of payment.

The method allows to change the attitude of teachers to the results of performance assessments and to form a desire to be in another cluster, but don't chase points.

6. References

1. M. V. Polevaya, *Performance evaluation system of employees of higher education institutions: current practice and key performance indicators,* Social & labour research, 4 (**37**), 98-105 (2019).
2. K. A. Dyusekeev, M.I. Shikulskiy, O.M. Shikulskaya., *Hierarchical system of indicators for the assessment of efficiency of higher education institution staff activity,* Fundamental-research, 5-1, 33-37 (2016).
3. T. G. Ozernikova, O.I. Gainullina, *Development of university faculty motivation based on balanced score card,* Baikal Research Journal, 5, 28 (2011).
4. D. V. Tyutin., A.V.Gorbatov, *The system of material incentives for teachers through the introduction of key performance indicators,* Kaluga Economic Bulletin, 1, 55-60 (2017).
5. M. R. Bechvaya, *Technology Performance Evaluation of Scientific and Educational Activities of Scientific-pedagogical Staff in Higher Education,* Journal of Economic Regulation, V.**6**,№4, 46-54 (2015).
6. I. A. Slobodnyak, O. A. Preina, *Estimation of the productivity of labor of the instructor,* Economics and Management: Problems, Solutions, V.**1**, № 4, 36-50 (2015).
7. V. V. Gromyko, *Labour culture in higher school in ergonomics context,* Vestnik of the Plekhanov Russian University of Economics, 5 (**71**), 64-75 (2014).
8. I. A. Bedrachuk, L. S. Mazelis, R. A. Lugovoi., K. S. Solodukhin, *Rating models for evaluating the activities of teachers in a university and determining the size of incentive and other payments,* Controlling, 37, 66-73 (2010).
9. E. A. Gorbashko, I. G. Golovtsova, *The Innovative Approach to the Assessment of the Quality Assurance of Educational Activity in High School,* Innovations, 1 (**183**), 26-30 (2014).
10. I.A. Mamaeva, *Method for scholarship calculation in the rating system*, Information Systems and Technologies, 5 (**97**), 39-44 (2016).